UNIVERSITÀ DEGLI STUDI DELL'INSUBRIA

ÉCOLE POLYTECHNIQUE

THESIS SUBMITTED IN PARTIAL FULFILLMENT OF THE REQUIREMENTS
FOR THE DEGREE OF PHILOSOPHIÆ DOCTOR IN PHYSICS

Pulse shaping and ultrashort laser pulse filamentation for applications in extreme nonlinear optics.

Antonio Lotti

Date of defense: February 1, 2012

Examining committee:

Advisor	Daniele FACCIO*	Assistant Prof. at University of Insubria
Advisor	Arnaud COUAIRON	Senior Researcher at CNRS
Reviewer	John DUDLEY	Prof. at University of Franche-Comté
Reviewer	Danilo GIULIETTI	Prof. at University of Pisa
President	Antonello DE MARTINO	Senior Researcher at CNRS
	Paolo DI TRAPANI	Associate Prof. at University of Insubria
	Alberto PAROLA	Prof. at University of Insubria
	Luca TARTARA	Assistant Prof. at University of Pavia

* current position: Reader in Physics at Heriot-Watt University, Edinburgh

Abstract

English abstract

This thesis deals with numerical studies of the properties and applications of spatio-temporally coupled pulses, conical wavepackets and laser filaments, in strongly nonlinear processes, such as harmonic generation and pulse reshaping. We study the energy redistribution inside these wavepackets propagating in gases and condensed media, in the linear and nonlinear regime. The energy flux constitutes a diagnostic for space-time couplings that we applied to actual experimental results. We analyze the spectral evolution of filaments in gases and derive the conditions for the generation of ultrashort pulses in the UV range. We study high harmonic generation in a gas from ultrashort conical wavepackets. In particular, we show how their propagation properties influence the harmonic output. We also study the interference of different electron trajectories. Finally, we derive the shape of stationary Airy beams in the nonlinear regime. For each topic, we present experimental results that motivated our works or were motivated by our simulations.

French abstract

Cette thèse traite de l'étude numérique des propriétés et des applications des impulsions spatio-temporellement couplées, paquets d'ondes coniques et filaments laser, dans les processus fortement non-linéaires, comme la génération d'harmoniques d'ordre élevé. Nous étudions la redistribution de l'énergie au sein de ces paquets d'ondes en propagation linéaire et non-linéaire. Le flux d'énergie constitue un diagnostic des couplages spatio-temporels que nous avons appliqué à des résultats expérimentaux réels. Nous analysons l'évolution spectrale des filaments dans un gaz et nous obtenons les conditions pour la génération d'impulsions de quelques cycles dans le spectre UV. Nous étudions la génération d'harmoniques d'ordre élevé par des ondes coniques ultra-courtes. En particulier, nous montrons comment leurs propriétés de propagation influencent le champ généré dans

la région X-UV. Nous étudions aussi l'interférence des différents chemins quantiques correspondant aux trajectoires électroniques. Enfin, nous obtenons la forme des faisceaux d'Airy stationnaires dans le régime non-linéaire. Pour chaque sujet, nous présentons des résultats expérimentaux qui ont motivé nos travaux ou ont été motivés par nos simulations.

Italian abstract

Questo lavoro di tesi tratta dello studio numerico delle proprietà di impulsi con accoppiamento spazio-temporale, pacchetti d'onda conici e filamenti laser, e di loro applicazioni a processi fortemente non lineari, come generazione di armoniche di ordine superiore o rimodulazione di impulsi. Studiamo la ridistribuzione dell'energia all'interno dei pacchetti d'onda in propagazione lineare e non lineare. Il flusso della densità di energia costituisce una diagnostica per accoppiamenti spazio-temporali, che abbiamo applicato a reali risultati sperimentali. Analizziamo l'evoluzione spettrale di filamenti in gas e deriviamo le condizioni per la generazione di impulsi UV ultracorti. Studiamo la generazione di armoniche di ordine superiore in gas da impulsi conici. In particolare, mostriamo come le loro proprietà propagative influenzino il risultato. Studiamo inoltre l'interferenza tra diversi cammini elettronici. Deriviamo infine il profilo di fasci di Airy stazionari in regime non lineare. Per ogni argomento, presentiamo i risultati sperimentali che hanno motivato il nostro lavoro, o basati sulle nostre simulazioni.

Acknowledgments

In this dissertation I have reported most of the scientific results and work I dealt with during my Ph.D. studies.

First of all, I want to thank my two co-tutors, Daniele Faccio from University of Insubria and Arnaud Couairon from École Polytechnique, who equally supported my work, suggested research lines, helped with the interpretation of the results and pushed towards the finalization of the works. From a personal point of view, I want to thank them for their friendship and availability, and for all the good moments we spent together. In particular, I want to wish good luck to Daniele for his new position at Heriot-Watt University and to him and his family (Silvia and Cesare) for their new life in Scotland.

I also want to thank the heads of the institutions and the leaders of the research groups in which I worked: at École Polytechnique, Patrick Mora, head of the CPHT, and Stefan Hüller, head of the Laser Plasma Interaction group at CPHT. I wish to thank Prof. Paolo Di Trapani from University of Insubria for hosting me in his group at the beginning of my Ph.D., and the group of general relativity, analogue gravity and theoretical physics of Dr. Sergio Cacciatori and Prof. Vittorio Gorini, with Prof. Ugo Moschella as group leader, for hosting me in the last part of this thesis. In particular, I want to thank Prof. Di Trapani for his deep insights not only related to physics, but in general to the approach towards Science and Nature.

The works presented in these pages was also performed thanks to a various network of collaborations. I want to thank, in no precise order:

- the UNIS group at the FORTH in Heraklion, Greece. In particular, the group leader, Prof. Stelios Tzortzakis and his colleague Prof. Dimitris Papazoglou; and the Ph.D. students Paris Panagiotopoulos and Daryoush Abdollahpour;

- the AUO group at the ICFO in Barcelona, Spain, in the persons of the group leader, Prof. Dr. Jens Biegert, the Post-Doc Researchers Dane Austin, Philip Bates and the Ph.D. students Stephan Teichmann, Alexander Grün;

- Prof. Mette B. Gaarde from Louisiana State University, Baton Rouge;

- the Ultrafast Laser Optics group at Leibniz Universität, Hannover, Germany. In particular, the group leaders, Prof. Dr. Milutin Kovačev and Prof. Dr. Uwe Morgner, the Post-Doc Researcher Daniel Steingrube, the Ph.D. students Emilia Schulz and Tobias Vockerodt;

- Prof. Miroslav Kolesik and Prof. Jerome Moloney, from the College of Optical Sciences at the University of Arizona, Tucson.

Contents

Contents ix

List of Figures

Introduction

This thesis deals with investigations in the field of extreme nonlinear optics and ultrafast science. In particular, we investigate the role of spatio-temporally coupled laser pulses of a particular class, namely conical wavepackets, in strongly nonlinear processes, such as harmonic generation and pulse reshaping, by means of a series of numerical works.

The starting point for these works is the fact that nonlinear processes are influenced by both the property of the medium (e.g. dispersion, or nonlinear response to the optical field) and the property of the light itself (e.g. phase and amplitude curvatures, or intensity localization). In fact, by properly tuning temporal and spatial property of a light pulse, it is possible to tailor the output of processes such as the generation of new frequencies, or the modification of the optical properties of the medium.

Such optimization, obtained by tuning the properties of the incoming light pulse, spans over a very wide range of applications; recent examples are the use of accelerating beams for efficient ultraviolet and soft X-ray generation [1], the use of conical Bessel beams for micro- and nano-machining [2] or the generation of long plasma channels [3, 4], the use of ultrashort laser pulses filaments for enhanced stimulated Raman conversion [5].

In particular, we concentrate our attention on the properties of conical wavepackets and their influence on highly nonlinear processes, such as frequency generation. The ultimate goal is enhancement and control of these processes, as well as fine tuning of the output radiation for what concerns frequency range, spatial (e.g. divergence angle) and temporal (e.g. duration) properties.

We also investigate the regime of ultrashort laser pulse filamentation, as a way of spontaneous spatio-temporal reshaping and conical wavepackets generation.

The core of this thesis work is numerical. However, our simulations were performed with the aim of predicting or interpreting a series of experimental results that supported our research. We therefore briefly present these experimental results that motivated our works or were motivated by our simulations. The experiments were performed by different groups which are among the leaders in their respective research fields.

In chapter 1 we present the equation describing the propagation of optical pulses and the approximations they are based on, referring in particular to two main models: a nonlinear envelope equation and a field propagation equation, which are at the basis of our simulations. We also illustrate and model the main nonlinear effects experienced by high intensity ultrashort pulses. The final sections are devoted to the description of the process of high harmonic generation (HHG), as one of the most promising strongly nonlinear effect for applications [6–8].

Chapter 2 presents the main topics of this thesis work, namely conical wavepackets and the filamentation regime.
Conical wavepackets are the polychromatic counterparts of Bessel beams and may be viewed as a continuous superposition of plane waves at different frequencies propagating along a cone with a characteristic frequency-dependent aperture angle. These wavepackets are thus inherently space-time objects, in the sense that it is not possible to separately factorize their spatial and temporal distributions.
The filamentation regime is characterized by a dynamical propagation of ultrashort optical pulses, in which these pulses remain tightly focused over extended distances (much larger than the typical diffraction length) without the help of any external guiding. We describe the main nonlinear effects which determine such propagation regime and we illustrate the main related phenomena and features. In particular, we describe the X-wave model, which interprets the main features of a filament as the spontaneous generation of stationary conical wavepackets.

In chapter 3 we develop a numerical tool for visualizing the information stored in the phase of optical pulses. This allows for calculating the energy density flux which represents the energy redistribution inside the wavepackets during propagation in gases or transparent condensed media. We concentrate on and analyze in detail the characteristic features of conical wavepackets by studying this energy density flux in the linear and nonlinear regime. In the nonlinear case, we focus on the filamentation regime.
We apply this numerical tool to actual experimental results, both in the linear and nonlinear case. In the latter case, we provide evidence of spontaneous generation of conical wavepackets in the filamentation regime.

In chapter 4, we continue our studies on the filamentation regime. We numerically analyze the spectral evolution of filaments in gases at different pressures, starting from a series of experimental measurements of the super-continuum generated in the filaments. We derive the phase profile at the third harmonic component in view of possible phase compensation and compression of the emitted light, for the generation of ultrashort pulse in the ultraviolet range.

In chapter 5, we consider HHG in a gas, as another source of femtosecond-attosecond pulses in the ultraviolet or soft X-ray spectral region. We consider the effect of pump pulses shaped as ultrashort conical wavepackets. We show that

the phase and envelope velocity properties of conical wavepackets influence the harmonic output and in particular we show that they act as a gating mechanism for phase-matched selection of quantum path contributions.

Quantum trajectory contribution in HHG is also the main topic of chapter 6. In particular, we present a second series of numerical simulations based on actual experimental data. Their analysis shows the evidence of interference between different electron trajectories, which may lead to complex spatio-temporal structures in the harmonic emission.

Finally, we present in chapter 7 a specific class of monochromatic accelerating beams sharing properties of conical wavepackets: the nonlinear Airy beams. These beams have the remarkable characteristic of preserving their intensity shape along propagation over an accelerated (parabolic) trajectory [9, 10].
We analytically and numerically derive the shape of stationary Airy-like beams in the nonlinear regime featured by optical Kerr effect and multiphoton absorption. We study the conditions for their generation, and we present experimental results confirming the theoretical profiles.

All numerical codes presented in this dissertation were developed and tested during the Ph.D. thesis and were used for simulations and data analysis of experiments carried on by the different groups we had the chance to collaborate with.

Chapter 1

Propagation equations and physical effects

In this chapter we will derive the numerical models describing the propagation of ultrashort laser pulses on which the works of this thesis were based on. In particular, we will refer to two main models: a nonlinear envelope equation for a carrier-envelope formulation and a Forward Maxwell Equation for field propagation.

We will also describe the main nonlinear effects and the relative numerical counterparts involved in the propagation of ultrashort laser pulses. We will briefly go into detail about the process of high harmonic generation.

1.1 Equation governing the nonlinear propagation of laser pulses

Starting from Maxwell-Faraday and Maxwell-Ampère equations in a nonmagnetic dielectric medium:

$$\begin{cases} \nabla \times \mathbf{E} = -\partial_t \mathbf{B} & (1.1) \\ \nabla \times \mathbf{B} = \mu_0 \left(\mathbf{J} + \partial_t \mathbf{D} \right) & (1.2) \end{cases}$$

where $\partial_t \bullet = \partial \bullet / \partial t$, $\mathbf{E}$ and $\mathbf{B}$ are the electric and magnetic fields, $\mathbf{D}$ is the electric displacement field, $\mathbf{J}$ the total current density, and μ_0 the permeability of free space. The electric displacement field is defined as:

$$\mathbf{D} = \epsilon_0 \mathbf{E} + \mathbf{P} \qquad (1.3)$$

with ϵ_0 the vacuum permittivity and $\mathbf{P}$ the polarization density.
The polarization density may be decomposed into the sum of a linear and a nonlinear component. For weak electric field the nonlinear term may be neglected,

while it becomes more and more relevant as the electric field intensity increases. It is useful to write this decomposition in the *temporal* Fourier domain:

$$\hat{\mathbf{P}}(\mathbf{x},\omega) = \epsilon_0 \chi^{(1)}(\omega)\hat{\mathbf{E}}(\mathbf{x},\omega) + \hat{\mathbf{P}}_{NL}(\mathbf{x},\omega) \tag{1.4}$$

where $\chi^{(1)}(\omega)$ is the linear electric susceptibility at frequency (angular frequency) ω of the medium, which is assumed to be *homogeneous*. From Eq. (1.4) the electric displacement is rewritten as:

$$\hat{\mathbf{D}} = \epsilon_0 n^2(\omega)\hat{\mathbf{E}} + \hat{\mathbf{P}}_{NL} \tag{1.5}$$

where $n(\omega) = (1 + \chi^{(1)}(\omega))^{1/2}$ is the frequency-dependent refractive index of the medium.

Applying the curl operator to Eq. (1.1) and combining its temporal Fourier counterpart with Eq. (1.2) and Eq. (1.5), we obtain:

$$\nabla^2 \hat{\mathbf{E}} - \nabla\left(\nabla \cdot \hat{\mathbf{E}}\right) + k^2(\omega)\hat{\mathbf{E}} = \mu_0\left(-i\omega\hat{\mathbf{J}} - \omega^2\hat{\mathbf{P}}_{NL}\right) \tag{1.6}$$

where $k(\omega) = \omega n(\omega)/c$ is the modulus of the wavevector at frequency ω and $c = (\mu_0\epsilon_0)^{-1/2} = 299792458$ m/s the speed of light in vacuum. The corresponding wavelength (in vacuum) is $\lambda = 2\pi c/\omega$.

If the electric field and the fields describing the medium response are assumed to be *linearly polarized in a direction transverse* to the propagation direction z ($\hat{\mathbf{E}} = \hat{E}\mathbf{e}_x$, $\hat{\mathbf{J}} = \hat{J}\mathbf{e}_x$, $\hat{\mathbf{P}}_{NL} = \hat{P}_{NL}\mathbf{e}_x$), the term $\nabla\left(\nabla \cdot \hat{\mathbf{E}}\right)$ may be neglected. This approximation is called the *scalar wave approximation* and it holds for loosely focused linearly polarized electric fields. Equation (1.6) becomes:

$$\left(\partial_{zz}^2 + \nabla_{\perp}^2\right)\hat{E} + k^2(\omega)\hat{E} = \mu_0\left(-i\omega\hat{J} - \omega^2\hat{P}_{NL}\right) \tag{1.7}$$

where $\partial_{zz}^2 = \partial^2/\partial z^2$ and $\nabla_{\perp}^2 = \partial_{xx}^2 + \partial_{yy}^2$.
The real fields E, J and P may be written as the real parts of the complex fields $\mathcal{E}$, $\mathcal{J}$ and $\mathcal{P}$. Moreover, it is possible to include the current contribution in the nonlinear polarization term, by the formal consideration that in the time domain the current term is equivalent to a time derivative of a proper nonlinear polarization term $\mathcal{J} \to \partial_t \mathcal{P}_{cur}$, which becomes in the frequency domain: $\hat{\mathcal{J}} \to -i\omega\hat{\mathcal{P}}_{cur}$. In the following the nonlinear polarization density term will be considered as the sum of the actual polarization density term and this effective polarization contribution.

1.2 Unidirectional Propagation and Forward Maxwell Equation

By performing a Fourier transform over the x, y transverse coordinates of Eq. (1.7) for the complex fields we obtain:

$$\left(\partial_{zz}^2 + k_z^2\right) \tilde{\mathcal{E}}(k_x, k_y, z, \omega) = -\mu_0 \omega^2 \tilde{\mathcal{P}}_{NL}(k_x, k_y, z, \omega) \qquad (1.8)$$

where k_x, k_y represent the transverse components and $k_z = \left[k^2(\omega) - k_x^2 - k_y^2\right]^{1/2}$ the longitudinal component of the wavevector, respectively. In the linear case, when the left hand side of Eq. (1.8) is 0, the general solution for $\tilde{\mathcal{E}}$ is a superposition of two solutions which represent waves propagating in the forward and backward direction:

$$\tilde{\mathcal{E}} = \tilde{\mathcal{E}}^{(+)} + \tilde{\mathcal{E}}^{(-)} = \mathcal{C}^{(+)}(k_x, k_y, \omega)\, e^{ik_z z} + \mathcal{C}^{(-)}(k_x, k_y, \omega)\, e^{-ik_z z} \qquad (1.9)$$

Note that in the nonlinear case the polarization density term acts as a coupling between the two forward- and backward-propagating components. We consider problems in ultrashort nonlinear optics where we can safely neglect the backward propagating component. We are interested in "long" propagation distances compared to the typical laser-matter interaction length. This requires an additional approximation, the *unidirectional propagation approximation*, which consists in considering in the nonlinear term only the contribution given by the forward propagating electric field. This requires that the intensity of the backward-propagating field is negligible with respect to the forward-propagating one, i.e. $|\tilde{\mathcal{E}}^{(-)}| \ll |\tilde{\mathcal{E}}^{(+)}|$. If we formally decompose the operator in the left hand side of Eq. (1.8) into:

$$\left(\partial_z + ik_z\right)\left(\partial_z - ik_z\right)\tilde{\mathcal{E}}(k_x, k_y, z, \omega) = -\mu_0 \omega^2 \tilde{\mathcal{P}}_{NL}(k_x, k_y, z, \omega) \qquad (1.10)$$

the unidirectional approximation implies that $(\partial_z + ik_z) = 2ik_z$, where $\tilde{\mathcal{E}}$ represents now only the forward propagating component and we are assuming $\tilde{\mathcal{P}}_{NL}$ as a function of this forward component $\tilde{\mathcal{E}}$ only.

Going back to Eq. (1.7) for the complex fields, we can apply a similar procedure:

$$\left[\partial_z + ik(\omega)\right]\left[\partial_z - ik(\omega)\right]\hat{\mathcal{E}} = -\nabla_\perp^2 \hat{\mathcal{E}} - \mu_0 \omega^2 \hat{\mathcal{P}}_{NL} \qquad (1.11)$$

and we can retrieve an unidirectional propagation equation under the assumption, as proposed in Ref. [11]: $[\partial_z + ik(\omega)] \sim 2ik(\omega)$.

This implies a further approximation: the *paraxial approximation*. If we write Eq. (1.11) in the linear case in the (k_x, k_y, z, ω) space (by performing a Fourier transform over the transverse coordinates), under this approximation we obtain:

$$\partial_z \tilde{\mathcal{E}}(k_x, k_y, z, \omega) = i \left[k(\omega) - \frac{k_x^2 + k_y^2}{2k(\omega)}\right] \hat{\mathcal{E}}(k_x, k_y, z, \omega) \qquad (1.12)$$

the propagation term inside the brackets in the right hand side is simply an expansion of $k_z = \left[k^2(\omega) - k_x^2 - k_y^2\right]^{1/2}$ for small transverse components. The paraxial approximation therefore implies $(k_x^2 + k_y^2) \ll k(\omega)$. This is equivalent to having small transverse propagation angles. In the nonlinear case we obtain the so-called *Forward Maxwell Equation* (FME) [12]:

$$\partial_z \hat{\mathcal{E}} = i \left(\frac{1}{2k(\omega)} \nabla_\perp^2 + k(\omega) \right) \hat{\mathcal{E}} + i \frac{\mu_0 \omega^2}{2k(\omega)} \hat{\mathcal{P}}_{NL} \qquad (1.13)$$

It is useful to follow the propagation of optical pulses by changing the reference system to the one moving at the velocity of the pulse itself, which for a Gaussian pulse is the *group velocity* $v_g = 1/k_0'$, with $k_0' = \partial_\omega k(\omega = \omega_0)$. The new coordinates thus are:

$$\begin{cases} \zeta = z & (1.14) \\ \tau = t - \dfrac{z}{v} & (1.15) \end{cases}$$

where v is the velocity at which this new reference system is moving. This transformation implies $\partial_z = \partial_\zeta - (1/v)\partial_\tau$ and $\partial_t = \partial_\tau$. In the temporal Fourier domain the reference system change is then:

$$\begin{cases} \partial_\tau = -i\omega & (1.16) \\ \partial_\zeta = \partial_z - i\dfrac{\omega}{v} & (1.17) \end{cases}$$

Equation (1.13) becomes:

$$\partial_\zeta \hat{\mathcal{E}} = i \left(\frac{1}{2k(\omega)} \nabla_\perp^2 + k(\omega) - \frac{\omega}{v} \right) \hat{\mathcal{E}} + i \frac{\mu_0 \omega^2}{2k(\omega)} \hat{\mathcal{P}}_{NL} \qquad (1.18)$$

1.3   Envelope Equations

Starting from Eq. (1.7) for the complex fields, it can be written in the moving reference frame, Eqs. (1.16) and (1.17):

$$\left(\partial_{\zeta\zeta}^2 + 2i\frac{\omega}{v}\partial_\zeta + k^2(\omega) - \frac{\omega^2}{v^2} \right) \hat{\mathcal{E}} = -\nabla_\perp^2 \hat{\mathcal{E}} - \mu_0 \omega^2 \hat{\mathcal{P}}_{NL} \qquad (1.19)$$

We may now decompose the complex electric field into *carrier and envelope* as $\mathcal{E}(x, y, z, t) = A(x, y, z, t) \exp\left(-i\omega_0 t + ik_0 z\right)$, where $k_0 = \omega_0 n(\omega_0)/c$ is the modulus of the wavevector at ω_0, which is assumed to be the central frequency of the pulse. In terms of (ζ, τ) coordinates:

$$\mathcal{E}(x, y, \zeta, \tau) = A(x, y, \zeta, \tau) \exp\left[-i\omega_0\left(\tau + \zeta/v\right) + ik_0\zeta\right] \qquad (1.20)$$

While its temporal Fourier transform is (except for renormalization factors):

$$\hat{\mathcal{E}}(x,y,\zeta,\omega) = \left[\hat{A}(x,y,\zeta,\omega) * \delta(\omega - \omega_0)\right] \cdot \exp\left[i\left(k_0 - \frac{\omega_0}{v}\right)\zeta\right] \qquad (1.21)$$

$$= \hat{A}(x,y,\zeta,\omega = \Omega) \cdot \exp\left[i\left(k_0 - \frac{\omega_0}{v}\right)\zeta\right] \qquad (1.22)$$

where $*$ denotes the convolution operator and $\Omega = \omega - \omega_0$. The temporal spectrum of the pulse, formerly centered at ω_0, is now centered at 0.

Similarly, the complex polarization density may be written in terms of envelope and carrier as $\hat{\mathcal{P}}_{NL}(x,y,\zeta,\omega) = \hat{N}(x,y,\zeta,\omega = \Omega)\exp\left[i\left(k_0 - \omega_0/v\right)\zeta\right]$.

For simplicity of notation, we will use the same notation for $\hat{A}(x,y,\zeta,\omega)$ and $\hat{A}(x,y,\zeta,\omega = \Omega)$, while one should remember to use the former or the latter in the context of complex field or complex envelope, respectively, remembering that this implies $\partial_\tau \leftrightarrow -i\omega$ in the field context and $\partial_\tau \leftrightarrow -i\Omega$ in the envelope context when performing a temporal Fourier transform.

By inserting Eq. (1.22) into Eq. (1.19) we obtain the envelope equation:

$$\left[\partial_{\zeta\zeta}^2 + 2ik_0\hat{U}\partial_\zeta + \nabla_\perp^2\right]\hat{A} + \left(k^2 - k_0^2\hat{U}^2\right)\hat{A} = -\mu_0(\Omega + \omega_0)^2\hat{N} \qquad (1.23)$$

where we set $v = v_g = 1/k_0'$, assuming a reference system moving at the Gaussian pulse group velocity, and $\hat{U}(\Omega) = 1 + k_0'\Omega/k_0$ is called *space-time coupling* operator.

Equation (1.23) may be rewritten as:

$$2ik_0\hat{U}\partial_\zeta\hat{A} = -\nabla_\perp^2\hat{A} - 2k_0\hat{U}\left(k - k_0\hat{U}\right)\hat{A} +$$

$$- \left[\left(k - k_0\hat{U}\right)^2 + \partial_{\zeta\zeta}^2\right]\hat{A} - \mu_0(\Omega + \omega_0)^2\hat{N} \qquad (1.24)$$

and k can be expanded as a function of Ω:

$$k = \sum_{j=1}^{+\infty} \frac{k_0^{(j)}}{j!}\Omega^j, \quad \text{with } k_0^{(j)} = \left.\frac{\partial^j k}{\partial\omega^j}\right|_{(\omega=\omega_0)} \qquad (1.25)$$

We can neglect the third term of the right hand side of Eq. (1.24) with the following assumptions:

- we consider a narrow spectral bandwidth, so that the $O(\Omega^4)$ term $(k - k_0\hat{U})^2$ may be neglect with respect to the $O(\Omega^2)$ term $2k_0\hat{U}\left(k - k_0\hat{U}\right)$;

- we neglect the second order derivative $\partial_{\zeta\zeta}^2\hat{A}$ with respect to the first order term $2ik_0\hat{U}\partial_\zeta\hat{A}$; this approximation, together with the first one, implies

$|\partial_\zeta \hat{A}| \ll |k_0 \hat{A}|$, which means that the envelope of the field evolves over a propagation distance scale greater than $1/k_0 = \lambda/(2\pi n_0)$, hence the name *slowly evolving envelope approximation* (SEEA) [13].

These assumptions in the nonlinear case are at the base of the slowly evolving wave approximation (SEWA) [14].

By neglecting only the second derivative with respect to ζ we reduce to an *Extended Nonlinear Schrödinger* model, which has proved a valid tool for the simulation of ultrashort laser pulses and associated dynamics [15]. By performing the carrier-envelope expansion with the introduction of the $\exp(ik_0 z)$ term, and by neglecting the second order derivative $\partial^2_{\zeta\zeta}\hat{A}$, we are de facto assuming a unidirectional propagation and a paraxial approximation. True non-paraxial model in the form of this equation may be implemented only in the transverse coordinate Fourier domain.

By keeping only the highest order term in the Ω-expansion, i.e. by adopting the *slowly varying envelope approximation* (SVEA), we obtain the equation:

$$\partial_\zeta \hat{A} = i\frac{1}{2k_0}\nabla^2_\perp \hat{A} + i\frac{k_0''}{2}\Omega^2 \hat{A} + i\frac{\omega_0}{2\epsilon_0 n_0 c}\hat{N} \qquad (1.26)$$

which, in the temporal τ domain, becomes:

$$\partial_\zeta A = i\frac{1}{2k_0}\nabla^2_\perp A - i\frac{k_0''}{2}\partial^2_{\tau\tau} A + i\frac{\omega_0}{2\epsilon_0 n_0 c}N \qquad (1.27)$$

In the case of Kerr nonlinearity, which will be discussed in section 1.5.1, this equation with the additional Kerr term is usually referred to as the *Nonlinear Schrödinger Equation* (NLS). This equation, although its approximations (which in general are justified provided that the spectrum does not become too broad), has broad applications for simulating the propagation of optical pulses, see for example [16].

We will now introduce and discuss the linear and nonlinear effects and relative equation terms involved in the propagation of ultrashort laser pulses.

1.4   Linear behavior

The linear behaviors for the field FME and the envelope NLS equation are:

$$\partial_\zeta \hat{\mathcal{E}} = i\frac{1}{2k(\omega)}\nabla^2_\perp \hat{\mathcal{E}} + i\left(k(\omega) - \frac{\omega}{v}\right)\hat{\mathcal{E}} \qquad (1.28)$$

$$\partial_\zeta \hat{A} = i\frac{1}{2k_0}\nabla^2_\perp \hat{A} + i\frac{k_0''}{2}\Omega^2 \hat{A} \qquad (1.29)$$

In particular, the first term in the right hand side represents *diffraction*, while the second one represents *dispersion* of the medium through $k = k(\omega)$, or the second order-only dispersion in the envelope NLS case. The main difference between the first terms of the two equations is the fact that in the second one the approximation $\hat{U} \sim 1$ was carried on. This operator represents the space-time focusing operator, i.e. the fact that wave components at different frequencies exhibit different typical diffraction lengths.

For the monochromatic Gaussian case:

$$\mathcal{E} = A_0 \exp(-(x^2 + y^2)/w_0^2 + i(k_0 z - \omega_0 t))$$

this typical length, called *Rayleigh range*, is indeed proportional to the wavevector at the beam frequency, and to the square of the beam width: $L_{DIFF} = k_0 w_0^2/2$.

Because of the dispersion relation, wavepackets centered at different frequencies will exhibit different group velocities. Since the group velocity at frequency ω is $v = 1/k'(\omega)$, this frequency-dependent variation of the group velocity mainly comes from the second derivative k_0''. This effect is called *group velocity dispersion* (GVD) and it is the responsible of a progressive chirp of optical pulses during propagation. In particular, for *normal* GVD dispersion ($k_0'' > 0$), during propagation an initially transform-limited pulse gains a positive chirp, where lower frequencies concentrates in the leading part and higher frequencies in the trailing part. For *negative* GVD dispersion the pulse develops negative chirp, with opposite frequency distribution. For a Gaussian pulse:

$$\mathcal{E} = A_0 \exp(-t^2/T_p^2 + i(k_0 z - \omega_0 t))$$

the typical length of GVD is proportional to the square of the pulse duration and inversely proportional to the second derivative of $k(\omega)$ at central frequency ω_0: $L_{GVD} = T_p^2/(2k_0'')$.

1.5 Nonlinear terms

We will now briefly report the most common case for the nonlinear terms we may encounter in the propagation of optical pulses and their representation.

1.5.1 Kerr effect

The optical Kerr effect arises when the nonlinear polarization density is proportional to the third power of the electric field. In particular, when the intensity of the electric field is high enough that the medium response is no longer linear, this third order term is the first to appear in materials with central symmetry (the E^2 term is forbidden for symmetry constraint).

The optical Kerr effect gives rise to two main effects:

- third harmonic generation;

- self-phase modulation and self-focusing.

Indeed, if we write the electric field in a carrier-envelope decomposition: $E = 1/2 \cdot A \exp\left[ik_0 z - i\omega_0 t\right] + \text{C.C.}$, the third order polarization $P_{NL} = \epsilon_0 \chi^{(3)} E^3$ becomes:

$$P_{NL} = \epsilon_0 \frac{\chi^{(3)}}{8} \left[A^3 e^{i3k_0 z - i3\omega_0 t} + 3|A|^2 A e^{ik_0 z - i\omega_0 t} + \text{C.C.}\right] \tag{1.30}$$

The first term of the right hand size of Eq. (1.30) describes a wave oscillating at $3\omega_0$ and is responsible for third harmonic generation, while the second one may be interpreted as an effective linear polarization term in which the refractive index is proportional to the intensity of the electric field.
This effect is usually written as (see for example [17]):

$$n(I) = n_0 + n_2 I(r, t) \tag{1.31}$$

where n_2 is a coefficient which depends on the specific medium (in general it is possible to consider n_2 as a complex number; the following considerations are for the real part of this coefficient, usually positive).
By writing Eq. (1.30) in terms of the complex polarization density and considering only the term oscillating at frequency ω_0, by using the relation between the squared modulus of the field and the light intensity $I = \epsilon_0 n_0 c |\mathcal{E}|^2 / 2$, we have $\mathcal{P}_{NL} = (3/2)\chi^{(3)} I A / (c n_0) = \epsilon_0 \epsilon_{NL}(I) A$.
The refractive index is $n_{NL} = (1 + \chi^{(1)}(\omega_0) + \epsilon_{NL}(I))^{1/2} \simeq n_0 + \epsilon_{NL}(I)/(2n_0)$, with n_0 the (linear) refractive index at ω_0, we thus obtain the relation: $n_2 = 3\chi^{(3)}/(4\epsilon_0 c n_0^2)$.
By means of this relation is then possible, from the values for n_2, to reconstruct the relative value of $\chi^{(3)}$, which can also be used in the field equation.
The Kerr term in the envelope equation is:

$$\partial_\zeta A = i\frac{1}{2k_0}\nabla_\perp^2 A - i\frac{k_0''}{2}\partial_{\tau\tau}^2 A + i\frac{\omega_0}{c}n_2 I A \tag{1.32}$$

where the third harmonic contribution has been neglected.
This intensity-dependent variation of n occurs in a very short time (of the order of the electronic cloud response time $\sim 10^{-16}$ s) and the light itself is affected by this modification of the refractive index in the form of a self-modulation of the temporal or spatial phase.

A plane wave traveling along the z axis for a length L suffers a phase variation:

$$\delta\varphi = \delta\varphi_0 + \frac{\omega_0}{c}n_2 I L$$

where $\delta\varphi_0$ is the phase variation in the absence of nonlinear effects.
The third-order nonlinearity thus determines a phase delay proportional to the instantaneous intensity of the wave, that, in the most general case, has a spatio-temporal distribution $I = I(r,t)$. This determines the phenomena of *self-phase modulation* and *self-focusing*.

Self-phase modulation - In the case of a light pulse centered at frequency ω_0, it is possible to consider the instantaneous frequency along the pulse as the first derivative of the phase $\varphi(t)$ with respect to time. For a propagation along a distance L the instantaneous frequency in the presence of the Kerr nonlinearity is given by:

$$\omega_{inst} = \partial_t(\omega_0 t - \delta\varphi) = \omega_0 - \frac{\omega_0}{c}n_2 L \partial_t I \qquad (1.33)$$

Since the intensity of a light pulse does exhibit a temporal profile, Eq. (1.33) determines the generation of new frequencies: this process is called *self-phase modulation* (SPM).
In particular, since n_2 is usually positive, the leading part $(\partial_t I > 0)$ generates lower frequencies, while higher frequencies are generated in the trailing part of the pulse.

Self-focusing - If one considers a Gaussian transverse intensity profile inside Eq. (1.31) $(n_2 > 0)$, the refractive index in the center of the beam, where the intensity is higher, is greater than the index seen by the tails of the beam: the material acts as a focusing lens, with the difference that the effect is cumulative in propagation. This spatial counterpart of the self-phase modulation leads to the so-called *self-focusing* (SF) for $n_2 > 0$ and self-defocusing for $n_2 < 0$.

The characteristic length for spatial self-phase modulation is defined as the length over which the accumulated phase, measured by the B-integral ($B = (\omega_0/c)\int_0^L n_2 I dz$), varies by a factor of one:

$$L_{SF} = \frac{c}{n_2\omega_0 I_0}$$

with I_0 the peak intensity.
An intense collimated beam traveling through a Kerr medium starts to contract because of self-focusing; this determines an increase of the peak intensity and the effect becomes stronger and stronger (the focal length of the "effective" lens becomes smaller). Since the diameter of the beam decreases also diffraction becomes stronger.

In the case of a continuous laser Gaussian beam, self-focusing overcomes diffraction if the initial power $\mathbb{P}_{in}$ is greater than a critical threshold power:

$$\mathbb{P}_{thr} = \frac{3.77\pi n_0}{2k_0^2 n_2}$$

In this case the beam collapses (for 2-dimensional spatial propagation) after a distance given by the semi-empirical formula [18]:

$$L_C(\mathbb{P}_{in}) = \frac{0.367 L_{DIFF}}{\left[\left(\sqrt{\mathbb{P}_{in}/\mathbb{P}_{thr}} - 0.852\right)^2 - 0.0219\right]^{1/2}}$$

where $L_{DIFF} = k_0 w_0^2/2$ is the Rayleigh range associated to the central frequency of the pulse.

1.5.2 Nonlinear absorption

The collapse predicted for the pure Kerr case is prevented in real experiments by saturation mechanisms, which lower the total energy (and therefore limit the intensity) of the beam and/or defocus the beam itself.

In particular, close to the collapse point, the intensity becomes high enough to trigger ionization of the medium by means of nonlinear absorption. *Multiphoton absorption* is the process in which an electron absorbs two or more photons and achieves an excited state (passing through a "virtual" state which does not correspond to any electronic or vibrational state). If the energy absorbed is high enough to make it a free electron the process is called multiphoton ionization. The number of photons of frequency ω_0 required for ionization is $K = \lceil U_i/\hbar\omega_0 \rceil$ (where $\lceil \cdots \rceil$ is the ceiling function) with U_i the ionization potential or band-gap for condensed media (for example, $K = 8$ for air at wavelength $\lambda_0 = 800$ nm).

Nonlinear absorption is described by a current $\mathcal{J}$ such that the averaged dissipated power corresponds to the one necessary for the optical field ionization of the medium. In general, ionization is described by an intensity-dependent ionization rate $W(I)$.
Multiphoton ionization is just one particular case of ionization regime, with rate $W(I) = \sigma_K I^K$, and σ_K the cross section for this process.
The energy conservation condition reads:

$$\frac{1}{2}\mathcal{J} \cdot \mathcal{E}^* = W(I)K\hbar\omega_0(\rho_0 - \rho) \tag{1.34}$$

where ρ_0 is the initial density of neutral atoms and ρ is the free electron density. The current is therefore:

$$\mathcal{J} = \frac{W(I)}{I}Kn_0\epsilon_0 c\hbar\omega_0(\rho_0 - \rho)\mathcal{E} \tag{1.35}$$

Equation (1.35) for the multiphoton absorption case in the envelope formulation is then:

$$\mathcal{J}_{env} = n_0\epsilon_0 c\beta^{(K)}\left(1 - \frac{\rho}{\rho_0}\right)I^{K-1}A \tag{1.36}$$

where $\beta^{(K)} = \sigma_K K\hbar\omega_0\rho_0$ is the multiphoton absorption cross section. The corresponding term in the envelope equation, derived by means of the formal identity $\hat{\mathcal{J}} = i\hat{\mathcal{P}}_{NL}/\omega$ becomes:

$$\partial_\zeta A = i\frac{1}{2k_0}\nabla_\perp^2 A - i\frac{k_0''}{2}\partial_{\tau\tau}^2 A - \frac{\beta^{(k)}}{2}\left(1 - \frac{\rho}{\rho_0}\right)I^{K-1}A \tag{1.37}$$

1.5.3 Plasma effects

The plasma of free electrons generated by the high intensity peak contributes to the arrest of the collapse by two main processes:

- it locally reduces the refractive index [19];

- it can be further accelerated by the electric field in an inverse Bremsstrahlung effect, therefore lowering the intensity by means of this absorption effect [20].

The effect of plasma may be treated following the *Drude model*, in which the plasma of free electrons is treated as a fluid. The corresponding current obeys the equation:

$$\partial_t \mathcal{J} = -\frac{\mathcal{J}}{\tau_c} + \frac{q_e^2}{m_e}\rho\mathcal{E} \tag{1.38}$$

where τ_c is the electron collision time, ρ is the electron density, q_e and m_e are the electron charge and mass, respectively (in condensed media this m_e is replaced by the reduced mass).

In the temporal Fourier space Eq. (1.38) gives:

$$\hat{\mathcal{J}} = \frac{\tau_c q_e^2}{m_e}\frac{1 + i\omega\tau_c}{1 + \omega^2\tau_c^2}\widehat{\rho\mathcal{E}} \tag{1.39}$$

The corresponding term in Eq. (1.18) is:

$$-\frac{\omega}{2k(\omega)\epsilon_0 c^2}\hat{\mathcal{J}} = -\frac{\sigma(\omega)}{2}\widehat{\rho\mathcal{E}} \tag{1.40}$$

with

$$\sigma(\omega) = \frac{\omega_0}{n(\omega)c\rho_c}\frac{\omega_0\tau_c\left(1 + i\omega\tau_c\right)}{1 + \omega^2\tau_c^2} \tag{1.41}$$

and $\rho_c = \epsilon_0 m_e \omega_0^2/q_e^2$ the critical plasma density above which the plasma becomes opaque to the laser beam at the reference frequency ω_0.

The real and imaginary part of $\sigma(\omega)$, Eq. (1.41), account for plasma absorption (real part), and plasma defocusing and phase modulation (imaginary part).

When $\omega_0\tau_c \gg 1$, for example in gases where at $\lambda_0 = 800$ nm, $\tau_c \sim 200$ fs, we can approximately consider only the imaginary term of Eq. (1.41). In the approximation $\omega \simeq \omega_0$, this leads to a local change of the refractive index:

$$n \simeq n_0 - \frac{\rho(r,t)}{2n_0\rho_c} \tag{1.42}$$

Since the density of free electrons is higher in the central part of the beam (where intensity is higher), the overall effect is that plasma acts as a defocusing lens. This process involves especially the trailing part of the pulse [21] where the plasma density is higher.

The generation of plasma also contributes to spectral broadening and shift toward higher frequencies, since the instantaneous frequency may be written as:

$$\omega_{inst} = \partial_t\varphi = \omega_0 + \frac{\omega_0 L}{2n_0 c\rho_c}\partial_t\rho \tag{1.43}$$

The free electron density evolves according to the rate equation:

$$\partial_t\rho = W_{\text{ofi}}(I)\left(\rho_0 - \rho\right) + W_{\text{ava}}(I)\rho \tag{1.44}$$

where the first term in the right hand side represents optical field ionization, described in the previous section, while the second one accounts for avalanche ionization, $W_{\text{ava}}(I) = \Re\left\{\sigma(\omega_0)\right\} I/U_i$, in which $\Re\left\{\sigma(\omega_0)\right\}$ is the cross section for inverse Bremsstrahlung at the central frequency ω_0, given by Eq. (1.41), and U_i is the ionization potential. In this case recombination of the electrons was neglected.

1.5.4   Raman effect

The optical Kerr effect has two contributions: an electronic response with a typical time response below 1 fs, described in section 1.5.1, and a slower response ($\sim$ ps or hundreds of ps) due to the excitation of rotational and/or vibrational levels of the molecules. This delayed component is called *Raman effect*. Because of the response time scale, this effect is weak for shorter pulses, while it becomes more important for long pulses ($\gtrsim 1$ ps).

Despite having a different origin with respect to the actual Kerr effect, the Raman contribution appears as a third order term in the polarization density, thus making it difficult to distinguish from the former effect in the case of relatively long pulses.

The Raman response is effectively described as a term:

$$\mathcal{P}_{NL} \propto Q_R(t)\mathcal{E} \tag{1.45}$$

with the Raman response function Q_R obeying an equation of forced and damped oscillator:

$$\partial_{tt}^2 Q_R + 2\Gamma\partial_t Q_R + \left(\omega_R^2 + \Gamma^2\right)Q_R = \left(\omega_R^2 + \Gamma^2\right)|\mathcal{E}|^2 \tag{1.46}$$

where Γ is a phenomenological damping rate and ω_R the fundamental rotational frequency. We also require $Q_R, \partial_t Q_R \to 0$ for $t \to -\infty$ (i.e. no Raman response before the interaction of the medium with the light pulse).
Equation (1.46) has solution:

$$Q_R(t) = \int_{-\infty}^{t} \mathcal{R}(t - \vartheta)\,|\mathcal{E}(x, y, z, \vartheta)|^2\,\mathrm{d}\vartheta \tag{1.47}$$

with

$$\mathcal{R}(t) = \frac{\omega_R^2 + \Gamma^2}{\omega_R}\exp\left(-\Gamma t\right)\sin\left(\omega_R t\right)$$

The nonlinear polarization for the Kerr and Raman term therefore reads as:

$$i\frac{\omega_0}{2\epsilon_0 n_0 c}N = i\frac{\omega_0}{c}n_2\left[(1 - \alpha)I(x, y, \zeta, \tau)\ +\right.$$
$$\left.+\ \alpha\int_{-\infty}^{\tau}\mathcal{R}(\tau - \vartheta)I(x, y, \zeta, \vartheta)\,\mathrm{d}\vartheta\right]A \tag{1.48}$$

where $0 \le \alpha \le 1$ is a phenomenological parameter which describes the fraction of third order nonlinearity pertaining to the Raman effect.

1.5.5   Self-steepening

The process of self-steepening occurs because of the intensity-dependent refractive index: this implies that the velocity of the intensity peak of the pulse is smaller than the velocity of the wings, which determines a steep edge in the trailing edge since the back part of the pulse catches up the peak [22]. A shock front is formed in correspondence of this edge and self-phase modulation brings an increase in the generation of bluer frequency.

The self-steepening effect is mathematically described by the frequency-dependence of the prefactor of the nonlinear term in Eqs. (1.18) and (1.24). If we keep all the dispersion order, and the first order Ω factors in the envelope equation,

we obtain an extended nonlinear envelope equation, widely used for simulating the filamentation regime [15]:

$$
\begin{cases}
\hat{U}\partial_\zeta \hat{A} = \dfrac{i}{2k_0}\nabla_\perp^2 \hat{A} + \dfrac{ik_0}{2}\left(\dfrac{k^2(\omega)}{k_0^2} - \hat{U}^2\right)\hat{A} + \hat{N}(A) & (1.49) \\[2ex]
N(A) = i\dfrac{\omega_0 n_2}{c}T^2\left[(1-\alpha)I + \alpha\displaystyle\int_{-\infty}^{\tau}\mathcal{R}(\tau-\vartheta)I(\vartheta)\,\mathrm{d}\vartheta\right]A + \\[2ex]
\qquad\quad - T\dfrac{\beta^{(K)}}{2}\left(1 - \dfrac{\rho}{\rho_0}\right)I^{K-1}A - \dfrac{\sigma(\omega_0)}{2}\rho A & (1.50)
\end{cases}
$$

where the operators $\hat{U}(\Omega) = 1 + (k_0'\Omega/k_0)$ and $\hat{T}(\Omega) = 1 + (\Omega/\omega_0)$, with corresponding expressions in the direct space $U = 1 + i(k_0'/k_0)\partial_\tau$ and $T = 1 + (i/\omega_0)\partial_\tau$, represent space-time focusing and self-steepening, respectively.

1.5.6 Optical field ionization

As already mentioned in section 1.5.2, multiphoton absorption is only a particular process by which ionization may happen. For example, for intense electric fields the ionization is usually regarded to happen through a *tunneling* process.

In general, when the intensity of light interacting with matter is high enough, the strength of the electric field of the light may become comparable with the atomic electric field, so that the contribution from the incoming light to the total potential experienced by the electron $V(\mathbf{r},t) = -q_e^2/(4\pi\epsilon_0 r) + \mathbf{E}(t)\cdot\mathbf{r}$ (r radial coordinate and $\mathbf{r}$ position with respect to the atomic nucleus) severely distorts the Coulomb potential. A potential barrier is created (see Fig. 1.1 for a schematic representation) and the electron can escape the binding potential by mean of a tunneling effect.

A theoretical description of ionization rates for such a process was first proposed by Keldysh [23] in the quasi-static limit, i.e. when the time scale for ionization is much faster than the period of the incoming laser light. In particular, within this framework, one may identify two different regimes, depending on the *Keldysh parameter*:

$$
\gamma = \sqrt{\frac{U_i}{2U_p}} \qquad U_p = \frac{q_e^2 E_0^2}{4m_e\omega_0^2} \tag{1.51}
$$

where U_p is the *ponderomotive energy*, depending on the amplitude E_0 and frequency ω_0 of the electric field.

When $\gamma \gg 1$ the ionization occurs mainly due to multiphoton absorption, while in the opposite case $\gamma \ll 1$ tunneling ionization is the dominant process. Indeed, for very low light intensities the Coulomb potential is essentially not affected by
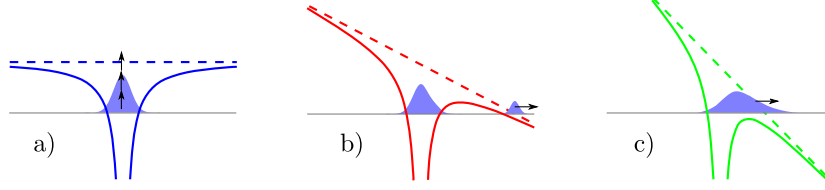
Figure 1.1: Schematic representations of three ionization regimes. a) multiphoton ionization, when $\gamma \gg 1$. b) tunnel regime, when the incoming field is strong enough to significantly modify the Coulomb potential and the laser frequency is low enough such that the electron can respond to this changing potential, $\gamma \ll 1$; in this case ionization can be understood as the tunneling through a static potential wall. c) above-barrier ionization, when the field is high enough to suppress the potential barrier.

the incoming electric field, while for high oscillation frequencies the quasi-static treatment does not hold and the motion of the electron will be governed by a cycled-average of the laser field rather than tunneling in a single cycle. In the limit case in which the field of the laser is high enough to suppress the barrier [Fig. 1.1(c)], the electron is classically "ripped off" the atom in an *above-barrier ionization* [24].

The original Keldysh formulation for the hydrogen atom was then generalized in the works of Perelomov, Popov and Terent'ev (PPT) [25–27], while the tunnel limit was investigated and a general formula for arbitrary atoms and initial electronic states was obtained by Ammosov, Delone and Krainov (ADK) [28].

The *cycled averaged* ADK tunnel ionization rates for a sinusoidal electric field $E(t) = E_0 \cos(\omega_0 t)$ read as, with all quantities expressed in *atomic units* ($\hbar = m_e = q_e = 1$):

$$\overline{W}_{ADK}(E_0) = \left(\frac{3e}{\pi}\right)^{3/2} \frac{Z^2}{n^{*9/2}} \left(\frac{4eZ^3}{n^{*4}E_0}\right)^{2n^* - \frac{3}{2}} \exp\left(-\frac{2Z^3}{3n^{*3}E_0}\right) \qquad (1.52)$$

where $e = 2.7182818\ldots$ is Euler's number (or Napier's constant), Z is the charge of the resulting ion, $n^* = Z/(2U_i)^{1/2}$ is the effective principal quantum number. The instantaneous rate W_{ADK} is linked to the averaged rate, $\overline{W}_{ADK}$, by substituting E_0 with $|E(t)|$ and (in atomic units):

$$W_{ADK}(E(t)) = \left(\frac{3|E(t)|}{\pi(2U_i)^{3/2}}\right)^{-1/2} \overline{W}_{ADK}(E(t)) \qquad (1.53)$$

In general the ionization rates do not depend on the relative sign of the electric field, therefore we will write indiscriminately $W_{ADK}(E(t))$ or $W_{ADK}(E^2(t))$. By mean of the ADK expression of $W(E^2)$, or the more general Keldysh-PPT rate revised by Ilkov, Decker and Chin [29], it is possible to evaluate nonlinear absorption and plasma density evolution from Eqs. (1.35) and (1.44), by considering the

instantaneous field (in proper units) instead of the cycled-averaged intensity in the rate expression. It is worth noting that the ADK formulation has been shown to remain valid close to the limit $\gamma \ll 1$, and to be still valid up to $\gamma \lesssim 0.5$ [29].

Figure 1.2 shows the ionization rates for oxygen and argon computed from the full Keldysh-PPT formulation (in the O_2 case with a prefactor for diatomic molecules from Ref. [30]), for $\lambda_0 = 800$ nm. Ionization rates from the complete Keldysh-PPT formulation are shown by the continuous curve for oxygen and by the dash-dotted curve for argon. The figure clearly shows that the multiphoton ionization rates $\propto I^K$ for oxygen (blue dotted line, $K = 8$ at $\lambda_0 = 800$ nm) are a good approximation of the full rates for intensities lower than $\sim 5 \times 10^{12}$ W/cm^2, while the ADK rates (green dashed line) overlap with the Keldysh-PPT formulation for intensities above 4×10^{13} W/cm^2. The Keldysh-PPT curve for argon is similar, with a behavior dominated by multiphoton absorption ($K = 11$) at lower intensities and a tunnel regime described by the ADK rates for higher intensities. The Keldysh parameter $\gamma = 1$ corresponds to $I = 1.3 \times 10^{14}$ W/cm^2 for the argon case and 1.1×10^{14} W/cm^2 for the oxygen case.
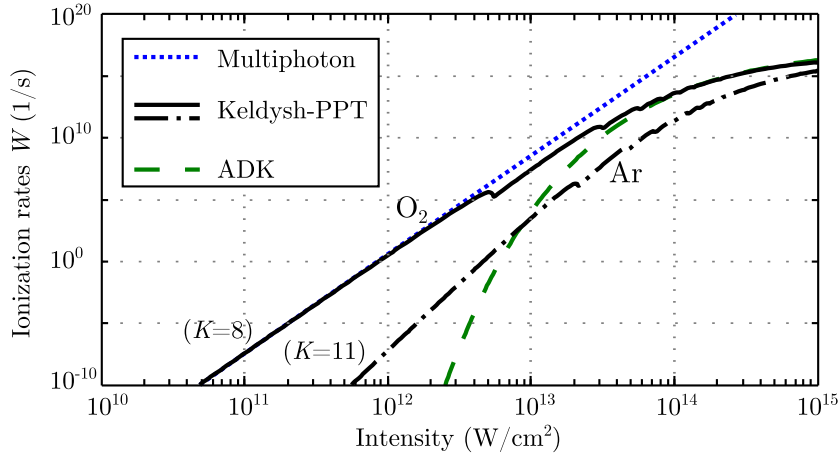
Figure 1.2: Cycled-averaged ionization rates for oxygen (continuous curve) and argon (dash-dotted curve) as a function of laser intensity at $\lambda_0 = 800$ nm. By comparison, the blue dotted line and the green dashed line show the multiphoton ionization rate and the ADK rate for oxygen, respectively. In brackets the relative multiphoton order approximating the behavior before entering the tunnel regime.

1.6   High harmonic generation

High harmonic generation (HHG) is a highly nonlinear process in which laser light at frequency ω_0, usually in the near infrared region, generates a series of

integer odd-multiples of ω_0 during the interaction with a medium, with a final spectrum in the shape of a frequency comb [Fig. 1.3(a)] spanning from the visible range to the extreme ultraviolet (XUV), or even soft X-rays [31].

HHG in gas was first reported in the late 1980s [32, 33]. A striking feature in this process was the fact that, instead of a rapid decrease in efficiency with increasing harmonic order, the spectrum exhibited an initial decrease in agreement with a perturbative approach, then a relatively flat *plateau*, i.e. an extended spectral region with equally intense harmonics spanning over many orders, and finally an abrupt *cut-off*, as shown in Fig. 1.3(b) and 1.3(c).
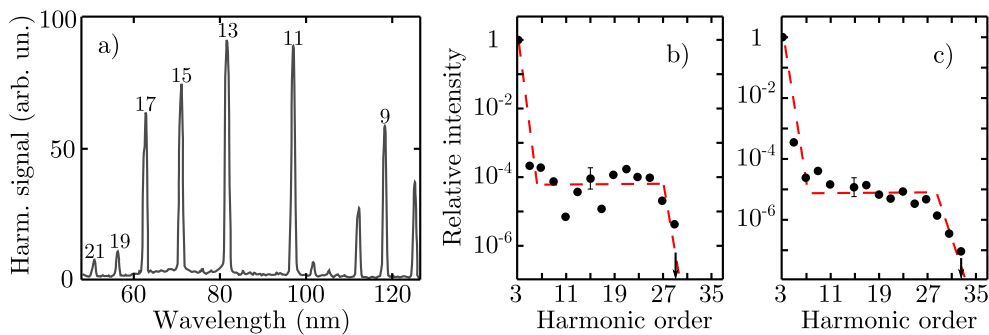
Figure 1.3: Typical examples of harmonic spectra, from [33]. a) HHG from a 10 Torr Xe gas jet, showing the frequency comb of odd harmonics between the 9th and the 21st. b) Relative intensity of the harmonics generated in Kr at a laser intensity of $\sim 3 \times 10^{13}$ W/cm^2 and c) for Ar gas. The arrows indicate the highest harmonic orders observed in the two cases. The red dashed lines approximatively highlight the initial perturbative region (rapid intensity decrease), the plateau of almost equally intense harmonics and the cutoff region.

A first, semi-classical approach which explained this experimentally found behavior was proposed in 1993 by Corkum [34] and Kulander, Schafer, Krause [35], known as the *three-step model*.

1.6.1   The three-step model

The three-step model, as the name suggests, describes the process of HHG as a sequence of three main steps: *ionization*, *acceleration* in the electric field and *recollision*.

Ionization. This step has already been discussed in section 1.5.6. In particular, when the intensity of the incoming light is high enough, the electron can escape the binding potential through a tunnel ionization process. The electron is then treated as a free particle. In fact, this process is more likely to happen when the absolute electric field of the laser light is close to its peak during the optical cycle.

Acceleration. After the electron has been ionized, it can be approximately treated as a free particle subject to the electric field of the laser light. In the classical treatment, the electron can be considered as a classical particle subject to the (scalar) electric field $E(t) = E_0 \cos(\omega_0 t + \phi)$, where ϕ is the phase of the electric field when the electron is ionized; if the electron is supposed to appear in the continuum at $x = 0$ with zero initial drift velocity, its velocity and position are governed by the equations:

$$\begin{cases} v(t) = \int_0^t -\dfrac{q_e E(\tau)}{m_e} \, \mathrm{d}\tau = -\dfrac{q_e E_0}{m_e \omega_0} \left[\sin(\omega_0 t + \phi) - \sin(\phi) \right] & (1.54) \\[3mm] x(t) = \int_0^t v(\tau) \, \mathrm{d}\tau = \dfrac{q_e E_0}{m_e \omega_0^2} \left[\cos(\omega_0 t + \phi) - \cos(\phi) + \omega_0 t \sin(\phi) \right] & (1.55) \end{cases}$$

The amplitude of position oscillation (ponderomotive radius) $x_0 = q_e E_0/(m_e \omega_0^2)$ for typical laser intensities $\sim 10^{14}$ W/cm^2 is of the order of the nanometer, larger than typical atomic radius, thus confirming the validity of the approximation of the electron as a free particle inside the laser field.

From Eq. (1.54) it is easily seen that the ponderomotive energy U_p is the average kinetic energy acquired by the electron for $\phi = 0$, i.e. when it is ionized in correspondence of the peak of the electric field. The time-independent term in Eq. (1.54) is a drift velocity, which can prevent the trajectory to come back to the initial position $x = 0$, as shown in Fig. 1.4(a), where the electron can recombine with the parent ion and emit, in the third step of the HHG process, the energy acquired under the influence of the field plus the ionization potential U_i. Only the first two encounters of the electron with the ion actually lead to significant photon emission; this is due to the quantum-mechanical nature of the electron, whose wavepacket undergoes diffraction during propagation (and the overlap with the atom becomes smaller).

Recollision. As already said, when electron during its trajectory encounters again the ion, it can recombine and emit the kinetic energy E_{kin} it acquired during propagation together with the ionization potential as a photon of frequency ω_H:

$$\hbar \omega_H = E_{kin} + U_i \qquad (1.56)$$

By combining Eqs. (1.54) and (1.55) it is possible to evaluate the kinetic energy at the first recombination time (i.e. when $x(t) = 0$), as shown in Fig. 1.4(b). In particular, the kinetic energy reaches a maximum $\simeq 3.17 U_p$ corresponding to the initial electric field phase $\phi \simeq 0.31333$ rad ($\phi \simeq 18°$). The maximum emitted photon energy is thus:

$$\hbar \omega_H = 3.17 U_p + U_i \qquad (1.57)$$

This corresponds to the maximum photon frequency emitted and therefore it describes the cut-off. This cut-off prediction is in very good agreement with the
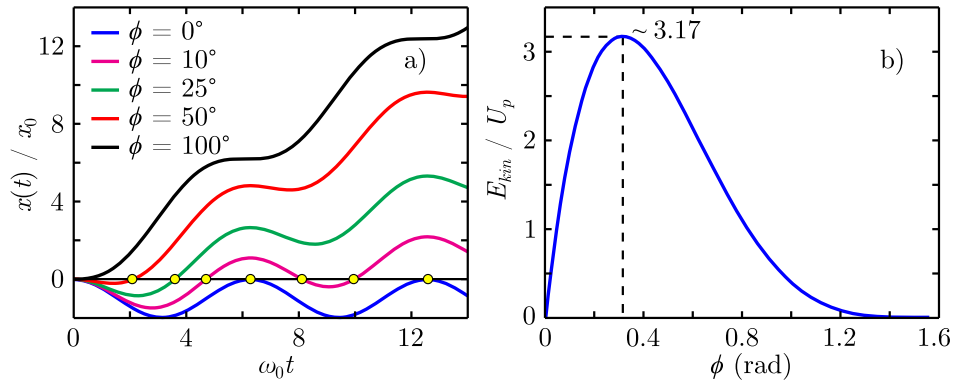
Figure 1.4: a) Trajectories of a classical electron subject to an oscillating electric field: distance (normalized to the amplitude of oscillations x_0) versus time (normalized by ω_0), for different initial phase ϕ of the electric field. Only some of the trajectories re-encounter the atom at the initial position $x = 0$ (underlined by the yellow circles). b) Kinetic energy [proportional to the square of the slope values of curve a)] at the first re-encounter points [intersection points with $x = 0$] for the classical trajectories, as a function of the initial phase of the field. A maximum of $\sim 3.17 U_p$ is reached at $\phi \simeq 0.31333$ rad $\simeq 18°$.

experiments [34]. Equation (1.57) is thus called *cut-off law* and it was empirically derived before its theoretical demonstration [36].

Since the three-step process and the associated photon emission happens every half-cycle of the laser field (the maximum ionization occurs around the maxima of the absolute value of the field), the output signal will comprise a series of light bursts separated by roughly half an optical period. The output spectrum will thus consist in a series of discrete peaks with separation $2\omega_0$. These will be odd multiples of ω_0 because of inversion symmetry.

Another implication of the three-step model is that HHG may occur only for linearly polarized electric field. Under an elliptically polarized field indeed the classical electron is no more able to return to its initial position, therefore "missing" the parent ion. From a quantum-mechanical point of view this corresponds to a reduced overlap of the electron wavepacket with the atom. This effect has been observed experimentally, demonstrating a rapid decrease of harmonics intensity for increasing ellipticity [37, 38].

1.6.2 Quantum-mechanical model

A fully quantum-mechanical treatment of the classical three-step model was introduced by Lewenstein *et al.* in 1994 [39], and a derivation for elliptical polarization by Antoine *et al.* in 1996 [40].

This quantum model is called *strong field approximation* (SFA). It evaluates the atomic dipole response $\mu(t)$ for one single electron wavefunction (*single-active electron approximation*), and the associated nonlinear polarization is then $P_{NL} = [\rho_0 - \rho(t)]\mu(t)$, with $[\rho_0 - \rho(t)]$ the density of neutral atoms.
The model is based upon the following approximations:

- the contribution to the evolution of the system mainly comes from $|0\rangle$, the ground state of the atom;

- the depletion of the ground state can be neglected;

- after ionization, in the continuum the electron is treated as a free particle (neglecting the Coulomb potential).

The Schrödinger equation for the electron wavefunction $|\psi\rangle$ is, in *atomic units*:

$$i\partial_t |\psi(\mathbf{r}, t)\rangle = \left[-\frac{1}{2}\nabla^2 + V_C(\mathbf{r}) - E_0 \cos(\omega_0 t)x \right] |\psi(\mathbf{r}, t)\rangle \quad (1.58)$$

where $V_C(\mathbf{r})$ is the atomic Coulomb potential, and the light electric field is linearly polarized along x-direction.

Under the previous assumptions, the time-dependent wavefunction can be expanded as

$$|\psi(t)\rangle = \exp(iU_i t) \left(a(t)|0\rangle + \int d^3\mathbf{v} \, b(\mathbf{v}, t)|\mathbf{v}\rangle \right) \quad (1.59)$$

where $a(t)$ is the amplitude of the ground state, which is assumed to be $a(t) \simeq 1$ since the depletion is neglected; $b(\mathbf{v}, t)$ is the amplitude of the continuum state $|\mathbf{v}\rangle$ characterized by momentum $\mathbf{v}$. Free oscillations of the ground state were factored out.

Following Ref. [39], the x-component of the dipole moment $\mu(t) = \langle\psi(t)| - x|\psi(t)\rangle$ reads:

$$\mu(t) = i \int_0^t dt' \int d^3\mathbf{p} \, \underbrace{E_0 \cos(\omega_0 t')}_{(a)} \times \underbrace{d_x(\mathbf{p} - \mathbf{A}(t'))}_{(a)} \times \underbrace{\exp\left(-iS(\mathbf{p}, t, t')\right)}_{(b)} \times$$

$$\times \underbrace{d_x^*(\mathbf{p} - \mathbf{A}(t))}_{(c)} + \text{C.C.} \quad (1.60)$$

where $\mathbf{A}(t) = -\int_{-\infty}^t dt' \, \mathbf{E}(t')$ is the vector potential of the laser field, $\mathbf{p} = \mathbf{v} + \mathbf{A}(t)$ is the canonical momentum; $d_x(\mathbf{v})$ is the x-component (parallel to the

polarization axis) of the atomic dipole matrix element for the bound-free transition $\mathbf{d}(\mathbf{v}) = \langle \mathbf{v} | \mathbf{r} | 0 \rangle$. S is the so-called quasi-classical action:

$$S(\mathbf{p}, t, t') = \int_{t'}^{t} dt'' \left(\frac{[\mathbf{p} - \mathbf{A}(t'')]^2}{2} + U_i \right) \tag{1.61}$$

which represents the phase advance of the electron during the time it spends in the continuum. The equation can be generalized by substituting the sinusoidal field $E_0 \cos(\omega_0 t')$ with the electric field $E(t')$.

Equation (1.60) has a physical interpretation as a sum over the possible quantum paths of the probability amplitudes corresponding to three main processes:

(a) *ionization*: transition from the ground state at time t' to the continuum state with canonical momentum $\mathbf{p}$;

(b) *propagation in the continuum* between t' and t; the electron is treated as a free particle and the effect of the binding potential is retained only through the dependence on U_i;

(c) *recombination* to the ground state at time t.

Therefore, the quantum treatment closely resembles the three-step model.

The main contribution to the momentum integral in Eq. (1.60) comes from the stationary points of the semi-classical action:

$$\nabla_{\mathbf{p}} S(\mathbf{p}, t, t') = 0 \tag{1.62}$$

This requirement can be interpreted in the three-step model context by considering that $\nabla_{\mathbf{p}} S(\mathbf{p}, t, t') = \mathbf{r}(t) - \mathbf{r}(t')$, so that the stationary points correspond to electron trajectories that return at time t to the same position where they were ionized at time t', i.e. the main contribution comes from electrons which tunnel away from the nucleus and then re-encounter it while oscillating in the laser field. Equation (1.60) thus becomes

$$\mu(t) = 2\Re \left\{ i \int_{-\infty}^{t} dt' \left(\frac{\pi}{\epsilon + i(t - t')/2} \right)^{3/2} d_x^*(p_{st}(t, t') - A(t)) \times \right.$$

$$\left. \times E(t') \times d_x(p_{st}(t, t') - A(t')) \times \exp[-iS_{st}(t, t')] \right\} \tag{1.63}$$

The stationary values of the x-component of the momentum $p_{st}(t, t')$ and action integral along the trajectory $S_{st}(t, t')$ are

$$p_{st}(t, t') = \frac{1}{t - t'} \int_{t'}^{t} A_x(t'') \, \mathrm{d}t'' \tag{1.64}$$

$$S_{st}(t, t') = (t - t') \left(U_i - \frac{p_{st}^2}{2} \right) + \frac{1}{2} \int_{t'}^{t} A_x^2(t'') \, \mathrm{d}t'' \tag{1.65}$$

where A_x is the non-zero component of the vector potential for the electric field linearly polarized along x.

The first term of Eq. (1.63), with ϵ an infinitesimal positive regularization constant, arises from the regularized Gaussian integration over $\mathbf{p}$, and represents the quantum diffusion, i.e. the spread of the electronic wavepacket in the continuum. This term cuts the contribution from trajectories with large recombination times, that is large $(t - t')$.

For hydrogen-like atoms the dipole matrix element takes the form [41]:

$$\mathbf{d}(\mathbf{p}) = i \frac{2^{7/2} (2U_i)^{5/4}}{\pi} \cdot \frac{\mathbf{p}}{(\mathbf{p}^2 + 2U_i)^3} \tag{1.66}$$
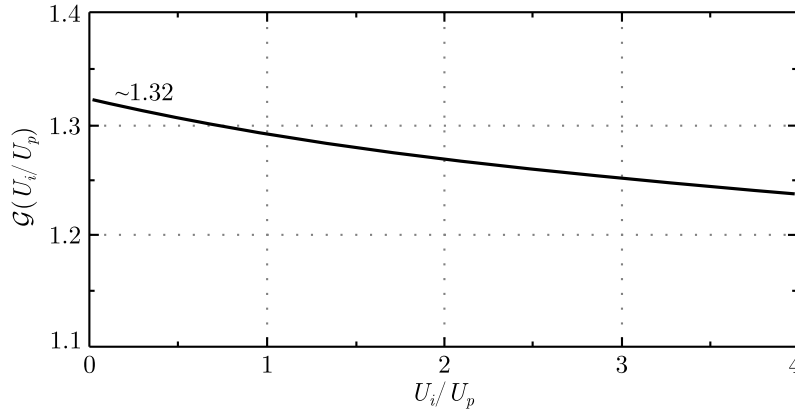
Figure 1.5: Plot of the correction function $\mathcal{G}(U_i/U_p)$ for the cut-off law in the quantum-mechanical model, from [39]. For $U_i \ll U_p$ ($\gamma \ll 1$, tunnel regime) this function is ~ 1.32.

The quantum-mechanical model also yields the classical cut-off law equation, Eq. (1.57) up to a small correction. By Fourier transforming the dipole moment, the cut-off frequency is found to be:

$$\hbar \omega_H \simeq 3.17 U_p + \mathcal{G} \left(\frac{U_i}{U_p} \right) U_i \tag{1.67}$$

where $\mathcal{G}(U_i/U_p)$, shown in Fig. 1.5 is a slowly varying function of the order of 1. This correction is related to the tunneling effect: since the electron must tunnel out, it cannot appear at the origin $x = 0$ and, when returning to the position x_1 where it appeared, it can acquire an additional kinetic energy approximatively equal to the work of the electric field in the interval $[x_1, 0]$. The spreading of the wavefunction then tends to average and decrease this additional kinetic energy gain for larger U_i.
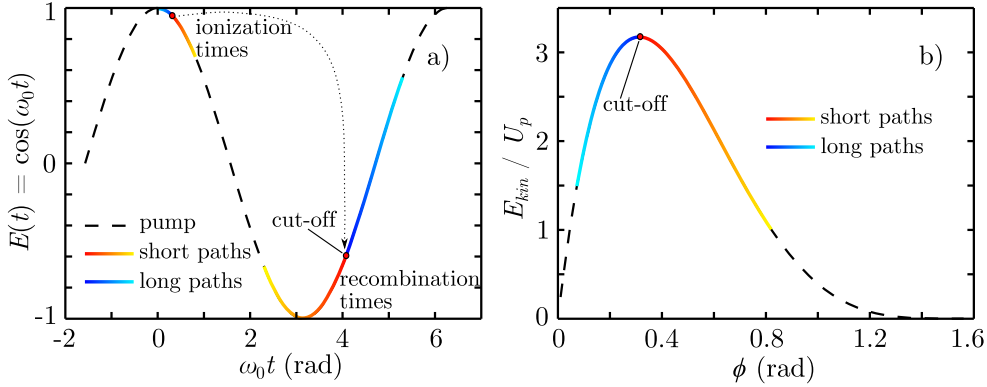
Figure 1.6: a) From the classical three-step model: times at which the electron appears in the continuum (ionization) and recombination times, superimposed to the amplitude (normalized) of the electric field. The red circle correspond to the trajectory which achieves the maximum kinetic energy. Red-yellow lines correspond to short trajectories; blue-cyan lines to long trajectories. b) Kinetic energy for the classical model as a function of the initial field phase [equivalent to the ionization time of figure a), in units $\omega_0 t$]. The red-yellow line correspond to the kinetic energy for the short trajectories; blue-cyan line to the kinetic energy for the long trajectories. The red circle is the cut-off energy.

Different electron trajectories in the integral of the dipole equation, Eq. (1.60), acquire different phases during the time they spend in the continuum. These phase shifts are usually referred to as *atomic dipole phases*. Upon recombination, the final electronic wavepacket will be featured by the interference between these different quantum paths. In particular, referring to the classical three-step model, for a given final kinetic energy value in the plateau region (thus below the cut-off energy) there exist two different initial field phase values, corresponding to two different electron trajectories, see Fig. 1.6(b). Therefore, for a particular harmonic frequency there exist two main electron trajectories. Figure 1.6(a) shows the time at which the electron appears in the continuum (ionization time) and the time at which it recombines to the atom: the time corresponding to the cut-off energy (absolute phase $\simeq 18°$) divides the quantum trajectories into two families: one in which the electron appears into the continuum *after* the absolute phase $\phi \simeq 18°$

and recombines *before* the recombination time corresponding to the cut-off energy [red-yellow lines in Fig. 1.6(a)], and one in which the electron appears *before* the phase corresponding to the cut-off and recombines *after* the recombining time of the cut-off trajectory [blue-cyan lines in Fig. 1.6(a)]. One family is therefore characterized by return times shorter than approximately half a period of the laser field, while the other one presents return times close to a full period [42].
The quantum trajectories are thus divided into *short* and *long trajectories* (or quantum paths) depending on whether they belong to the first or the second family, respectively.

Such trajectories will interfere constructively or destructively, depending on their relative dipole phase. This dipole phase depends on the electric field. It has been shown [42–44] that the dipole phase is linearly proportional to the laser intensity I, with different coefficients for short and long paths, in atomic units: $\varphi_{at}^{(s,l)} \simeq -\tau^{(s,l)} U_p$, where φ_{at} is the atomic dipole phase for short $\varphi_{at}^{(s)}$ and long $\varphi_{at}^{(l)}$ trajectories, with return times $\tau^{(s)} \simeq 0$ and $\tau^{(l)} \simeq 2\pi/\omega_0$, respectively. Since U_p is proportional to the laser intensity, the dipole phase may be rewritten (in International System units) as:

$$\varphi_{at}^{(s,l)} \simeq -\alpha^{(s,l)} I \tag{1.68}$$

For example, for the 15th harmonic in argon, these coefficients are of the order $\alpha^{(s)} \simeq 10^{-14}$ cm^2/W and $\alpha^{(l)} \simeq 27 \times 10^{-14}$ cm^2/W.

This intensity-dependent nonlinear phase gives rise to modifications of the spectral line shape of high harmonics [45, 46] and it originates an almost linear chirp in the harmonic field [43, 47]. Moreover, it introduces a curvature of phase fronts, originating different divergence properties [45, 48, 49].

1.6.3   Phase matching

An important effect to be considered in the process of HHG is how the harmonic field generated sums up coherently during *propagation* along ζ [50].
The harmonic field at each propagation distance may be understood as a light source with a phase closely related to the pump phase, which sums with the previously generated field; the resulting field intensity will then grow if the phase fronts of the newly generated field match with the propagating field, i.e. they interfere constructively.
In general, there will be an effective distance over which the interference is constructive. This distance is called *coherence length* and it is tightly related to the

phase mismatch $\Delta \mathbf{k}$ between the source and the harmonic field:

$$L_c = \frac{\pi}{|\Delta \mathbf{k}|} \tag{1.69}$$

it represents the distance over which the relative phase between the harmonic field and its source change by π rad.

The phase mismatch, which depends on the harmonic frequency under consideration, may be decomposed into a series of different contributions:

$$\Delta \mathbf{k} = \Delta \mathbf{k}_{disp} + \Delta \mathbf{k}_{plasma} + \Delta \mathbf{k}_{geom} + \Delta \mathbf{k}_{atomic} \tag{1.70}$$

namely dispersion, plasma effect, geometrical factor, atomic dipole phase.

The dispersion term comes from the frequency-dependent refractive index $n(\omega)$. For the generation of the qth-harmonic, the dispersion contribution (for simplicity of notation in scalar form) reads:

$$\Delta k_{disp} = k(\omega_q) - q k(\omega_0) = q \frac{\omega_0}{c} \left(n(\omega_q) - n_0 \right) \tag{1.71}$$

where $k(\omega_q)$ is the wavevector at the harmonic frequency. This term depends only on the difference between the refractive index values at the pump and harmonic frequency. In general, the refractive index is larger than 1 for frequencies in the visible and near-infrared range, while it is smaller than 1 in the XUV, i.e. in the typical range of high order harmonics. The dispersion term is thus usually *negative*.

The Δk_{plasma} term comes from the effect of the free electron plasma generated during the ionization of the medium, see section 1.5.6. Indeed, only a very small part of electrons actually recombine to emit a harmonic photon.
The plasma locally modifies the refractive index, as shown in Eq. (1.42). In particular, in HHG experiments plasma densities are usually much smaller than the critical density ρ_c of the infrared laser radiation ($\lambda_0 = 800$ nm); moreover, for high harmonics the correction term is even smaller since the critical density is higher (for example, for the 10th harmonic this quantity is 100 times the critical density at the fundamental frequency). The plasma term thus read:

$$\Delta k_{plasma} = k_{plasma}(\omega_q) - q k_{plasma}(\omega_0) \simeq \frac{\omega_0 \rho}{2 c \rho_c} \left(q - \frac{1}{q} \right) \simeq \frac{q \omega_0 \rho}{2 c \rho_c} \tag{1.72}$$

where in this case ρ_c is the critical plasma density at frequency ω_0 (we considered $n \simeq 1$ for both the pump and the harmonic field in the evaluation). This term is then usually *positive*.

The geometric term arises from the spatial properties of the beam involved in the HHG process. In particular, this term represents the phase difference with

respect to a plane wave. Similarly to the concept of instantaneous frequency, the local wavevector is defined as the spatial gradient of the phase $\varphi(x, y, \zeta)$ of the beam:

$$\mathbf{k}_{inst} = \nabla\varphi(x, y, \zeta) \qquad (1.73)$$

For a Gaussian beam geometry, on axis ($r = 0$), the beam exhibits an additional longitudinal phase shift called *Gouy phase shift*:

$$\varphi_{Gouy} = \arctan\left(\frac{\zeta}{L_{DIFF}}\right) \qquad (1.74)$$

where L_{DIFF} is the Rayleigh range of the Gaussian beam, with beam waist (or position of the focus) at $\zeta = 0$. In particular, the Gouy phase shift is responsible for an additional π phase change in the propagation through the focus (beam waist position). The local wavevector on axis is then positive with a maximum at the beam waist position:

$$k_{inst} = \frac{1}{L_{DIFF}} \cdot \frac{1}{1 + (\zeta/L_{DIFF})^2} \qquad (1.75)$$

This thus gives a *negative contribution* in the phase mismatch term.

In the case of a guided geometry [51–54], the pump beam is focused on and propagates inside a capillary filled with gas. Because of the dispersion property of the modes inside the waveguide [55], for the fundamental mode the longitudinal wavevector is:

$$k_{capillary}(\omega) \simeq \frac{\omega}{c} - \frac{(2.4048)^2 c}{2a_0^2 \omega} \qquad (1.76)$$

with 2.4048 the first zero of the Bessel function J_0, c the speed of light in vacuum and a_0 the capillary inner radius. This expression has been derived by assuming that the refractive index inside the hollow waveguide is 1 and $\omega a_0/c \gg 2.4048 n_{cap}$, with n_{cap} the refractive index of the medium constituting the capillary itself, i.e. the capillary is much larger than the wavelength of light. In particular, the wavevector may be written as $k_{capillary} = \omega\cos\theta_{eff}/c$, where $\theta_{eff} \ll 1$ is an effective propagation angle which in general depends on the frequency. Since the effective longitudinal wavevector is shortened by this effect, the geometrical term in this case is *positive*.

A similar geometrical term is experienced in the case of self-guided geometry [56, 57] or Bessel beams [58–61].

The atomic dipole term, as shown in the previous section, arises from the quantum ionization-propagation-recombination process. In particular, since the phase contribution from the quantum process depends on the intensity, the local

wavevector will be proportional to the gradient of the intensity. In particular, the longitudinal component of the wavevector will be:

$$k_{atomic}^{(\zeta)} = -\alpha^{(s,l)}\partial_\zeta I \tag{1.77}$$

where the (positive) coefficient $\alpha^{(s,l)}$ depends on the particular quantum trajectory (short or long) under consideration. The atomic dipole phase mismatch term thus has the same sign as that of the intensity gradient. In general, for a given intensity gradient, the absolute value of the long path wavevector contribution will be larger than the corresponding short path.

Because of the different values this coefficient assumes for the different quantum paths, it is possible to enhance one trajectory contribution with respect to the other by properly placing the medium (gas jet) before or after the focus of a Gaussian beam pump [46]. This affects not only the spectral profile, but also the spatial distribution of harmonic intensity.

1.6.4   Absorption

Beside the phase mismatch, a further factor limiting the yield of high harmonic frequencies is reabsorption in the medium itself. The high-harmonic photon frequencies are indeed typically in the XUV or soft X-ray spectral region, where light is well absorbed by matter. The absorption length L_{abs} may be defined as the distance over which the intensity of light (at a given frequency) drops by a factor $1/e$.

During propagation, the pump laser pulse continuously generates harmonic light which adds to the previously generated harmonic radiation. The latter is however attenuated by absorption of the medium. Even in the perfect phase-matching case ($L_c \to +\infty$), the total amount of harmonic field is thus limited by absorption and the total harmonic yield does not build up indefinitely for infinite interaction length, as shown in Fig. 1.7. In the case of this upper limit in harmonic generation the process is called *absorption-limited* HHG [62, 63].

Another effect which limits the harmonic generation occurs when the medium reaches the condition of full ionization, because HHG relies on the availability of non-ionized (bounded) electrons. Since the process involves high intensities, the requirements of both low plasma density and high intensity may be achieved with the use of very short driving pulses, so that the medium does not have enough time to become fully ionized.
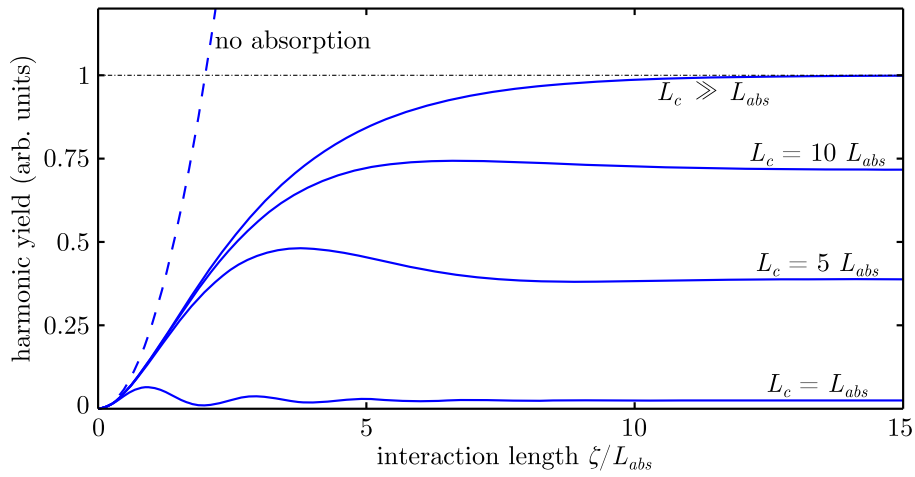
Figure 1.7: Effect of absorption in HHG, from [62], when the driving pulse intensity is supposed not to change during propagation. In the case of perfect phase matching ($L_c \to +\infty$) the harmonic yield grows quadratically over interaction distance if $L_{abs} = 0$. For finite absorption length, there is a limit asymptotic value, which depends on the coherence length (it decreases for smaller coherence lengths).

Chapter 2

Conical waves and filamentation regime

In this chapter we will introduce a family of space-time coupled non-Gaussian pulses which are (weakly) localized spatial stationary solutions of the linear propagation equation in cylindrical geometry, the conical wavepackets. In particular, we will describe the main features of these space-time coupled wavepackets, such as the possibility of independently tuning phase velocity and envelope velocity, i.e. the velocity at which phase and envelope fronts propagate on axis. These wavepackets and their distinguishing features will be at the basis of the numerical works described in this thesis.

We will also discuss the possibility of finite-energy experimental realizations of such wavepackets, and we will devote the final sections to the description of the filamentation regime, a dynamical regime in the evolution of ultrashort laser pulses in which a particular kind of spatio-temporal stationary conical wavepackets, X-waves, have been observed to be spontaneously generated. This regime will be a further topic of this thesis work.

2.1 Propagation equation

The starting point for the derivation of the nearfield and spectral features of conical wavepackets is the wave equation Eq. (1.7) for a complex scalar wavepacket $\mathcal{E}$ propagating in a dispersive medium in the linear case $\mathcal{J}, \mathcal{P} = 0$, when the wavepacket is assumed to be symmetric for rotations around the propagation axis (cylindrical symmetry).

We assume to describe such a wavepacket by a complex envelope $\Psi(r, \tau = t - z/v, z)$ (where r is the transverse radial coordinate) propagating in the forward direction at velocity v, possibly different from $v_g = 1/k_0'$, and a carrier wave

$\exp(i\beta z - i\omega_0 t)$ where the carrier wavevector β may differ from k_0; τ denotes the local time in this envelope reference frame.

The propagation equation governing this complex envelope in the temporal Fourier domain reads as

$$\left[\partial_{zz}^2 + 2i \left(\beta + \frac{\Omega}{v} \right) \partial_z + \nabla_\perp^2 + k_\perp^2(\Omega) \right] \hat{\Psi}(r, \Omega, z) = 0 \qquad (2.1)$$

where

$$k_\perp^2(\Omega) = k^2(\omega) - (\beta + \Omega/v)^2 \qquad (2.2)$$

and $\Omega \equiv \omega - \omega_0$ denotes the frequency departure from the carrier frequency. The longitudinal wavevector β is thus linked to the angular aperture θ_0 of the beam at the carrier frequency ω_0 as $\beta = k_0 \cos\theta_0$.

The general solution to Eq. (2.1) propagating in the forward direction with revolution symmetry reads as

$$\Psi = \frac{1}{2\pi} \int_{-\infty}^{+\infty} \mathrm{d}\Omega \int_0^{+\infty} \mathrm{d}K \, K \, \tilde{\Psi}(K, \Omega) \, J_0(Kr) \times \exp(i\kappa z - i\Omega\tau) \qquad (2.3)$$

where K represents the transverse component of the wavevector, $\tilde{\Psi}(K, \Omega)$ denotes an arbitrary function which represents the complex angular spectrum of the wavepacket at $z = 0$ and the longitudinal wavenumber associated with the envelope reads

$$\kappa = \sqrt{k^2(\omega) - K^2} - \left(\beta + \frac{\Omega}{v} \right). \qquad (2.4)$$

Conical wavepackets (CWPs) correspond to the specific choices of the angular spectrum:

$$\tilde{\Psi}(K, \Omega) = \hat{f}(\Omega) \cdot \delta \left[K - k(\omega) \sin\theta(\Omega) \right] \qquad (2.5)$$

where $\hat{f}(\Omega)$ is a weight function.

The simplest example of CWP is the *monochromatic Bessel beam* [64].

2.2   Monochromatic Bessel Beam

In the monochromatic case $\hat{f}(\Omega) = \delta(\Omega)$.

The general solution, Eq. (2.3), under the conical wave transverse wavevector relation, Eq. (2.5), and the monochromatic relation, reduces to

$$\Psi(r, z) = \sqrt{I_0} J_0(r k_0 \sin\theta_0)$$

where $J_0(x)$ is the 0th-order Bessel function of the first kind and I_0 represents the intensity of the wavepacket.

This solution has thus an amplitude which does not depend upon the propagation distance z. In other words, it is a stationary solution of the propagation equation, and its spatial profile overcomes the natural diffraction of the localized intensity peak, as first experimentally demonstrated in 1987 by Durnin, Miceli, Eberly [65].

By using the integral form of the Bessel function we obtain:

$$\mathcal{E}(z,r,t) = \sqrt{I_0} J_0(rk_0 \sin\theta_0) \exp\left(izk_0 \cos\theta_0 - i\omega_0 t\right) =$$
$$= \frac{\sqrt{I_0}}{2\pi} \int_0^{2\pi} d\phi \exp\left\{i\left[zk_0 \cos\theta_0 + r(\cos\varphi)k_0 \sin\theta_0 \cos\phi +\right.\right.$$
$$\left.\left.+r(\sin\varphi)k_0 \sin\theta_0 \sin\phi - \omega_0 t\right]\right\} =$$
$$= \frac{\sqrt{I_0}}{2\pi} \int_0^{2\pi} d\phi \exp\left\{i(\mathbf{q}\cdot\mathbf{r} - \omega_0 t)\right\}$$

where $\mathbf{r} = (x,y,z) = (r\cos\varphi, r\sin\varphi, z)$ represents the position vector, and the wavevector $\mathbf{q} = (k_0 \sin\theta_0 \cos\phi, k_0 \sin\theta_0 \sin\phi, k_0 \cos\theta_0)$ intersects the z axis at an angle θ_0. The Bessel beam may thus be viewed as a continuous superposition of plane waves with wavevectors $\mathbf{q}$ of modulus k_0 and arranged along a conical surface, hence the name conical wavepacket.

The Bessel beam exhibits a central high intensity core and oscillating tails which decay to 0 as $r \to +\infty$. However, the ideal non-diffracting Bessel beam contains *infinite energy*, since the decay of the Bessel tail ($|\mathcal{E}|^2 \sim r^{-1}$) is not fast enough. In order to overcome this problem for practical realizations, it is possible to apodize the Bessel profile with a proper rapidly decaying function, as in the case of the Bessel-Gauss Beams [66]. The wavepacket is thus no more stationary in the strict sense, but for a finite propagation distance, called *Bessel zone* [67], the profile may be effectively described as an ideal Bessel beam, i.e. it exhibits a central narrow interference peak surrounded by a series of concentric lower intensity rings, which propagates without diffraction. Usually this non-diffracting propagation is much larger than the typical diffraction length associated to a Gaussian Beam with the same width as that of the central Bessel lobe [65].

Since the Bessel beam may be considered as a superposition of plane waves propagating on a cone, it exhibits a *self-reconstruction* (or self-healing) property [64, 68, 69]: the central core of the beam is reconstructed in propagation after it is blocked by an obstacle. This is explained by the fact that its constituents are propagating from a lateral direction, so that after a "shadow" zone they superimpose again and the Bessel profile is reconstructed. This property is appealing for applications such as particle trapping [70] and microscopy [71].

The phase velocity for the Bessel beam is $v_p = c/(n_0 \cos\theta_0)$. In vacuum (or for sufficiently high propagation angles) this velocity is larger than c; this is simply

due to the geometrical effect because of the plane waves constituents propagating at an angle with respect to the z axis.

The farfield (spectral) distribution of the Bessel beam is a ring of infinitesimal thickness and radius given by the cone angle θ_0. In the general case of apodized beams, the spectral distribution is the convolution of the infinitely narrow (delta) ring with the spatial Fourier transform of the apodizing distribution, i.e. it is an annulus of width inversely proportional to the apodizing function width.

2.3 Polychromatic CWPs

By looking back at Eq. (2.3), CWPs in general may be viewed as a superposition of monochromatic Bessel beams, i.e. a continuous superposition of plane waves with frequency-dependent wavevectors $k(\omega)$ distributed over cones of, in general, frequency-dependent angle $\theta(\Omega)$ with respect to the propagation direction z [72, 73].
The first polychromatic conical waves as superpositions of Bessel beams at different frequencies were derived in the field of acoustics by Lu and Greenleaf [74, 75]. Ref. [76] extended their solution to the field of electromagnetism.

Similarly to the Bessel beam case, CWPs present a central intense core and weakly decaying tails for $r \rightarrow +\infty$, and contain infinite energy, but practical realizations approaching ideal CWPs can be produced by finite energy beams sent through finite apertures. This finite-energy realizations effectively behave like the ideal infinite-energy solutions over a propagation region (Bessel zone) which depends on the spatial apodization of the profile. Moreover, they also exhibit the self-healing property of monochromatic Bessel beams.

Since CWPs are the polychromatic counterpart of Bessel beams, they exhibit not only a narrow peak in space, but also a temporal peak, depending on the temporal-frequency spectral distribution. However, CWPs are not in general stationary solutions of the propagation equation, because of their temporal (longitudinal) behavior.
The specific angle-wavelength (or analogously wavevector-frequency) relation $\theta(\Omega)$ determines the characteristics of the CWP, such as phase and envelope velocities, or effective dispersion [72].

2.3.1 Pulsed Bessel beams and Bessel X-pulses

Two representatives of the CWP family are the *pulsed Bessel beam* (PBB) and the *Bessel X-pulse* (BXP). By assuming a description as a superposition of plane-wave constituents, these particular wavepackets have the following characteristic features:

- *PBB* [77]: constant transverse component of the wavevector for each frequency, $K(\Omega) = K_0$. This corresponds to a frequency-dependent propagation angle $\theta(\Omega) = \arcsin[K_0/k(\omega)]$;

- *BXP* [78]: constant propagation angle for each frequency, $\theta(\Omega) = \theta_0$, and corresponding wavevector $K(\Omega) = k(\omega)\sin\theta_0$.

The PBB is generated by means of a circular diffraction grating and may be regarded as the product of a Bessel beam (in space) and a Gaussian pulse (in time). The BXP is similar to the pulse generated by sending a Gaussian beam through an axicon (i.e. a conically shaped lens) and exhibits a two-winged (X-shaped) structure resulting from the superposition of an inward and an outward beam [72, 79, 80].

PBBs and BXPs are particular cases of the axisymmetric counterparts of *tilted pulses*. Tilted pulses are pulses in which the pulse envelope (amplitude) fronts are inclined (tilted) with respect to the propagation direction of the beam [81]: therefore, amplitude fronts and phase fronts are not parallel to each other [82, 83]. In general, as a first order approximation, every CWP may be represented by one of this rotationally symmetric wavepackets.
As schematically represented in Fig. 2.1, it is possible to independently tune phase (v_p) and envelope (v) velocities of the main intensity peak of a rotationally symmetric tilted pulse, and therefore, in general, of a CWP by properly adjusting the propagation angle and angular dispersion. In particular, these velocities read [72]

$$\begin{cases} v_p = \dfrac{\omega_0}{k_0 \cos\theta_0} & (2.6) \\[2ex] v = \dfrac{\cos\delta}{k_0' \cos(\theta_0 + \delta)} & (2.7) \end{cases}$$

with $\theta_0 = \theta(\omega = \omega_0)$ the mean cone angle, and $\delta = \arctan(\theta_0' k_0/k_0')$ the mean tilt angle of the amplitude fronts ($\theta_0' = \partial_\omega\theta|_{\omega=\omega_0}$). The phase velocity is then equal to phase velocity of the corresponding monochromatic Bessel beam. The phase and the envelope velocities refer to the main intensity peak of the pulse; in particular, v should not be confused with the group velocity at which each amplitude front propagates. By properly adjusting the propagation and the tilt angles the envelope velocity may become larger than c [84] or even negative [85]
Within this framework, the PBB case corresponds to $\delta = -\theta_0$, while the BXP case to $\delta = 0$. In the PBB case the envelope velocity is $v = v_g \cos\theta_0$, while in the BXP case this velocity is $v = v_g/\cos\theta_0$, where $v_g = 1/k_0'$.
The phase velocity in the PBB case is larger than the envelope velocity, while, in the case of negligible dispersion ($n \simeq n_0$), for the BXP case we have $v \simeq v_p$.
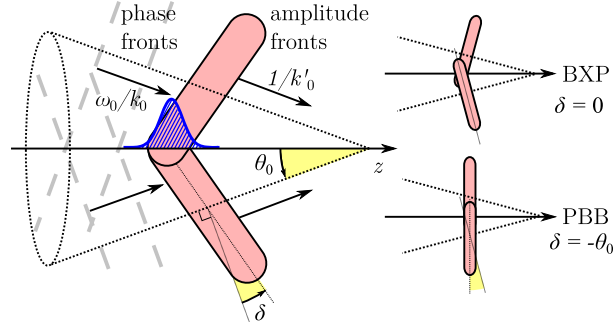
Figure 2.1: Schematic propagation of a CWP: the gray dashed lines represent phase fronts and the red areas amplitude fronts. θ_0 and δ are the propagation and tilt angles, respectively. The quantities v_p and v refer to the main intensity peak of the pulse, represented in the figure by the blue Gaussian profile. On the right there is a schematic representation of the PBB and BXP cases.

The velocity at which the energy of the pulse propagates along the z axis is $v_g \cos \theta_0$. For small angles this velocity is roughly v_g.

2.3.2 Stationary CWPs

The specific frequency-angle relation of CWPs introduce an additional dispersive effect, given by the angular chromatic dispersion (which characterizes also tilted pulses). This effective group velocity dispersion reads:

$$k''_{eff} = \left(k''_0 - k_0(\theta'_0)^2\right) \cos \theta_0 - (k_0\theta''_0 + 2k'_0\theta'_0) \sin \theta_0 \qquad (2.8)$$

In the BXP case, for example, this becomes $k''_{(BXP)} = k''_0 \cos \theta_0$, so that BXPs propagating in vacuum do not undergo effective chromatic dispersion, since $k''_0 = 0$. In the PBB case, however, this effective dispersion reads

$$k''_{(PBB)} = \frac{k_0 k''_0 - \sin^2 \theta_0 \left((k'_0)^2 + k_0 k''_0\right)}{k_0 \cos^3 \theta_0}$$

so that it becomes $k''_{(PBB)} = -\tan^2 \theta_0/(\omega_0 c \cos \theta_0)$ in vacuum ($k''_0 = 0$ and $k'_0 = 1/c$). In particular, this means that PBBs, and CWPs in general, exhibit chromatic dispersion even when propagating in a non-dispersive medium, due only to the relation between propagation angles and frequencies.

By properly tuning the spectral feature of a CWP, however, it is possible to use this effective dispersion to compensate for the dispersion of the medium.
The resulting CWP will then be a stationary wavepacket in the full (r, τ) space, i.e. its spatio-temporal intensity distribution will not depend on the propagation distance z.

This behavior is obtained when the longitudinal component of the wavevector varies linearly with frequency: $k_z(\Omega) = k_0 \cos\theta_0 + \Omega/v$. In this case the envelope of the wavepacket is stationary in the reference frame moving at velocity v. This corresponds to the spectral constraint: $\tilde{\Psi}(K,\Omega) = \hat{f}(\Omega) \cdot \delta[K - k_\perp(\Omega)]$, with $k_\perp(\Omega)$ given by Eq. (2.2).

Such stationary CWPs have been obtained by Porras and Di Trapani [86] and Longhi [87] in the context of the paraxial envelope propagation equation in the linear case [Eq. (1.27) with $N = 0$] and more recently studied in a non-paraxial framework by Malaguti and Trillo [88].

Under the angular spectrum choice $\tilde{\Psi}(K,\Omega) = \hat{f}(\Omega) \cdot \delta[K - k_\perp(\Omega)]$, the envelope reads:

$$\Psi(r,\tau) = \int_{k_\perp(\Omega)\in\mathbb{R}} \hat{f}(\Omega) J_0[k_\perp(\Omega)r]\exp(-i\Omega\tau)\mathrm{d}\Omega \qquad (2.9)$$

where integration is performed over frequencies for which $k_\perp(\Omega)$ is real, so that these wavepackets can be viewed as a continuous superposition of monochromatic Bessel beams following the specific angle-frequency spectral relation of Eq. (2.2).

After a small Ω-expansion of the dispersion relation up to second order, $k(\omega) \simeq k_0 + k_0'\Omega + k_0''\Omega^2/2$, we have

$$k_\perp^2(\Omega) = \alpha_2\Omega^2 + 2\alpha_1\Omega + \alpha_0, \qquad (2.10)$$

where $\alpha_2 = k_0 k_0'' + (k_0')^2 - 1/v^2$, $\alpha_1 = k_0 k_0' - \beta/v$ and $\alpha_0 = k_0^2 - \beta^2$.

Referring to the notation of Ref. [88], stationary CWPs are characterized by two parameters: the angular aperture θ_0, related to the longitudinal wavevector at the central frequency $\beta = k_0 \cos\theta_0$, and the velocity v of the CWP. Figure 2.2 shows the different types of stationary conical waves in the plane (θ_0, v) in the case of water at $\lambda_0 = 527$ nm ($k_0 = 15.924 \ \mu\mathrm{m}^{-1}$, $k_0'' = 0.056 \ \mathrm{fs}^2/\mu\mathrm{m}$, $v_g = 0.7366 \cdot c$). This classification is based on a second order approximation of medium dispersion, but spectral features remain qualitatively similar even if the full dispersion relation of the medium is retained, provided that the bandwidth is not too large. A single exception exists when the spectrum of the wavepacket is centered around a zero of the GVD.

Roughly speaking, depending on the sign of the coefficient k_0'' for second order GVD the spatio-temporal spectral shape given by Eq. (2.2) may be divided in two main families: *hyperbolic* and *elliptic profiles*. The former case refers to the normal GVD case ($k_0'' > 0$) and the corresponding CWPs are called *X-waves*; the latter case, called *O-wave* case, refers to negative (anomalous) GVD [72, 86, 87]. In correspondence to a central frequency close to a zero in the GVD, the spatio-temporal spectra present features common to both normal and anomalous GVD cases; this case is called "fish wave", since the corresponding spectral shape exhibits an elliptic core and an hyperbolic tail.
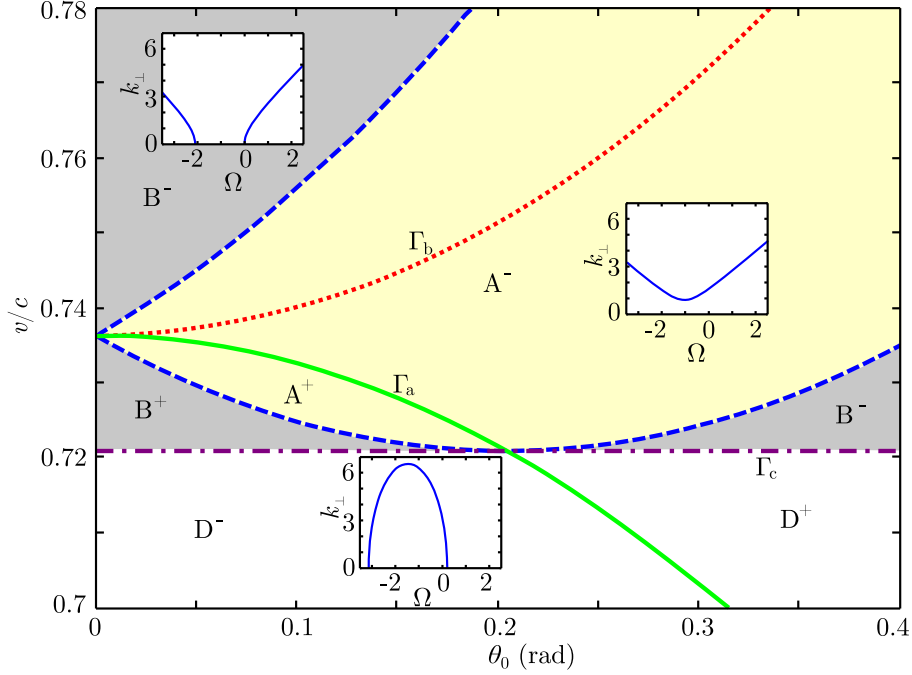
Figure 2.2: Parameter space (θ_0, v) for stationary CWPs in water and at a central wavelength of 527 nm. The different sectors labeled A,B,D are bounded by the dashed curves given by $\alpha_1^2 = \alpha_2\alpha_0$, and line Γ_c ($\alpha_2 = 0$), on which the shape of the angular spectrum $k_\perp(\Omega)$ changes. A: X-waves (hyperbolic) with angle gap. B: X-waves (hyperbolic) with frequency gap. D: O-waves (elliptic). The $\pm$ labels indicate that the central frequency of the $k_\perp(\Omega)$ curve is upshifted (+) or downshifted (−) with respect to ω_0. The curves Γ_a ($v = v_g \cos\theta_0$) and Γ_b ($v = v_g/\cos\theta_0$) determine loci around which stationary CWPs with sufficiently narrow bandwidth share the features of PBBs or BXPs, respectively. The insets show the qualitative shape of the dispersion curve Eq. (2.10) for the cases B⁻, A⁻, D⁻($k_\perp$ in μm^{-1}, Ω in rad/fs).

The authors of Ref. [88] found elliptic solutions also in the normal GVD case, when v is very different from v_g; this is due to the negative sign of the effective GVD coefficient. In Fig. 2.2, the line Γ_c is defined by $\alpha_2 = 0$. The region above this line corresponds to X-wave solutions ($\alpha_2 > 0$), i.e. hyperbolic shaped solutions. In particular, regions A$^\pm$ ($\alpha_1^2 - \alpha_2\alpha_0 < 0$) correspond to hyperbolic solutions of Eq. (2.10) with wavevector (angle) gap, while regions B$^\pm$ ($\alpha_1^2 - \alpha_2\alpha_0 > 0$, shaded areas) correspond to hyperbolic solutions with frequency (wavelength) gap. The insets show the typical spectral profiles corresponding to such wavepackets.

The region below line Γ_c corresponds to O-wave like solutions ($\alpha_2 < 0$), which present elliptic $k_\perp(\Omega)$ profiles and are analogous to the solutions found in the case

of anomalous GVD.

The curves Γ_a and Γ_b determine loci around which stationary CWPs with sufficiently narrow bandwidth share the features of PBBs or BXPs, i.e. envelope velocity $v = v_g \cos \theta_0$ and $v = v_g / \cos \theta_0$, respectively. In particular, along line Γ_a, the spectral $k_\perp(\Omega)$ curves are symmetrical with respect to the central frequency ω_0 ($\Omega = 0$).

2.4   Experimental realization

As already said, ideal CWPs carry infinite energy due to their weakly decaying tails. Any experimental realization would necessarily imply the use of their apodized, finite-energy counterparts, which effectively approach the ideal wavepackets only over a limited propagation distance called Bessel zone.

Usually in experimental realizations CWPs are generated by sending an input Gaussian beam over a series of optical elements. In particular, one of the most efficient method to generate Bessel-like pulses is the use of a refractive conical lens: the *axicon* [89, 90].

The propagation angle at frequency ω for a beam impinging on an axicon made of a material with refractive index $n_{ax}(\omega)$, with cone base angle α_{ax} is:

$$\theta(\omega) = \arcsin\left(\frac{n_{ax}(\omega)}{n(\omega)} \sin \alpha_{ax} \right) - \alpha_{ax} \qquad (2.11)$$

where $n(\omega)$ is the frequency-dependent refractive index of the medium surrounding the axicon. In general, if both the chromatic dispersions of the axicon and the surrounding medium may be neglected, this angle [Eq. (2.11)] is approximatively constant for each frequency, so that the pulse may be effectively treated as a BXP. If the BXP-like pulse is generated in a weakly dispersive medium (as a gas $n(\omega) \sim 1$), then the main departure from the ideal spectral features of the BXP will be due to the axicon medium dispersion.

Another similar method for generating BXP-like pulses is the use of an amplitude mask in the form of an annular aperture [65, 78]. The light passing the ring is then focused by a converging lens, so that in the focal plane of the lens the spatial Fourier transform of the ring structure (a Bessel beam) is generated. In this case the departure from the ideal BXP is mainly due to the dispersion of the lens.

CWPs may also be generated by means of diffractive axicons, that is by cylindrical transmission gratings [91–93]. In this case the envelope fronts will be parallel to the grating itself, while the phase fronts (for wavelength λ) will be bent at angle $\theta(\lambda)$ satisfying (first diffraction order):

$$\sin \theta(\lambda) = \frac{\lambda}{n(\lambda)d} \qquad (2.12)$$

where d is the grating period. The transverse wavevector will then be:

$$K(\lambda) = \frac{2\pi n(\lambda)}{\lambda} \sin \theta(\lambda) = \frac{2\pi}{d} \qquad (2.13)$$

The resulting profile is thus a PBB.

Another possible method for generating a PBB is the use of a hollow core fiber. The propagation modes inside a capillary are indeed PBBs with sharp edges [55]. On exiting the capillary, the wavepacket will be a highly apodized PBB: for the fundamental mode, for example, in the case in which the capillary is much larger than the wavelength of light, the spatial function will roughly be nil outside the first Bessel zero.

In general both axicon and holographic methods do not allow for very high energy beam in order not to damage the optical elements. Moreover, in the holographic case a significant part of the input energy is lost in the other diffraction order. To overcome these limitations it is possible to employ different (more complicated) geometries and reflective axicons.

A recent study [94] has shown the possibility of generating and amplifying a PBB by mean of a $\chi^{(2)}$ (second-order nonlinearity) parametric amplification by exploiting the phase-matching curves of the nonlinear crystal.

Apodized versions of stationary CWPs have been shown to spontaneously appear during the filamentation of ultrashort laser pulses [95–99]. The instantaneous refractive index change from the high intensity filamentation regime may also be exploited to exert a spatio-temporal reshaping on a weak seed pulse [100]. In conjunction with other nonlinear processes, such as Raman resonances, this reshaping may also lead to amplification of the seed pulse [101].

2.5   Filamentation of femtosecond laser pulses

The phenomenon of *ultrashort laser pulse filamentation* in air was first reported by Braun *et al.* in 1995 [102] by launching intense infrared femtosecond laser pulses in the atmosphere. They observed a shrinking of the beam waist, which remained focused for a distance of over 20 m.

In condensed media short-range filamentation was a phenomenon known since the sixties [103–105]. However, the propagation was limited by the optical breakdown of the medium. The advent of ultrashort (femtosecond) laser pulses allowed long-range filamentation regime also in condensed media [106].

Filamentation, as defined in Ref. [15], is a *dynamic* optical pulse structure with an intense core that is able to propagate over extended distances much larger than the typical diffraction length (Rayleigh range) while keeping a narrow beam size without the help of any external guiding mechanism.

It is now well understood that this regime arises from a dynamic competition between self-focusing and a series of saturating or defocusing mechanisms. This involves a series of successive focusing-defocusing cycles that give the overall impression of a stationary-like propagation.

The main effect responsible for the filamentation regime is indeed the optical Kerr effect, see section 1.5.1, which leads to an intensity-dependent refractive index, thus inducing beam self-focusing. On the other hand peak-intensity reduction (thus preventing a catastrophic collapse) due to nonlinear absorption and temporal dispersion, and defocusing due to the free electron plasma, generated by the high intensities involved, counterbalance the focusing effect. During propagation, the filament will continuously lose energy until it dies out and a linear propagation regime is resumed.

2.6   Properties of light filaments

Although light filaments appear in a great variety of materials, they usually present a series of typical characteristics and related phenomena, common to all media, input pulse wavelengths and durations (within the ultrashort pulse regime), which are briefly summarized in the following sections.

2.6.1   Spatial robustness

The intensity peak associated to the filament is highly localized in space. Typical diameters are of the order of $\sim 100~\mu$m in air and $10 - 40~\mu$m in condensed media. This tightly localized peak is surrounded by a large background that acts as an energy reservoir continuously refilling the central core.

Such a feature is at the basis of the filament robustness to spatial perturbations, the *self-healing property*.

A filament spontaneously regenerates shortly after a stopper which blocks its central high intensity core [107–109]. The energy reservoir around the central spot manages to regenerate the core. Moreover, experiments in water (Fig. 2.3) have demonstrated that the clipping of this background reservoir brings a fast extinction of the central peak [110].

Experiments in air give the same results: filaments can survive interactions with droplets stopping the central core and their propagation proceeds substantially unperturbed even through clouds [111] and fog [112].
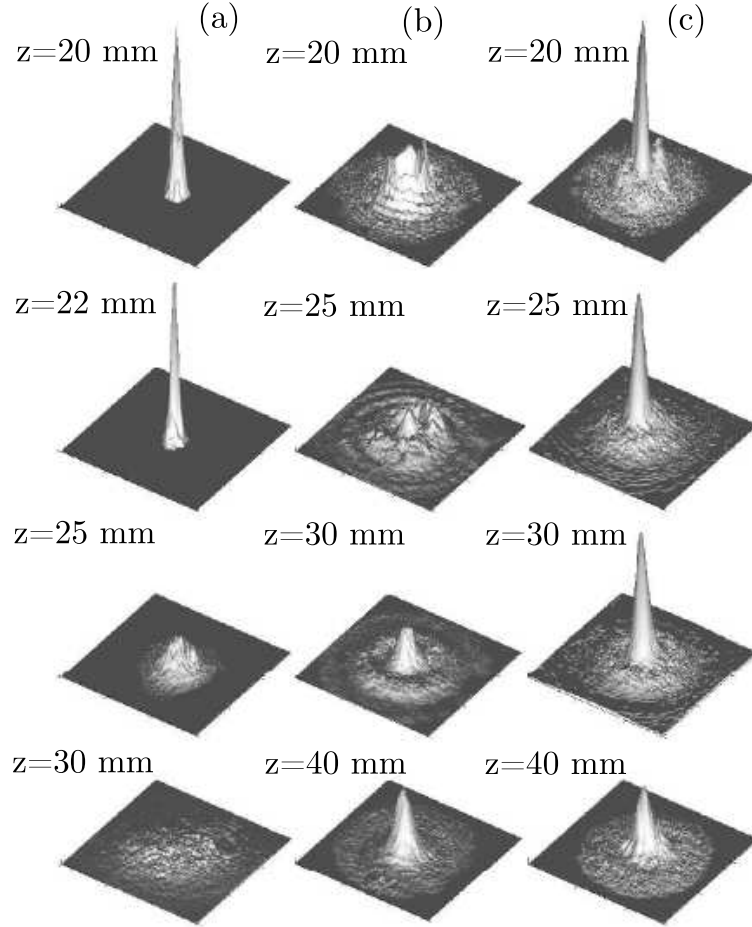
Figure 2.3: Fluence profiles in the cases of (a) clipped, (b) stopped and (c) free filaments in water (input peak power $\mathbb{P}_{in} = 13\mathbb{P}_{thr}$), from [110]. In the clipped case the central core quickly decreases, while just after the stopper the central peak is reconstructed until it is indistinguishable from the free case.

2.6.2   Spectral broadening and continuum generation

Filamentation is accompanied by a strong broadening of the initial spectrum of the pulse, called *super-continuum emission*. The physical mechanism for super-continuum emission largely follows the phenomena identified in fibers, see e.g. Ref. [113].

For example, a pulse centered in the near infrared (800 nm) generates during filamentation a coherent emission with a low angular divergence which covers the whole visible range. The continuum may span more than 1 octave. On the low frequency side, continuum generation has been observed up to 5 μm in infrared

[114]. This frequency conversion can involve an appreciable fraction of the initial energy.

The continuum of frequency generated by the filament may be subsequently compressed with a proper chirped mirror setup to obtain few-cycle optical pulses [115, 116] for highly nonlinear application, such as HHG. The filamentation thus constitutes an alternative to the use of self-phase modulation via propagation inside a gas-filled hollow capillary, with the advantage of being much less sensitive to experimental conditions such as beam alignment, input pulse duration or gas pressure.

Recent works [117, 118] have highlighted that the statistical properties of the extremes of the spectral super-continuum from the filamentation regime in a series of measurements affected by shot-to-shot fluctuations exhibit a long-tailed "L-shaped" distribution. This statistical distribution is associated to the physics of extreme events, or rogue waves [119]. In particular, these events may be described in terms of optical rogue waves [120, 121].

2.6.3   Conical emission (CE)

The white light beam generated during filamentation generally consists of a white central core surrounded by a structure of colored rings (Fig. 2.4).
The propagation angle increases with the frequency shift with respect to the central frequency of the pump pulse.

This phenomenon depicts a strong space-time coupling dynamics during the process of filamentation because every new generated frequency corresponds to a specific emission angle.

This mechanisms may be explained as the spontaneous evolution towards stationary X-waves profiles [96, 122], as discussed below.

2.6.4   Temporal splitting of the pulse

The filamentation process determines a strong reshaping of the pulse both from a spatial and a temporal point of view. In particular, during filamentation one or more temporal splittings of the initial pulse are observed.

Usually a first splitting is observed at the onset of the filament (nonlinear focus) and the two daughter pulses tend to separate from each other traveling at different peak velocities and are temporally much shorter than the input pulse. As an example, a 1 ps pump pulse filament in fused silica will split into two pulses with durations of the order of 10-20 fs.
If the pulse energy is high enough, the intensity in the central part may grow again due to Kerr self-focusing, leading to another subsequent splitting process. This process may be repeated several times provided that there is enough energy.
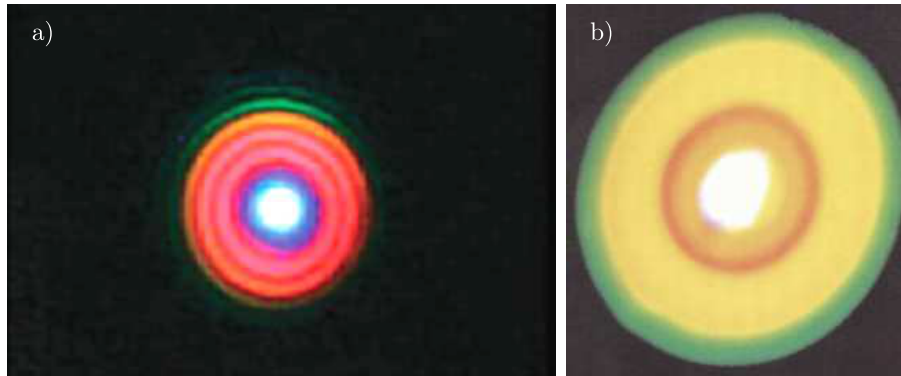
Figure 2.4: Images of conical emission in the case of filamentation. a) from [123]: after a propagation distance ~ 25 m; b) from [124]: at a distance of 30 m from the onset of filamentation. In the right figure, the diameter of the outer (green) ring ~ 10 cm.

Propagation effects such as absorption or defocusing and a consequent refocusing stage may lead to the isolation and survival of a single, temporally compressed, intense pulse [125, 126].

2.6.5 Intensity clamping

The peak intensity of the input pulse may increase by several orders of magnitude during the initial self-focusing stage, until it reaches an almost constant value in the filament regime, which depends on the material characteristics. In gaseous media, with peak intensities of the order of tens of TW/cm^2, the main limiting mechanisms for intensity clamping are plasma defocusing and nonlinear losses. In condensed media, with maximum intensities of the order of 1 TW/cm^2, the main limiting mechanisms are multiphoton absorption and GVD. In both gaseous and condensed media the filament will reach a maximum "clamped" intensity level due to these saturating mechanisms.

2.6.6 Pulse mode self-cleaning

It has been observed that the farfield profile of the conical emission originating from the filament exhibits an extremely high beam quality, while the remnant of the incident pulse, which does not couple into the filament, exhibits a poorer beam quality [127].

2.6.7 Plasma channel

The high intensities associated with the filamentation process generate a channel of free electrons due to multiphoton ionization. This narrow channel of plasma contributes to the arrest of the collapse and the consequent onset of the filamentation regime. The plasma channel is regarded as a central mechanism for a lot of applications, such as guiding of electrical discharges [128, 129], virtual antenna applications [130] and THz generation [131–133].

2.7 Models for filamentation

The first model proposed to explain the filamentation of long pulses was the *self-trapping model*, in which diffraction manages to balance the self-focusing of the beam. It has been demonstrated the existence of a particular profile ensuring a perfect balance between diffraction and self-focusing: the *Townes profile* [134], that is however unstable, both structurally and under perturbations in more than one dimension [135]. This led to the development of different models. The *moving focus model* was one of these early models.

2.7.1 Moving focus model

In the moving focus model [135, 136] the initial pulse is considered as a series of thin time slices which propagate independently from each other at the group velocity of the pulse. Every slice contains a specific power. Those with higher power will undergo Kerr self-focusing at shorter distances than the ones with lower power. The slices with power below $\mathbb{P}_{thr}$ will diffract. The filament will thus be the collection of the nonlinear foci corresponding to the different slices. In the case of a converging beam all the nonlinear foci lie before the linear focus. This is in contradiction with many experimental results with filaments extending much further than the linear focus. Therefore a possible correction to this model has been proposed with the consideration that delayed Kerr effect and plasma defocusing induce a strong coupling between the temporal slices of the pulse [137].

2.7.2 Self-guiding model

The *self-guiding model* [102, 124] is similar to the self-trapping model: it proposes a local balance between self-focusing on one side and diffraction and defocusing from the self-generated plasma on the other one. Self-focusing forms a leading peak which generates a channel of plasma; the trailing part of the pulse is then defocused while the leading peak suffers multiphoton absorption

and becomes less intense. This determines a lower production of plasma and self-focusing becomes stronger; if the power is high enough then other focusing-defocusing cycles may happen until the pulse power becomes insufficient for further focusing.

2.8   Conical X- and O-waves

The spontaneous formation of X-waves (described in section 2.3.2) in the presence of nonlinearity was first demonstrated in a second-order nonlinear crystal [122] and afterwards in Kerr media [95, 138, 139]. The concept of X-waves was then used to explain the properties of the propagation of laser pulse filaments in transparent media.

The interpretation is that, regardless the way of its formation, the evolution of the filament is governed by the interactions of one or more stationary non-diffractive and non-dispersive spatio-temporal profiles in the form of CWPs, so that the central high intensity core is the result of an interference effect, continuously refilled by the surrounding low-intensity energy reservoir. Kolesik *et al.* demonstrated by means of numerical simulations [95] that filamentation in condensed media may be interpreted as a dynamical interaction of these spontaneously-formed nonlinear X-waves.

Linear X-waves are not stationary solutions in the presence of nonlinear terms such as Kerr effect, nonlinear losses or plasma action. However, (apodized) conical solutions may be regarded as stationary solutions both in the linear and in the nonlinear case. Starting from the envelope equation Eq. (1.27), it is possible to determine the form of the stationary profiles by means of numerical integrations even in the presence of nonlinear terms such as the Kerr effect and multiphoton absorption (nonlinear losses); stationary profiles for nonlinear X-waves supporting plasma generation have not yet been found. If one or more terms in this equation may be neglected, stationary modes assume the following forms:

- Monochromatic case: the GVD term is neglected:

  1. if all nonlinear terms may be neglected, the stationary solution is a Bessel beam;

  2. in the case of (instantaneous) Kerr effect alone, and Kerr effect plus nonlinear losses, the solution is the family of the *nonlinear unbalanced Bessel beams* [140]. These are Bessel beam-like profiles in which, in the multiphoton absorption case, the inward energy flux is greater than the outward one in order to sustain the nonlinear losses in the central core;

3. if nonlinear losses may be neglected, one stationary non-conical solution is the Townes profile;

- Case with dispersion term:

  1. the linear case: the family of linear X-waves (O-waves in the case of anomalous dispersion), described by the spectral relation Eq. (2.2);

  2. in the case with Kerr effect and Kerr effect plus multiphoton absorption, the solution is a generalization of linear X-waves [141]. These Nonlinear X- and O-waves [142] are qualitatively similar to the linear case and, similarly to the unbalanced Bessel beam case, in presence of nonlinear losses exhibit unbalanced profiles between inward and outward energy flux to sustain nonlinear absorption.

The X-wave model therefore considers these non-diffractive and non-dispersive solutions as attractors for the filamentation process and the filament itself may be interpreted and effectively described as an X-wave, justifying most of the properties of the filamentation regime common to CWPs.

Each of the daughter peaks generated during the filamentation regime is then regarded as corresponding to an effective X-wave solution. In particular, these X-wave profiles related to the leading and the trailing peak exhibit an envelope velocity larger and smaller than the group velocity of the initial Gaussian pulse, respectively. This interpretation is supported by experimental spectra and numerical simulations.
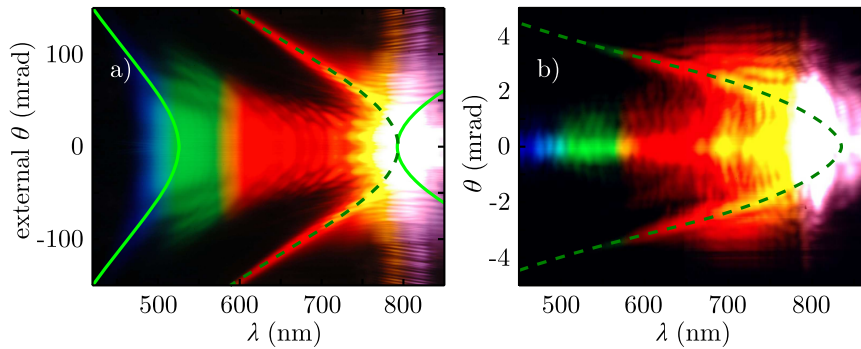
Figure 2.5: Farfield (λ, θ) spectra from filamentation regimes of 800 nm laser pulses: a) in sapphire, b) in air. The spectra were recorded with a modified (in order to record also part of the infrared region) professional camera. The propagation angles in the sapphire case correspond to external angles (i.e. measured in air). Superimposed to the spectra, best fitting curves with the X-wave spectral relation, Eq. (2.2), for $v < v_g$ (continuous light green curve) and $v > v_g$ (dashed dark green curves).

Typical experimental filamentation spectra are shown in Fig. 2.5, with the corresponding fit with the X-wave spectral relation, Eq. 2.2, for the cases: a) filamentation in sapphire (the angles in the figure are external angles, measured in air) and b) filamentation in air. In both cases the initial laser pulse was centered at 800 nm. The fitting curves correspond to frequency-gap X-waves. In Fig. 2.5(a) two curves are visible: one corresponding to the X-wave with envelope velocity $v < v_g$ (continuous light green curve) and one with velocity $v > v_g$ (dashed dark green curve). In Fig. 2.5(b) only the curve with $v > v_g$ is visible.

Chapter 3

Energy density flux

In this chapter we will define and introduce the energy density flux vector as a characterization tool for representing and interpreting the information stored in the phase of optical pulses. In particular, by applying this tool to strongly space-time coupled pulses, such as CWPs, see section 2.3, we will show how the use of this analysis tool enables a better understanding of the propagation dynamics of such pulses in their local reference frame. We will extend the definition of this vector to the case of nonlinear propagation in Kerr media with nonlinear losses. By means of recently developed intensity and phase retrieval techniques, we will apply this theoretical tool to real experimental data, in particular to the regime of ultrashort laser pulse filamentation to reach a better outlook on the dynamical processes involved. In the last section we will present a possible use of this tool as a phase retrieval instrument.

3.1 Definitions of energy density flux

We consider an optical pulse of central frequency ω_0 propagating in the forward direction in a dispersive medium. The equation governing the propagation of the envelope A of the complex electric field $\mathcal{E}(x, y, z, t)$ in the reference frame moving at velocity $v_g = 1/k_0'$, is Eq. (1.27):

$$\partial_\zeta A = i\frac{1}{2k_0}\nabla_\perp^2 A - i\frac{k_0''}{2}\partial_{\tau\tau}^2 A + i\frac{\omega_0}{2\epsilon_0 n_0 c}N \tag{3.1}$$

which relies on several approximations, as seen in chapter 1:

1. *scalar approximation*: the pulse is assumed to be linearly polarized in a direction transverse to the propagation direction;

2. *paraxial approximation*: the transverse component of the wavevector is small (small propagation angles) $|\Delta\mathbf{k}_\perp|/k \ll 1$;

3. *slowly evolving envelope approximation*: the envelope shape evolves over a scale typically much larger than the wavelength λ_0;

4. *narrow bandwidth*: $|\Omega|/\omega_0 \ll 1$ which justifies a second order expansion of the dispersive terms $k(\omega)$.

For convenience, A is rescaled so that $|A|^2 = I$ represents the local intensity of the pulse.
This quantity also represents the pulse energy density in the (x, y, τ) space, since the magnetic part of the electromagnetic energy is negligible and the total pulse energy is thus given by integration of intensity over the entire space.
In the *linear case*, Eq. (1.29), $\int_{\mathcal{V}} |A|^2 \mathrm{d}x \mathrm{d}y \mathrm{d}\tau$ represents the *total energy* carried by the pulse inside the volume $\mathcal{V}$ in the (x, y, τ) space. The energy satisfies a conservation equation obtained by multiplying Eq. (3.1) by A^*, summing the result with its complex conjugate and performing the volume integration (in the linear case, with $N = 0$).
Locally, this energy conservation equation takes a form analogous to the divergence theorem

$$\partial_\zeta |A|^2 = -\widetilde{\mathrm{div}}\mathbf{F} \tag{3.2}$$

where the divergence operator is defined in the (x, y, τ) space as

$$\widetilde{\mathrm{div}}\mathbf{F} = \nabla_\perp \cdot \mathbf{F}_\perp + \partial_\tau F_\tau$$

with $\nabla_\perp = (\partial_x, \partial_y)$.
This allows for an identification of vector $\mathbf{F}$ as the flux of energy density through the surface $\mathcal{S}$ enclosing volume $\mathcal{V}$:

$$\begin{cases} \mathbf{F}_\perp = \dfrac{1}{2ik_0} \left[A^* \nabla_\perp A - A \nabla_\perp A^*\right] & (3.3) \\[2ex] F_\tau = -\dfrac{k_0''}{2i} \left[A^* \partial_\tau A - A \partial_\tau A^*\right] & (3.4) \end{cases}$$

In particular, the longitudinal component defined by Eq. (3.4) entails information on the relative redistribution of energy along the temporal (longitudinal) τ coordinate during propagation. It is therefore associated to GVD.
It is worth underlining that the expressions of Eqs. (3.3) and (3.4) are analogous to the one describing the probability current in the formally equivalent quantum-mechanics formulation based on the Schrödinger equation.
In the laboratory frame, $z = \zeta$ and $t = \tau + k_0'\zeta$; therefore the expression for the transverse component of F remains unchanged, while the longitudinal component includes an additional contribution associated with the propagation of the pulse at

velocity $v_g = 1/k_0'$:

$$F_t = k_0' |A|^2 - \frac{k_0''}{2i} \left[A^* \partial_t A - A \partial_t A^* \right] \tag{3.5}$$

If the complex envelope is written in terms of amplitude and phase $A = |A| \exp(i\phi)$, each of the energy flux components is shown to be proportional to the intensity and to the phase gradient along the corresponding direction:

$$\mathbf{F} = \frac{1}{k_0} |A|^2 \begin{bmatrix} \nabla_\perp \phi \\ -k_0 k_0'' \partial_\tau \phi \end{bmatrix} \tag{3.6}$$

Therefore, if it is possible to have access experimentally to the intensity and phase distributions of an optical pulse as recently shown, e.g. in Refs. [79, 143–146], the longitudinal and transverse components of the energy density flux vector **F** are fully determined [144].

Equation (3.6) also shows that the flux is proportional to the intensity distribution, indicating that features of a space-time coupled wavepacket may be undetectable when an (x, y, τ) intensity distribution is measured, but may become more visible in the flux distribution. For instance, the weighting effect introduced by the phase gradient may enhance the contrast in the weak tails [139, 144].

3.2 Link to the Poynting vector

In classical electromagnetism, the energy density is defined as $w = \Re\{\boldsymbol{\mathcal{E}} \cdot \boldsymbol{\mathcal{D}}^* + \boldsymbol{\mathcal{B}} \cdot \boldsymbol{\mathcal{H}}^*\}/2$, where $\boldsymbol{\mathcal{D}}$, $\boldsymbol{\mathcal{B}}$, $\boldsymbol{\mathcal{H}}$ denote the complex electric displacement (vector) field, magnetic induction and magnetic field, respectively. The evolution of the energy density is governed by the conservation equation:

$$\frac{\partial w}{\partial t} = -\mathrm{div}\mathbf{S} \tag{3.7}$$

where $\mathbf{S} \equiv \Re\{\boldsymbol{\mathcal{E}} \times \boldsymbol{\mathcal{H}}^*\}/2$ denotes the Poynting vector and the divergence operator follows here the standard definition: $\mathrm{div}\mathbf{S} = \nabla_\perp \cdot \mathbf{S}_\perp + \partial_z S_z$.

By considering the electric field as mainly directed along x-axis and with zero y-component ($|\boldsymbol{\mathcal{E}}| \simeq \mathcal{E}_x$), from Maxwell equations in the absence of free charges we have:

$$\mathrm{div}\boldsymbol{\mathcal{D}} = 0 \tag{3.8}$$

and in the temporal Fourier domain:

$$\hat{\boldsymbol{\mathcal{D}}}(\omega) = \epsilon_0 n^2(\omega) \hat{\boldsymbol{\mathcal{E}}}(\omega)$$

Eq. (3.8) is thus written as:

$$n^2 \partial_x \hat{\mathcal{E}}_x + \partial_z (n^2 \hat{\mathcal{E}}_z) = 0 \tag{3.9}$$

By treating perturbatively this equation, with a carrier-envelope decomposition $\mathcal{E} = \mathbf{A} \exp[ik_0 z - i\omega_0 t]$, we obtain the vector electric field envelope (in International system units), considering only the dominant terms:

$$\mathbf{A} = \left\{ A_x; \quad 0; \quad -\frac{1}{ik_0} \partial_x A_x \right\} \tag{3.10}$$

The magnetic induction field is obtained with a perturbative approach from Maxwell equation $\partial_t \mathcal{B} = -\nabla \times \mathcal{E}$ and a similar carrier-envelope decomposition $\mathcal{B} = \mathbf{M} \exp[ik_0 z - i\omega_0 t]$:

$$\mathbf{M} = \left\{ 0; \quad \frac{k_0}{\omega_0} A_x - i\frac{k_0}{\omega_0^2} \partial_t A_x - \frac{i}{\omega_0} \partial_z A_x; \quad \frac{i}{\omega_0} \partial_y A_x \right\} \tag{3.11}$$

From the definition of the Poynting vector and the previous expressions:

$$\begin{cases} S_x = \frac{1}{2\mu_0} \Re \left[-\frac{i}{\omega_0} A_x{}^* \partial_x A_x \right] & (3.12) \\[2mm] S_y = \frac{1}{2\mu_0} \Re \left[+\frac{i}{\omega_0} A_x \partial_y A_x{}^* \right] & (3.13) \\[2mm] S_z = \frac{1}{2\mu_0} \Re \left[\frac{k_0}{\omega_0} |A_x|^2 + \frac{ik_0}{\omega_0^2} A_x \partial_t A_x{}^* + \frac{i}{\omega_0} A_x \partial_z A_x{}^* \right] & (3.14) \end{cases}$$

By recalling that the light intensity is $I = \epsilon_0 n_0 c |A_x|^2 / 2$, we can properly rescale the electric field in order to have $|A_x|^2 = I$. By means of this rescaling, the previous equations become:

$$\begin{cases} S_x = \Re \left[-\frac{i}{k_0} A_x{}^* \partial_x A_x \right] & (3.15) \\[2mm] S_y = \Re \left[+\frac{i}{k_0} A_x \partial_y A_x{}^* \right] & (3.16) \\[2mm] S_z = \Re \left[|A_x|^2 + \frac{i}{\omega_0} A_x \partial_t A_x{}^* + \frac{i}{k_0} A_x \partial_z A_x{}^* \right] & (3.17) \end{cases}$$

These equations show that the transverse components of the energy flux vector $\mathbf{F}$, defined in this context starting from the paraxial propagation equation, coincide with the transverse components of the Poynting vector $\mathbf{S}$, thus $\mathbf{S}_\perp = \mathbf{F}_\perp$, as shown in Refs. [147–151].

The longitudinal component S_z, however, must be interpreted differently from the local longitudinal energy flux J_τ. The density of electromagnetic energy indeed includes an electric (w_e) and a magnetic (w_m) contribution and the Poynting vector represents the energy density flux for both contributions, in the laboratory frame. In contrast, the energy density flux $\mathbf{F}$ accounts for the electric part only.

By mean of the continuity equations Eqs. (3.7) and (3.2), written in the laboratory frame, and the identification $\mathbf{F}_\perp = \mathbf{S}_\perp$ within the approximations involved, we obtain a link between the two longitudinal components:

$$\partial_t F_t = \partial_z(S_z - |A_x|^2) + \partial_t(w_e + w_m) \qquad (3.18)$$

Since experimentally we usually have access to intensity and, with proper techniques, phases of the electric field only, we can evaluate the energy redistribution by mean of vector $\mathbf{F}$ as defined by Eqs. (3.3) and (3.4). On the other hand, theoretical studies in which one has direct access to $\mathcal{E}$ and $\mathcal{H}$ permit the use of the usual definition of the energy density flux based on the Poynting vector $\mathbf{S}$.

Equation (3.7) can be written as:

$$\partial_z S_z + \partial_t w = -\nabla_\perp \cdot \mathbf{S}_\perp \qquad (3.19)$$

Under the change of reference frame $\zeta = z$, $\tau = t - z/c$, Eq. (3.19) becomes:

$$\partial_\zeta S_z = -\nabla_\perp \cdot \mathbf{S}_\perp - \partial_\tau(w - S_z/c) \qquad (3.20)$$

This is the generalization of the energy conservation equation, without envelope approximation. The left hand side describes the evolution of the longitudinal component of the Poynting vector S_z with respect to the local evolution variable ζ; it may be regarded as the energy density in the (x, y, τ) space, since it represents the intensity of the optical field. The right hand side is the divergence ($\widetilde{\text{div}}\mathbf{V} = \nabla_\perp \cdot \mathbf{V}_\perp + \partial_\tau V_\tau$) of the flux vector with components $(\mathbf{S}_\perp, w - S_z/c)$ in the transverse x, y and longitudinal τ directions, respectively. The longitudinal flux component (τ-component) is then proportional to the difference between the usual density of electromagnetic energy w and the longitudinal component of the Poynting vector. The transverse component of the flux is the same as that of the Poynting vector $S_\perp$, whether the envelope approximation is made or not. These flux components do not depend on the choice of a carrier frequency or wavenumber.

This more general form, Eq. (3.20), which is expected to depend on the dispersive properties of the medium since w depends on the dielectric permittivity, is analogous to the continuity equation Eq. (3.2), which was derived in a dispersive medium under the envelope approximation and was adopted for the definition of vector $\mathbf{F}$.

3.3 Nonlinearity and absorption

In the case of nonlinear propagation, the expressions for the flux density determined in the linear case, Eqs. (3.3) and (3.4), remain valid.

As an example, we consider the nonlinear terms which describe the propagation of wavepackets such as those spontaneously formed during the filamentation of ultrashort laser pulses, section 2.5. These include the optical Kerr effect with instantaneous and delayed (Raman effect) contributions, multiphoton absorption, plasma effects (absorption and defocusing) following ionization of the medium [97, 152], summarized in Eq. (1.50):

$$
N(A) = i\frac{\omega_0 n_2}{c}T^2 \left[(1 - \alpha)I + \alpha \int_{-\infty}^{\tau} \mathcal{R}(\tau - \vartheta)I(\vartheta)\,\mathrm{d}\vartheta\right] A +
$$
$$
- T\frac{\beta^{(K)}}{2}\left(1 - \frac{\rho}{\rho_0}\right)I^{K-1}A - \frac{\sigma(\omega_0)}{2}\rho A \tag{3.21}
$$

By performing the further approximation $T \simeq 1$, which is linked to the narrow bandwidth approximation $|\Omega|/\omega_0 \ll 1$, and introducing $N(A)$ from Eq. (3.21) into Eq. (3.1), we obtain the nonlinear counterpart of the continuity equation Eq. (3.2):

$$
\partial_\zeta |A|^2 + \widetilde{\mathrm{div}}\mathbf{F} = -\beta^{(K)}\left(1 - \frac{\rho}{\rho_0}\right)I^K - \Re\{\sigma(\omega_0)\}\rho I \tag{3.22}
$$

The terms on the right hand side of Eq. (3.22), as described in chapter 1, represent the density of energy losses by multiphoton absorption of order K and plasma absorption by inverse Bremsstrahlung, respectively [153]. Linear absorption can be treated similarly (for example by adding an absorption term with $K = 1$).

These additional terms represent the amount of energy transferred from the optical pulse to the medium.

3.4 Non-paraxial framework

Since non-paraxial ζ-evolution unidirectional propagation equations can only be solved in the full space-time $(\mathbf{k}, \omega)$ spectral domain, a non-paraxial generalization of $\mathbf{F}$, defined in the (x, y, τ) nearfield space, is difficult to derive. However, an easy generalization may be done in the case of wavepackets propagating under cylindrical symmetry around a main propagation angle θ_0, such as CWPs.

By starting from Eq. (2.1), within a second order expansion of $k(\omega)$ and a slowly varying envelope approximation ($\partial_{zz}^2 \ll \beta\partial_z$, with $\beta = k_0\cos\theta_0$ the longitudinal wavevector), the propagation equation for the envelope $\Psi(r, \tau, z)$ in the

linear case can be put in the form of Eq. (3.1):

$$2i\beta\partial_z\Psi + \nabla_\perp^2\Psi - \alpha_2\,\partial_{\tau\tau}^2\Psi + 2i\alpha_1\,\partial_\tau\Psi + \alpha_0\Psi = 0. \qquad (3.23)$$

where $\alpha_2 = k_0 k_0'' + (k_0')^2 - 1/v^2$, $\alpha_1 = k_0 k_0' - \beta/v$, $\alpha_0 = k_0^2 - \beta^2$, and v is the envelope velocity of the wavepacket.

The associated energy flux density components are expressed as:

$$\begin{cases} F_r = \dfrac{1}{2i\beta}\left[\Psi^*\nabla_\perp\Psi - \Psi\nabla_\perp\Psi^*\right] & (3.24) \\[2ex] F_\tau = -\dfrac{\alpha_2}{2i\beta}\left[\Psi^*\partial_\tau\Psi - \Psi\partial_\tau\Psi^*\right] + \dfrac{\alpha_1}{\beta}|\Psi|^2 & (3.25) \end{cases}$$

where F_r is the component of $\mathbf{F}$ along the transverse radial coordinate r (the action of $\nabla_\perp$ on a cylindrically symmetrical function gives a vector with only an r-component).

For $v \simeq v_g$ and in the limit $\theta_0 \to 0$ these expressions reduce to the ones [Eqs. (3.3) and (3.4)] derived within the framework of the paraxial propagation equation Eq. (3.1).

3.5 Monochromatic vs polychromatic energy density flux

3.5.1 Time integrated flux - monochromatic case

After having defined the framework of the energy density flux, in these sections we will show the importance of such a tool in the study and understanding of complex pulses.
In particular, the energy density flux given by Eqs. (3.3) and (3.4) is particularly well suited to characterize polychromatic wavepackets which exhibit space time coupling and/or angular dispersion, such as CWPs.

In most cases studied in the literature, optical wavepackets are supposed to be describable in terms of separated variables with uncoupled beam (spatial) and pulse (temporal) dynamics. When experimental characterization deals with the spatial dynamics only, the temporal dynamics is assumed to be frozen and the pulse is considered as quasi monochromatic. In this case, a characterization in terms of energy flux amounts to considering the transverse component of the flux only. As shown by Eq. (3.6), $\mathbf{F}_\perp$ is proportional to the intensity of the wavepacket and to the transverse gradient of the phase. If the gradient of the phase is assumed to depend very weakly on time, the *time integrated flux* $\mathcal{F}_\perp$ can be approximated

as:

$$\mathcal{F}_\perp(x, y, \zeta) = \int \mathbf{F}_\perp(x, y, \zeta, \tau)\mathrm{d}\tau \simeq \frac{1}{k_0}\mathbb{F}(x, y, \zeta)\nabla_\perp\phi(x, y, \zeta) \qquad (3.26)$$

where $\mathbb{F}(x, y, \zeta) = \int |A(x, y, \zeta, \tau)|^2\mathrm{d}\tau$ denotes the *fluence* of the beam, which is an experimentally accessible quantity.

In contrast to the time integrated quantity $\mathcal{F}_\perp(x, y, \zeta)$, the transverse energy flux $\mathbf{F}_\perp(x, y, \zeta, \tau)$ at each propagation distance ζ gives information both on the spatial and *temporal* reorganization of energy within the wavepacket, which therefore applies for polychromatic cases as well.

For the Gaussian pulse (GP) obtained by focusing a laser beam with a lens of focal length f in a dispersive medium, the linear propagation may be described in terms of the beam and pulse parameters solely depending on the propagation distance, with the origin ($\zeta = 0$) at the focus of the lens [16]:

$$A(r, \zeta, \tau) = A_0\frac{w_0 T_0^{1/2}}{w(\zeta)T^{1/2}(\zeta)}\exp\left(-\frac{r^2}{w^2(\zeta)} - \frac{\tau^2}{T^2(\zeta)}\right) \times$$

$$\times \exp\left(ik_0\frac{r^2}{2R(\zeta)} - i\Theta(\zeta) - i\frac{\tau^2}{2k_0''L(\zeta)}\right) \qquad (3.27)$$

where the beam waist $w(\zeta)$, beam curvature $R(\zeta)$, Gouy phase shift $\Theta(\zeta)$, pulse duration $T(\zeta)$ and pulse chirp $L(\zeta)$ are respectively given by:

$$w(\zeta) = w_0\left(1 + \frac{\zeta^2}{L_{DIFF}^2}\right)^{1/2} \qquad\qquad R(\zeta) = \zeta\left(1 + \frac{L_{DIFF}^2}{\zeta^2}\right)$$

$$\Theta(\zeta) = \arctan\left(\frac{\zeta}{L_{DIFF}}\right) \qquad\qquad T(\zeta) = T_p\left(1 + \frac{(\zeta + d)^2}{L_{GVD}^2}\right)^{1/2}$$

$$L(\zeta) = (\zeta + d)\left(1 + \frac{L_{GVD}^2}{(\zeta + d)^2}\right)$$

The beam is cylindrically symmetric and r is the transverse radial coordinate. Flat temporal phase was assumed at the beginning of propagation $\zeta = -d$, defined by $f = -d - L_{DIFF}^2/d$. The quantity $L_{DIFF} = k_0 w_0^2/2$ denotes the Rayleigh length and $L_{GVD} = T_p^2/2k_0''$ the dispersion length. The pulse duration at the focus T_0 is linked to the initial pulse duration T_p by the relation $T_0 = T_p(1 + d^2/L_{GVD}^2)^{1/2}$. In Eq. (3.27) the variables are separated: the temporal (longitudinal) and the spatial (transverse) dynamics remain completely uncoupled within the approximation used to derive this equation.

The components of **F** can be calculated directly from Eq. (3.27):

$$
\begin{cases}
F_r = |A(r, \zeta, \tau)|^2 \dfrac{r}{R(\zeta)} & (3.28) \\[2ex]
F_\tau = |A(r, \zeta, \tau)|^2 \dfrac{\tau}{L(z)} & (3.29)
\end{cases}
$$

where F_r is the radial component. The temporally integrated ("monochromatic") flux is:

$$
\mathcal{F}_\perp = \int F_r \, \mathrm{d}\tau = \mathbb{F}(r, \zeta) \frac{r}{R(\zeta)} \tag{3.30}
$$

The sign of the transverse component is determined by the sign of $R(\zeta)$: before the focus of the lens, $\zeta < 0$, F_r (and consequently the integrated quantity) is negative, i.e. directed toward the central axis $r = 0$, while after the focus this component is positive and directed outwards.

We can compare this behavior to the one associated to spatio-temporal coupled pulses such as CWPs. In particular, we can compare it to the behavior of a PBB and a BXP. PBB and BXP are ideally infinite-energy beams due to the low decay rate of their tails along the radial coordinate r. Thus we consider apodized version of the ideal PBB and BXP, so that in the center of the Bessel zone the wavepacket may be understood as the product of a Gaussian beam (apodizer) and a CWP. In particular, to mimic the experimental generation of such CWPs, we superimposed to a Gaussian beam the phase effect (in the temporal Fourier space) due to an ideal circularly symmetric diffraction grating (PBB) or an ideal axicon (BXP).

We numerically evaluated the flux in these three cases (GP, PBB and BXP) by considering propagation in water for central wavelength $\lambda_0 = 800$ nm.
The GP parameters are: $w_0 = 0.03$ cm, $T_p = 80$ fs and $f = 4$ cm.
The PBB and BXP have the same propagation angle $\theta_0 = 2°$, temporal duration $T_p = 80$ fs, and Gaussian apodization with $w_0 = 0.1$ cm.

Figure 3.1 shows the time integrated transverse flux $\mathcal{F}_\perp(r, \zeta)$ (radial component) as a function of the propagation distance ζ (evolution parameter) and radial coordinate for the three cases under examination. The focused GP case, Fig. 3.1(a), presents inward directed (negative) flux before the beam waist position at $\zeta = 0$, and outward directed (positive) beyond the focus, due to linear diffraction, as expected from Eq. (3.30).
As shown in Figs. 3.1(b) and 3.1(c), the PBB and BXP cases cannot be distinguished by their characterization in terms of time integrated flux. Both exhibit an integrated flux qualitatively similar to that of the GP, with an initial inward-directed flux, followed by a region (corresponding approximatively to the center of the Bessel zone) in which the flux vanishes and finally an outward directed flux. This behavior is strictly connected to the spatial apodization, as discussed in the
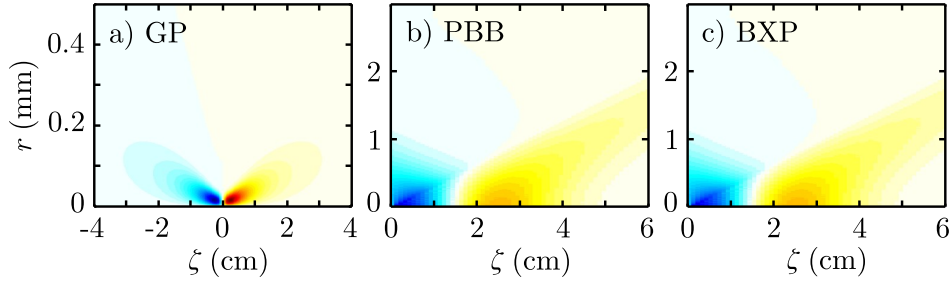
Figure 3.1: Time integrated transverse flux $\mathcal{F}_\perp$ profiles as a function of radial coordinate and propagation distance for a) a focused GP - b) a PBB - c) a BXP. Red color indicates outward flux ($\mathcal{F}_\perp > 0$) with respect to the propagation axis. Blue indicates flux towards the axis ($\mathcal{F}_\perp < 0$).

next sections. For longer propagation distances, the flux becomes ring-shaped in the transverse (x, y) plane, which corresponds to the farfield of a PBB or a BXP, since their spectrum is a ring with peak intensity centered around angle θ_0.

3.5.2   Energy flux in the polychromatic case

The representation at fixed ζ of F_r in the nearfield (r, τ) domain allows us to discriminate between the three cases examined in the previous section. Figure 3.2 shows the change in the transverse flux distribution for the GP, PBB and BXP cases as a function of the propagation distance.

The wavepackets, before the focus of the GP, or at the very beginning of the Bessel zone, are depicted in Figs. 3.2(a)–3.2(c). The GP transverse flux does not present any particular feature in the (r, τ) domain, and the pulse as a whole is focusing, since $F_r < 0$. The PBB and the BXP present an inward-directed energy flux, featured by the intensity distribution of the wavepacket itself. Even if the intensity distribution is almost identical for the GP and the PBB (the difference is only due to the different beam width of the GP and the Gaussian apodization), the distribution of the energy density flux is different because it takes into account also the phases of the wavepackets.

Figures 3.2(d)–3.2(f) show the three cases at the beam waist, or at the center of the Bessel zone. The GP transverse flux [Fig. 3.2(d)] is considerably smaller with respect to the previous case, since the spatial phase is flat in correspondence of the beam waist. As seen in the temporally integrated quantity, Fig. 3.1(a), the flux density reaches a minimum and a maximum just before and just after the beam waist [located at $\zeta = 0$ in Fig. 3.1(a)], respectively.

The BXP flux, Fig. 3.2(f), presents two wings: one in the leading part of the pulse with inward flux and one in the trailing part with outward-directed flux. The PBB can be regarded as a degenerate BXP, since propagation angle θ_0 and pulse

tilt angle δ are opposite, so that the inward-flux and outward-flux wings spatially overlap [see Fig. 3.2(e)], as schematically represented in the previous chapter in Fig. 2.1.

Figures 3.2(g)–3.2(i) show the flux characterizing the GP, PBB and BXP at a larger propagation distance. The energy flux is directed outward for all the three wavepackets and exhibits characteristic features of the intensity distribution in the farfield region, which corresponds to a diverging Gaussian beam for the GP and a diverging ring for the PBB and the BXP.

Since the reference system is moving at velocity v_g, the GP remains centered around $\tau = 0$, the PBB ($v = v_g \cos\theta_0 < v_g$) for increasing propagation distance moves towards positive τ, and the BXP ($v = v_g / \cos\theta_0 > v_g$) moves towards negative τ.

3.6 Stationary envelope waves

3.6.1 Normal GVD case: X-waves

As introduced in section 2.3.2, stationary CWPs satisfy a particular spectral relation, Eq. (2.2). In this section we will show the flux of stationary CWPs with asymmetric frequency spectral weight, evaluated by means of Eq. (2.9).
We used a full dispersion relation $k(\omega)$ for the definition of these wavepackets by mean of Eq. (2.2): the expression for the flux, derived in the second order approximation, gives in this case the main contribution, since higher order terms are expected to become more important in spectral regions corresponding to zero GVD ($k_0'' = 0$). The $k(\omega)$ relation was extrapolated from the data of Ref. [154].

Figures 3.3(a) and 3.3(b) show the transverse flux F_r for X-waves corresponding to hyperbolic spectral profiles with frequency gap [region B of Fig. 2.2], central wavelength $\lambda_0 = 527$ nm, reference angle $\theta_0 = 0$ rad, Gaussian temporal frequency weight [$\hat{f}(\Omega)$ in Eq. (2.9)] corresponding to a pulse duration $T_p = 80$ fs, and Gaussian spatial apodization ($w_0 = 0.5$ mm), propagating in water for two different envelope velocities: $v = 0.9995 v_g$ [Fig. 3.3(a)] and $v = 1.0005 v_g$ [Fig. 3.3(b)], respectively smaller and larger than the group velocity $v_g = 1/k_0' = 2.20720 \times 10^8$ m/s. The flux profile is similar to the BXP case: it exhibits two characteristic tails, one in the leading and one in the trailing part of the pulse.

The inward-directed flux wing appears either in the leading or the trailing part of the pulse, according to the fact that the envelope velocity is $v > v_g$ or $v < v_g$. This behavior is not in contradiction with the fact that the overall pulse is moving in the forward direction. It may be simply understood by considering that the propagation of the central peak is the result of the cylindrically symmetric su-
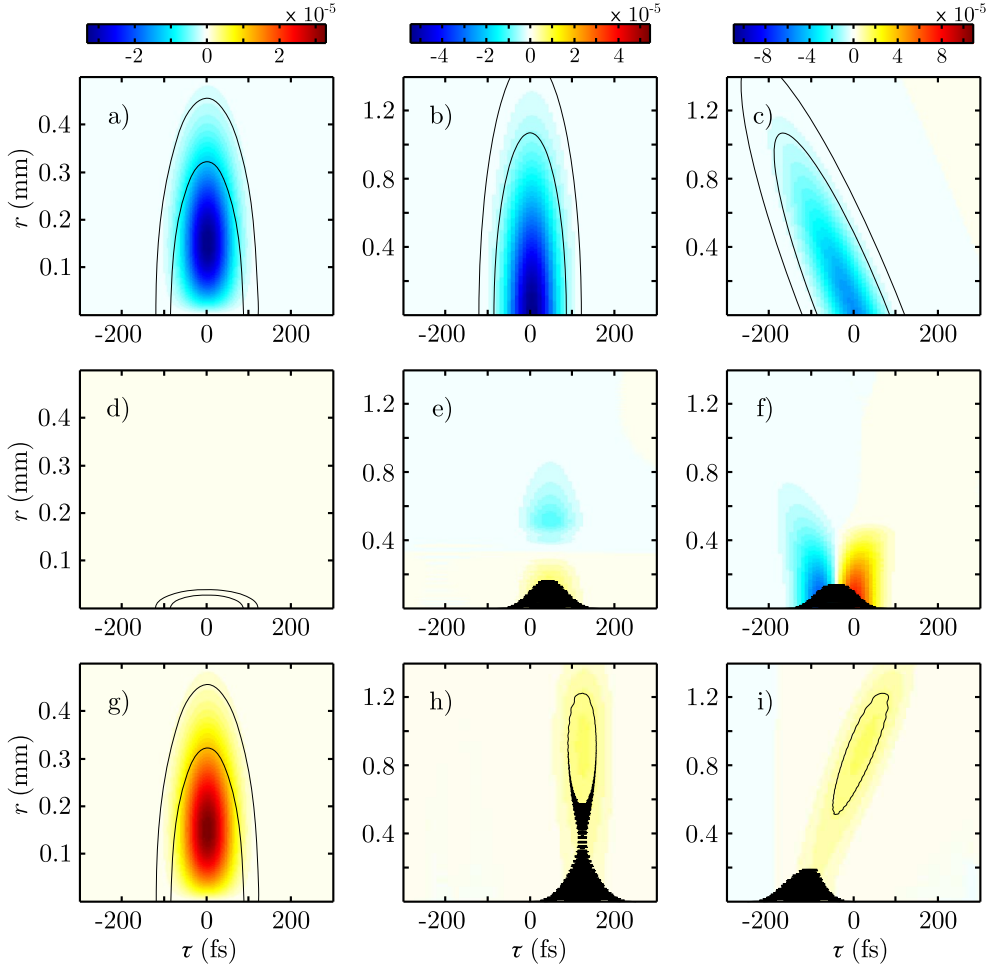
Figure 3.2: Transverse flux F_r for three different wavepackets at different propagation distances ζ. a),d),g) refer to the GP 4 cm before the focus, at the focus and 4 cm after that point, respectively. b),e),h) refer to the apodized PBB, obtained by multiplying a Gaussian profile by a radially-dependent phase, at the beginning of propagation, near the center of the Bessel zone and towards the end of this zone, respectively. c),f),i) refer to the same situation as b),e),h) for the BXP wavepacket profile. Color scale of F_r in arbitrary units. The black contour plots show the intensity distributions over 2 decades.

perposition of tilted pulses [72], as schematically represented in Fig. 2.1, so that exchanging the inward- and outward-propagating wings changes the relative position of the velocity of the axial temporal peak with respect to the group velocity v_g (in particular, with respect to the energy velocity: $v = v_g \cos\theta_0 \simeq v_g$ for small angles).

Spatial apodization limits the propagation range in which the wavepacket is
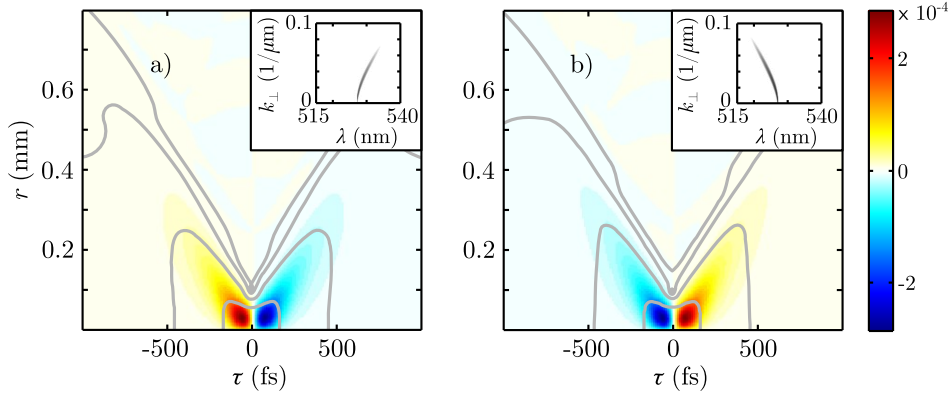
Figure 3.3: Transverse flux F_r for stationary CWP in normal GVD case (X-wave), for different propagation velocities of the envelope peak. a) $v = 0.9995 v_g$ and b) $v = 1.0005 v_g$. The gray contour plots show the intensity over 4 decades. The insets show the corresponding spectral $(\lambda, k_\perp)$ features. Color scale in arbitrary units.

effectively stationary: the behavior is qualitatively similar to the BXP case. After propagation, towards the end of the Bessel zone, the dominant wing is the residual outward-directed flux tail, which appears in the trailing or leading part of the pulse, depending on the envelope velocity.

In Ref. [88] closed-form analytical solutions for stationary CWPs with specific spectral weight functions $\hat{f}(\Omega)$, see Eq. (2.9), were given. All these analytical solutions with velocity equal to the energy velocity $v_g \cos \theta_0$ and corresponding to symmetrically distributed spectral weight turn out to have both transverse and longitudinal flux components equal to 0. The case of an asymmetric spectral weight leads to analytical solutions featuring a single branch of an X-wave with frequency gap in region B of Fig. 2.2, similar to the case treated in this section.

3.6.2 Anomalous GVD case: O-waves

Stationary CWPs in media with anomalous dispersion typically feature elliptical spectral $k_\perp(\Omega)$ profiles called O-waves [86, 155]. Similar stationary CWPs are also obtained in the case of normal dispersion [88] in region D of Fig. 2.2; however, these profiles are highly non-paraxial. By choosing a proper spectral distribution $\hat{f}(\Omega)$ around the region where the spectral curve intersects the $k_\perp = 0$ axis, to limit the wavepacket to a paraxial framework, such CWPs become almost identical to a single branch X-wave profile, examined in the previous section.

In this section we will thus study the O-wave case within the paraxial approximation by considering the propagation in a medium with anomalous GVD ($k_0'' < 0$). As for the previous section, we will consider the full dispersion relation in the definition of the wavepacket, and an asymmetrical spectral weight.

Figure 3.4 shows the transverse flux F_r for O-wave wavepackets propagating in water at central wavelength $\lambda_0 = 1300$ nm ($k''(\lambda) = 0$ in water at $\lambda \simeq 1000$ nm) and angle $\theta_0 = 0.005$ rad, Gaussian spectral weight corresponding to $T_p = 40$ fs, Gaussian spatial apodization ($w_0 = 0.6$ mm), and peak velocity a) $v = 0.9995v_g$ and b) $v = 1.0005v_g$, smaller or larger than $v_g = 2.22930 \times 10^8$ m/s, respectively. Although the nearfield profiles of these wavepackets are definitely different from the X-wave cases, since they exhibit a characteristic elliptical structure, the flux profiles are analogous to the X-wave cases and, as before, the position of the inward-directed energy wing is still linked to the value of the envelope velocity v with respect to the energy velocity $v_g \cos \theta_0$ (in the previous case this coincided with v_g since the main propagation angle was chosen as $\theta_0 = 0$).
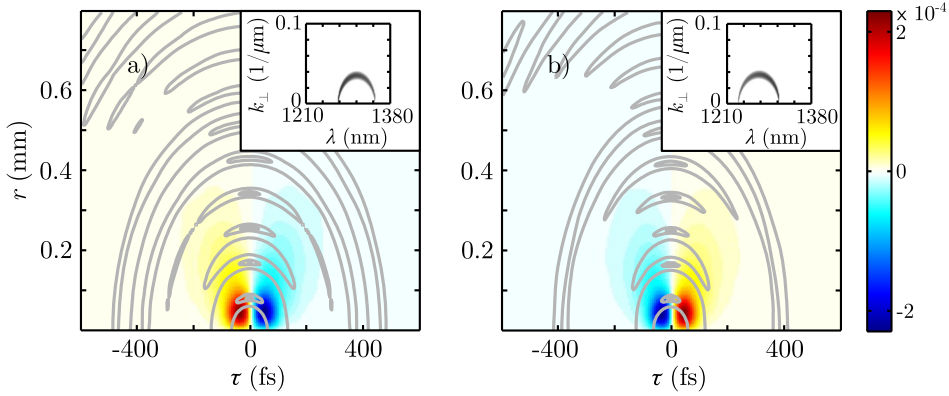
Figure 3.4: Transverse flux F_r for stationary CWP of the O-wave type in anomalous GVD regime ($k_0'' < 0$), for different propagation velocities of the envelope peak. a) $v = 0.9995v_g$ and b) $v = 1.0005v_g$. The contour plots show the intensity over 4 decades. The insets show the corresponding spectral ($\lambda, k_\perp$) features. Color scale in arbitrary units.

3.7 Longitudinal component

In the previous sections we considered only the transverse component of the energy flux **F**, which coincides with the transverse component of the Poynting vector and whose definition does not depend on the velocity of the wavepacket under examination. In this section, we will show that the longitudinal component of the energy flux also constitutes an important source of information. Monitoring this component in the frame moving at the velocity of the envelope peak allows us to diagnose the energy redistribution occurring within the wavepacket.

3.7.1 Longitudinal component of the energy flux

In the frame moving at $v_g = 1/k_0'$, the longitudinal flux component F_τ is related to the chromatic dispersion of the pulse, as underlined by Eq. (3.4). In both cases of normal and anomalous GVD, a Gaussian pulse with initial flat phase develops during propagation a longitudinal flux component featured by two side lobes in the leading and in the trailing part of the pulse: the leading lobe is directed toward negative times and the trailing lobe toward positive times [Fig. 3.5(a)]. This indicates that the pulse is broadening along the temporal coordinate during propagation because of GVD.

In contrast, if the pulse has an initial negative chirp and propagates in a normally dispersive medium ($k_0'' > 0$), each side lobe corresponds to a longitudinal flux with opposite sign, indicating pulse compression during propagation as expected in this case from the action of normal GVD.
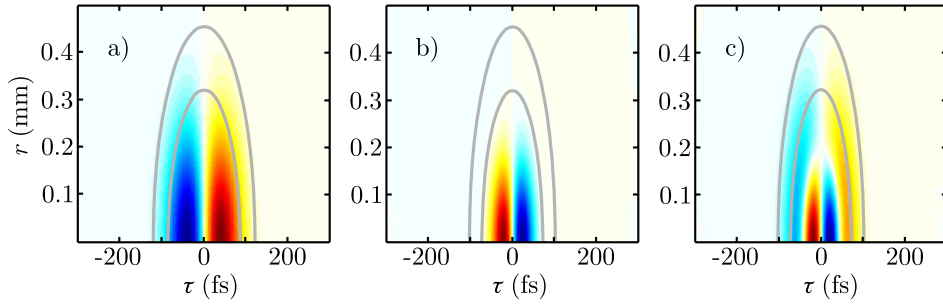
Figure 3.5: Longitudinal flux F_τ for a GP propagating in different regimes. a) linear propagation with normal GVD. b) Nonlinear propagation (high intensity) with anomalous GVD ($\lambda_0 = 1300$ nm in water). c) Nonlinear propagation with anomalous GVD at lower intensity with respect to case b). The color scale of F_τ indicates flux towards positive (resp. negative) τ values in red (resp. blue). The gray contour plots show normalized intensity contours over 2 decades, i.e. for $I/I_{max} = 10^{-1}$ and 10^{-2}.

The case of nonlinear propagation in a Kerr medium with anomalous dispersion ($k_0'' < 0$) is particularly instructive. As shown in section 3.3, the expression for $\mathbf{F}$ also holds for nonlinear propagation.

Self-phase modulation induced by the optical Kerr effect generates new frequencies in the regions of the pulse with the strongest intensity gradients [see 1.5.1]. In particular, a focusing Kerr nonlinearity generates upshifted or downshifted frequencies with respect to the central frequency ω_0 in the decreasing or growing part of the pulse, respectively, i.e. in the trailing and leading edge of the pulse. In conjunction with anomalous GVD, this effect is responsible for pulse shortening during propagation, since self-phase modulation frequency generation determines an effective negative chirp.

Figure 3.5(b) illustrates the longitudinal flux obtained in this situation: each lobe of F_τ exhibits an opposite sign with respect to the linear propagation case. As a comparison, Fig. 3.5(c) depicts the longitudinal flux associated with the nonlinear propagation of a GP with lower energy and pulse intensity than that of Fig. 3.5(b). Self-phase modulation is in this case weaker and the newly generated frequencies are not able to overcome linear dispersion over the whole pulse, but only in the central region where the intensity is higher. Nonlinear effects thus dominate in the central high intensity core and the flux points inwards thus leading to a local temporal compression, while the surrounding low intensity regions behave almost linearly with an outward-directed flux. Such a behavior leads to the progressive distortion of the pulse.

3.7.2   Radially averaged longitudinal flux

In analogy with the evolution of the temporally averaged transverse flux depicted in Figs. 3.1(a)–(c), the evolution of the *radially averaged* longitudinal flux $\mathcal{F}_\tau$ may be a relevant quantity for a system in which the evolution along the transverse spatial coordinates is negligible or fixed by the geometry of the system, such as the case of a pulse propagating inside an optical fiber.

Figures 3.6(a) and 3.6(b) show the power (spatially integrated intensity) and the longitudinal flux $\mathcal{F}_\tau$, respectively, versus propagation distance ζ, for the linear propagation of a pulse with an initially Gaussian spectral distribution and strong quadratic and cubic phase chirp. The pulse spectra is therefore in the form:

$$\hat{A}(\Omega) \propto \exp(-\Omega^2 T_p^2/4 + iC_1\Omega^2 + iC_2\Omega^3)$$

The dispersion parameters correspond to propagation in water at a central wavelength of $\lambda_0 = 527$ nm. Diffraction was neglected.

The intensity pattern depicts an intense temporal peak whose instantaneous velocity v varies during propagation, following the relation $1/v = 1/v_g + d\tau/d\zeta$. In the local frame moving at v_g, the instantaneous velocity of this peak is given by the first derivative of the (τ, ζ) intensity distribution curve. The curvature of this intensity distribution thus represents the peak acceleration: in Fig. 3.6(a), the peak exhibits a constant deceleration (since velocities larger than v_g correspond to a relative motion towards negative τ).

The peak velocity is larger than v_g for the first ~ 20 cm and smaller afterwards. This behavior is governed by the cubic chirp, while the distance ζ at which the peak travels at v_g (i.e. the z position for which $d\tau/dz = 0$, or the vertex of the parabola described by the intensity curve) is determined by the quadratic chirp.A cubic chirp of opposite sign would lead to a constant acceleration, due to the change of the curvature sign.

The longitudinal component of **F** shown in Fig. 3.6(b) underlines the deceleration property: in correspondence of the main peak a net flux is directed towards negative times in the region $v > v_g$, and in the opposite direction in the region $v < v_g$. However, the overall pulse presents a broad series of secondary intensity peaks associated with a flux of opposite sign. This indicates, as expected, that the center of mass of the entire pulse energy does not change during propagation in spite of the peak deceleration. Furthermore, for large propagation distances (final part of Fig. 3.6(b), for $\zeta \gtrsim 45$ cm) the flux pattern becomes similar to the one obtained for a GP subject to normal GVD (e.g. Fig. 3.5(a)).

This acceleration property given by a third order spectral phase component is at the basis of the behavior of the self-accelerating finite-energy Airy Beam [9, 10].
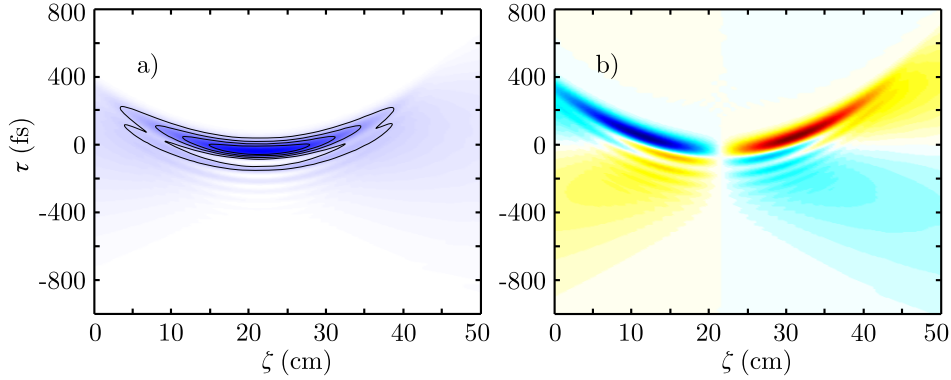
Figure 3.6: a) Linear scale of the intensity plot, and b) longitudinal flux $\mathcal{F}_\tau$ as a function of propagation distance z and temporal longitudinal coordinate τ for a GP with strong quadratic and cubic spectral frequency chirp. For both figures, the temporal axis refer to the local frame moving at $v_g = 1/k_0'$. The color scale of $\mathcal{F}_\tau$ indicates flux towards positive (respectively negative) τ values in red (respectively blue).

3.8 Nonlinearity and absorption

As previously shown, section 3.3, **F** represents the energy density flux also in the case of absorptions, provided that the continuity equation Eq. (3.22) includes the "sink" term associated to these effects.

Nonlinear CWP profiles which maintain an intensity-invariant shape in the presence of nonlinear losses (multiphoton absorption) have been derived [140, 142] starting from the envelope equation, Eq. (1.27).
Numerical solutions called unbalanced nonlinear Bessel beams (UBB) have been

found for the monochromatic case and unbalanced nonlinear O-waves (UBO) for the polychromatic case in the regime of anomalous GVD.

Following the procedure of Ref. [142], we numerically evaluated the nearfield profiles of UBB and UBO and the associated energy flux.

Figure 3.7 shows the vector representation of $\mathbf{F}$ for an UBO. The parameters were chosen to represent dispersion and nonlinear losses for water at $\lambda_0 = 1300$ nm (anomalous GVD).

The energy flux is directed towards the center of the pulse, corresponding to the peak of the intensity distribution, where the main amount of multiphoton absorption takes place. In the ideal case of a linear stationary O-wave moving at velocity v_g, within the framework of Ref. [142], the net flux is 0 since the incoming energy stream is exactly compensated by the outcoming one, analogously to the ideal PBB case. From a mathematical point of view, this corresponds to flat spatio-temporal phase for the complex envelope A.

In the unbalanced case, however, the central core, i.e. the most intense part of the wave, is continuously replenished since the amount of inward energy is larger than the outward stream (hence the name "unbalanced"). This surplus energy flux carried by the conical tail is exactly compensated by the amount of losses in the central core, thus sustaining the stationary propagation.

3.9   Experimental characterization

The energy flux analysis, as described in the previous sections, requires the knowledge of both intensity and phase information of an ultrashort pulse in the full spatio-temporal domain at given propagation distance.

The development of spatio-temporal intensity and phase retrieval techniques opens thus the possibility of applying this numerical tool to an experimental environment, to gain a deeper understanding of the pulse dynamics.

As an example, we used the energy density flux in two different experimental frameworks: the linear propagation of a BXP and the highly nonlinear propagation regime arising from the filamentation of ultrashort laser pulses.

3.9.1   The "Shackled" FROG

The reconstruction of the electric field complex envelope in the linear case was performed by mean of a combination of the Frequency-Resolved-Optical-Gating (FROG) technique [156] for the retrieval of the temporal profile of the pulse with a spatial nearfield measurement with an Hartmann-Shack (H-S) sensor [157]. This technique was thus called "Shackled" FROG [79, 158].
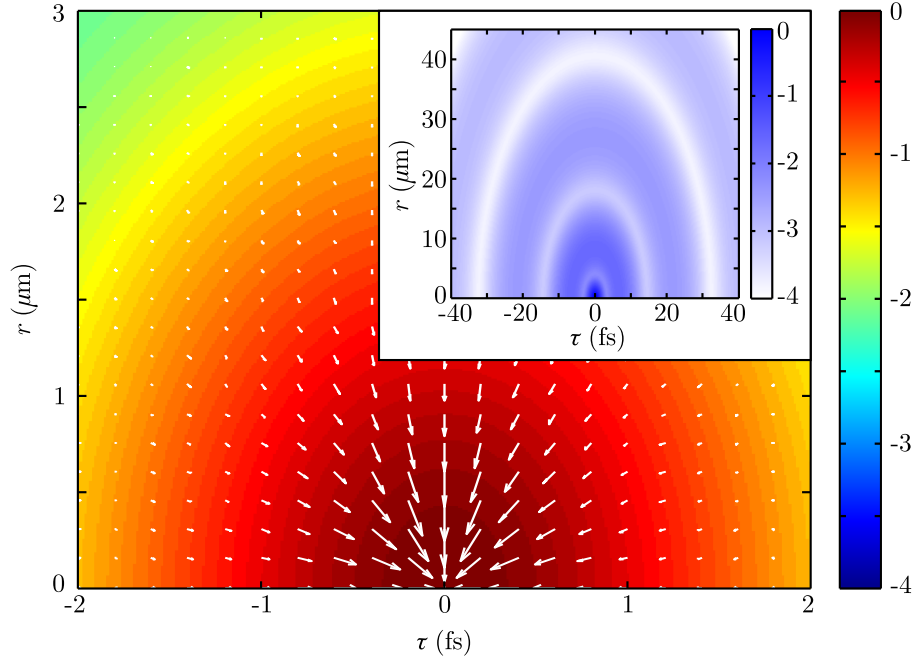
Figure 3.7: Vector plot of the energy flux **F** for the main intensity peak of an unbalanced nonlinear O-Wave (UBO) with stationary envelope propagating at $v_g = 1/k_0'$, superimposed to the intensity distribution of the UBO plotted over 4 decades. In the inset, the intensity plot over 4 decades of the UBO profile over a larger scale.

The temporal profile of the pulse at a single radial position was characterized by a standard Second Harmonic Generation (SHG) FROG measurement, while the spatial characterization was performed with a home-made H-S sensor. The H-S sensor consisted of a regular array of transmissive Fresnel zone plates, that play the same role of the lenses in the standard H-S sensor.

Each portion of the spatial profile of the beam is focused by the grid of lenses; the displacement $\Delta(x, y)$ of the focused spots from each lenslet with respect to the projection of the center of the respective Fresnel zone plate on the detector, will give the spatial phase derivative of the pulse. By a simple integration the wavefront in terms of relative displacement (with respect to a flat wavefront) is retrieved, and the adimensional phase is obtained by multiplying such quantity by $2\pi/\lambda$.

The spatial phase retrieved at each wavelength is uncorrelated with respect to the others. The link along the temporal axis between each spatial phase profile is performed by mean of a single FROG measurement at a given coordinate (x, y), with the constraint that all frequencies are present at this spatial position. In the case under examination, the couple $x, y = 0$ was chosen.

This procedure is easily applicable to the BXP case, since the propagation an-

gle is the same for each frequency. In a different case, the procedure requires a series of measurements with the H-S for each different frequency, which can be achieved by the use of a set of interferential filters [159], or an imaging interferometer configuration [158].

As described in Ref. [79], this technique was applied to an apodized BXP propagating in air, generated by sending a 790 nm, 33 fs, 4 mm FWHM diameter GP through a fused silica axicon with a base angle of $\alpha = 2.5°$. Under the condition that the dispersion of the axicon material is negligible, $\theta(\omega) = \theta_0$, so that only a single spatial measurement was performed. This allowed the retrieval of the spatial phase for each wavelength. The experiments and the intensity and phase retrieval were carried on by F. Bonaretti, D. Faccio and M. Clerici of the Ultrafast Nonlinear Optics group of Prof. P. Di Trapani, Università degli Studi dell'Insubria, Como, Italy, at the Institut de Ciències Fotòniques (ICFO), Castelldefels (Barcelona), Spain, with the help of the Attoscience and Ultrafast Optics group of Prof. J. Biegert.
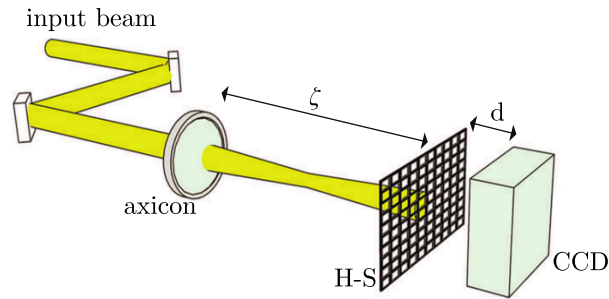
Figure 3.8: Setup for the H-S measurements; d is the focal distance of the Fresnel zone plates H-S sensor. The measurements were performed scanning the evolution of the pulse along the propagation direction ζ. Courtesy of F. Bonaretti.

The spatial measurements were performed with a CCD placed in the focal plane of the H-S sensor, as represented in Fig. 3.8; the whole set was moved at different propagating positions along the Bessel zone to scan the evolution of the spatio-temporal profile. The temporal profile of the pulse was measured independently by using a standard SHG FROG technique on the $r = 0$ coordinate of the input GP before the axicon, assuming that no changes occur in the temporal characteristics of the pulse along the direction of propagation.

We applied the energy density flux tool to the experimental data. Figure 3.9 shows the transverse y-component of vector $\mathbf{F}$. It experimentally verifies the numerical evaluation of Fig. 3.2. Red (blue) color in this case means flux directed toward positive (negative) values of the vertical (spatial) axis. In particular, at the very beginning of the Bessel zone [Fig. 3.9(a)], the flux is directed toward the central axis $y = 0$ for both wings above and below the axis,

i.e. it is negative for the wing above the axis and positive for the one below $y = 0$. At the center of the Bessel zone [Fig. 3.9(b)], the pulse exhibits the typical X-shaped structure of BXP with wings of inward- and outward-directed energy. After the Bessel zone [Fig. 3.9(c)], the pulse is reshaped into a diverging ring (spatial farfield of a BXP), as underlined by the outward-directed (with respect to the central axis) energy flux.
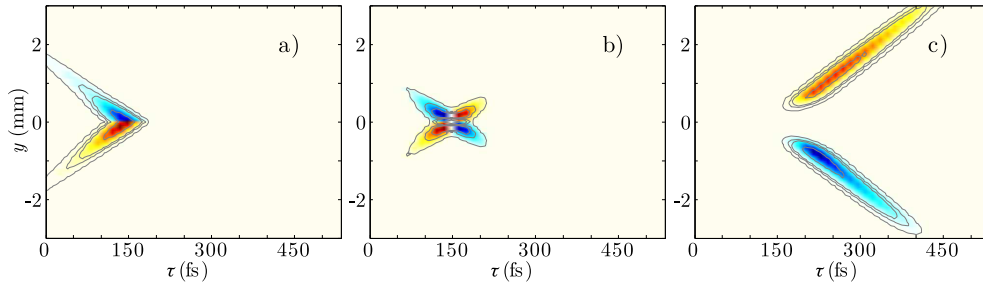
Figure 3.9: Experimentally evaluated Cartesian component F_y of the transverse flux $\mathbf{F}_\perp$ for a BXP at different propagation distances. The local reference system travels at the velocity of the main central peak of the wavepacket. a) refers to the very beginning of the Bessel zone. b) refers to the center of the Bessel zone. c) refers to the pulse after the end of the Bessel zone. F_y is renormalized to its maximum value for every image. The contour plots show the intensity over 2 decades. The vertical axes are spatial y-axes, not radial r-axes as in Fig. 3.2. Red, respectively blue, color thus represent flux directed toward the positive, respectively negative, direction of the vertical axis.

3.9.2 The Gerchberg-Saxton technique

The energy flux technique was also used on a dynamical highly nonlinear profile such as the one generated during the filamentation process of ultrashort laser pulses.

As explained in section 2.5, high power laser pulses undergo self-focusing in nonlinear Kerr media: the collapse is eventually arrested by multiphoton absorption or higher order nonlinear processes and the pulse reshapes into a tightly localized intensity peak that propagates sub-diffractively over many diffraction lengths. This peak is surrounded by a larger energy reservoir and the interaction between the core and the reservoir sustains the long-range nonlinear propagation. This allows to foresee applications based on long distance nonlinear interaction or on the transport of high intensities over long paths [15].

The filament was generated by focusing ($f = 50$ cm) a 160 fs, 800 nm, 3.3 μJ laser pulse in a water cell [144].

In order to retrieve the pulse amplitude and phase, a technique based on a near-(r, t) and farfield (θ, λ) intensity measurement and the Gerchberg-Saxton iterative error-reduction algorithm was introduced.
The characterization of the laser pulse filament was thus based on two separate measurements:

- The first was a 3D tomographic mapping [160] of the pulse space-time intensity profile obtained by overlapping the pulse under study with a flat-top, 5 mm diameter (FWHM), 720 nm, 20 fs gate pulse, generated by a commercial noncollinear optical parametric amplifier (NOPA), on a second order nonlinear crystal (BBO crystal), Fig. 3.10(a). The sum-frequency signal generated by the nonlinear BBO crystal, recorded with a CCD camera, reproduces the pulse spatial profile within the temporal window of the gate pulse. Changing the relative delay between the gate and the laser pulse reconstructs the full space-time intensity profile of the laser pulse itself, Fig. 3.10(b).

- The second measurement was a measure of the angularly resolved (θ, λ) spectrum, Fig. 3.10(d). This was obtained by sending the spatial farfield of the filament, i.e. the intensity distribution in the focal plane of a lens, onto the input slit of an imaging spectrometer, and the output (θ, λ) spectrum was recorded with a CCD camera [138], Fig. 3.10(c). From this measurement, the $(k_\perp, \omega)$ intensity spectrum was obtained.

The experiments were carried on by D. Faccio, A. Matijošius and F. Bragheri at the Department of Quantum Electronics, Vilnius University, Vilnius, Lithuania, with the help of the Group of Ultrashort Pulse Optics of Prof. A. Dubietis.

Since the (r, t) and $(k_\perp, \omega)$ measurements form a Fourier transform pair, we used a generalization to the space-time domain of the Gerchberg-Saxton, or error-reduction, algorithm [161], usually employed in the field of spatial wave-front reconstruction.
In particular, phase retrieval was obtained via an iterative algorithm in which the complex envelope is Fourier-transformed back and forth, each time substituting the corresponding measured (r, t) or $(k_\perp, \omega)$ amplitude profile, starting from an initial phase guess. The algorithm was run using measured data for a total of 400 iterations with an initial quadratic guess function for the phase profile. By varying the input phase curvature, the algorithm converged to results similar to the ones represented in Fig. 3.11.
The Gerchberg-Saxton algorithm is afflicted by an ambiguity in the sign of the retrieved phase, e.g. it cannot discriminate between a focusing or a defocusing Gaussian beam. This ambiguity can be removed if the sign of the phase is actually
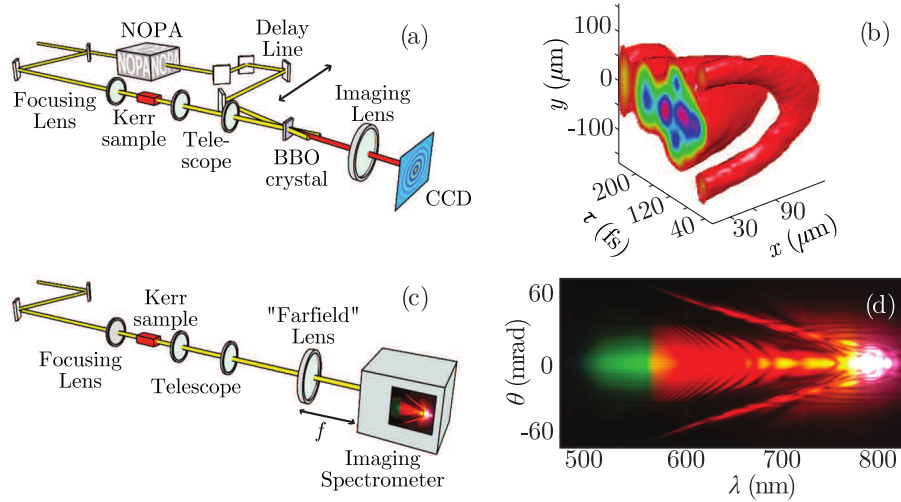
Figure 3.10: Setup for the Gerchberg-Saxton technique measurements. (a) Experimental setup for the 3D tomographic technique based on second-order sum frequency generation. (b) The intensity profiles at different temporal delays between the pulse under examination and the gate, recorded by a CCD camera, are used to reconstruct a three-dimensional image of the wavepacket in the space (x, y, τ). (c) Experimental setup for the farfield (θ, λ) measurements: an imaging spectrometer is placed in the focal plane of a converging lens, so that the components at different wavelengths are spatially displaced at the exit of the instrument. The spectral distributions are then recorded by a CCD camera. (d) Farfield spectrum of the filamentation regime in real colors, taken with a color Nikon digital camera.

known a priori. This was indeed the case for the input pulse ($\zeta = 0$ cm) as it was focused into the medium with a positive lens.

From the amplitude and phase information retrieved by the algorithm, we calculated the space-time energy-density flux in the reference frame moving at v_g. Figures 3.11(a) and 3.11(b) show the transverse flux F_y and the longitudinal F_τ for the input focusing GP, respectively. The grey curves show the contours of the pulse space-time intensity profile in logarithmic scale over 2 decades. Blue (red) regions indicate a flux directed towards negative (positive) values of the (spatial) vertical or (temporal) horizontal axis.

The transverse flux clearly shows an inward flow toward the center of the pulse ($r = 0$) as expected for a linearly focusing GP. The longitudinal flux shows two components, both flowing outward with respect to the center ($\tau = 0$) of the pulse. This flux, as explained in the previous sections, is related to linear dispersion. These figures are qualitatively equivalent to the numerical cases of Figs. 3.2(a) and 3.5(a), respectively.

Figures 3.11(c) and 3.11(d) show the fluxes after 1 cm of propagation. Non-
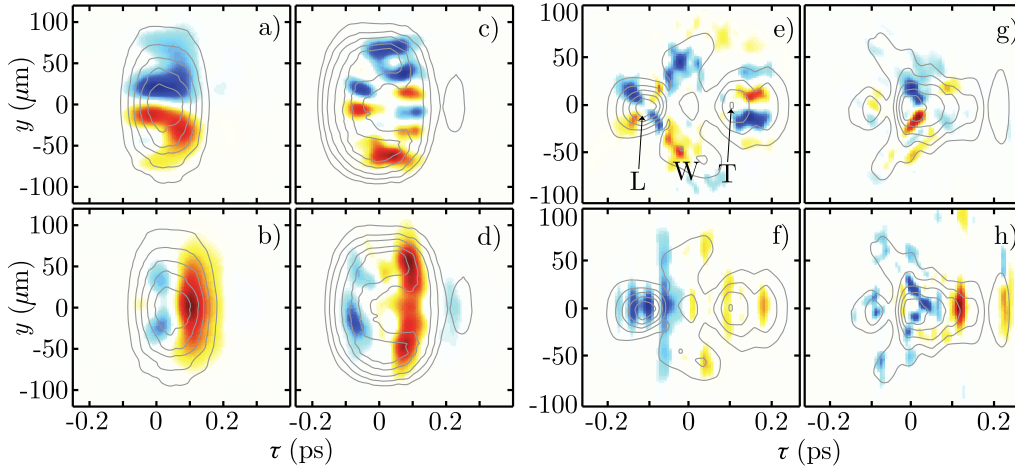
Figure 3.11: Experimentally retrieved energy density flux profiles for a laser pulse undergoing filamentation in water. Blue indicates a negative (opposite to the axis direction), Red indicates a positive (same as the axis direction) flux. (a), (c), (e) and (g) show the normalized (y, t) distribution of transverse flux for the input focused pulse, for the pulse after 10 mm, 20 mm and 40 mm of nonlinear propagation, respectively. (b), (d), (f) and (h), under the same conditions, show the longitudinal fluxes. The gray contour plots show the intensity profile over 2 decades (0.4 decade spacing between each contour line). In (e), L, T and W mark the leading peak, the trailing peak and the central (reservoir) wings, respectively.

linear effects on the pulse are clearly visible: F_y shows an inward flow toward the center due to linear focusing and self-focusing in correspondence of the leading region and the outer regions, while the trailing part exhibits a flux with opposite direction (i.e. outward directed). This defocusing behavior of the energy flux, associated with a horn-shaped profile of the intensity may be a signature of defocusing arising from the generated plasma [15].

Figures 3.11(e)–3.11(f) and 3.11(g)–3.11(h) show the energy flux components for the fully formed filament. The pulse is split into two daughter pulses (pulse splitting) and the leading pulse ("L" in the figure) shows a marked X-shaped structure in the transverse flux distribution. The X-shaped pattern underlines the presence of a conical energy flux that is bringing energy from the surrounding reservoir into the central intensity peak. The trailing pulse ("T" in the figure) is still affected by plasma defocusing and shows a marked outward flux. We note the presence of an off-axis ring ("W" in the figure) that is focusing toward the pulse axis. The conical X-shaped transverse-flux is still clearly visible after 40 mm propagation [Figs. 3.11(g) and 3.11(h)]: the energy has recombined toward the pulse center and another pulse splitting event has occurred after the one of Figs. 3.11(e)

and 3.11(f).

These results strongly support the presence of spontaneously formed CWPs inside the filamentation regime [97, 122, 162]. Indeed, the transverse flux profiles closely resemble the patterns seen in the BXP or X-wave cases, Figs. 3.2(f) and 3.3(b). Moreover, the inward-directed wing is in the front part of the leading pulse intensity peak, similarly to the examples of CWPs with velocity $v > v_g$.
The interpretation of the longitudinal flux in the fully-formed filament is more complicated.

We performed numerical simulation of the filamentation regime by mean of Eqs. 1.49 and 1.50, for both condensed [153] and gaseous media [98] and applied the energy density flux analysis. The results are very close to the experimental measurements.

In Fig. 3.12 we show a numerically simulated laser filament intensity with its transverse and longitudinal flux distribution using input conditions which reproduce the experimental measurements. Each feature retrieved in the experimental figures may be also recognized in the numerical figure. In particular, Fig. 3.12(a) exhibits an X-shaped flux structure associated to the leading peak L, resembling the X-wave (or BXP) behavior, while the trailing peak T is characterized by a mainly outward directed flux. The inward ring W from the energy reservoir is also clearly visible, in agreement with the experimental measurement and the explanation of the filament process continuously sustained by the surrounding background.
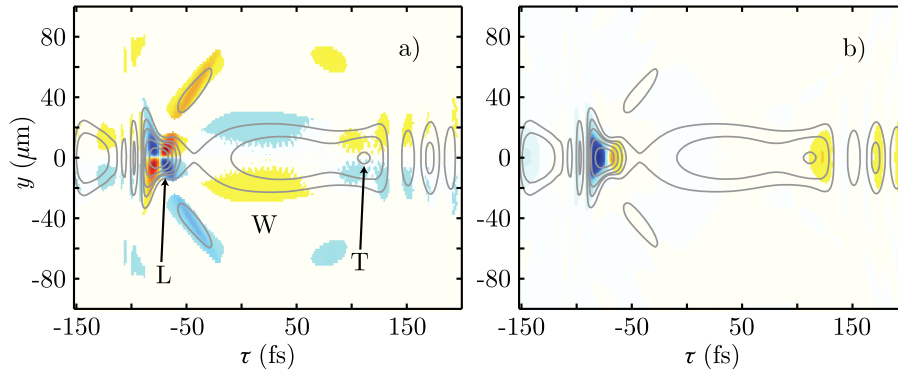
Figure 3.12: Transverse (a) and longitudinal (b) energy density flux for a numerically simulated laser filament pulse in water. The input power and focusing conditions were chosen to match the experiment. The gray contour plots show the intensity profile over 4 decades (0.8 decade spacing between each contour line). L, T and W indicate the leading peak, the trailing peak and the central wings, respectively. The main experimental features are reproduced, in particular the marked X-shaped flux associated to the main leading intensity peak

3.10   Conclusions and perspectives

In summary, in this chapter we defined the vector of energy density flux, starting from the envelope paraxial propagation equation. We showed that this quantity, linked to the Poynting vector, represents the redistribution of energy inside a wavepacket in its local reference frame, related to diffraction, dispersion and nonlinear effects, such as Kerr effect and multiphoton absorption.

We performed a series of numerical investigations based on the analysis of the instantaneous features and evolution along propagation distance of the energy density flux vector. We showed this as a valuable instrument for the investigation of spatio-temporally coupled wavepackets, such as CWPs, and in particular as a tool for retrieving information about the nature of the pulse and its propagation properties.

We finally reported two applications of this analysis tool. Indeed, the fact that it relies on the knowledge of intensity and phase of the electric field makes it a diagnostic tool also in an experimental context, thanks to the development of spatio-temporal intensity and phase retrieval techniques. By a close collaboration with experimental groups, we applied an energy density flux analysis to a linear BXP case, confirming the numerical results.
In the nonlinear case, we collaborated in the development of a novel retrieval technique based on a generalization of known algorithms, and we concentrated on the filamentation of ultrashort laser pulses. In this nonlinear filamentation case, the energy density flux analysis brought more information about the role of the energy reservoir in bringing energy toward the intense peak thereby sustaining the interaction over large distances.

As a final remark, in the next section, we propose the use of vector **F** as a possible alternative method for the complete phase retrieval of ultrashort pulses in the spatio-temporal domain.

3.10.1   Perspectives: phase retrieval

As previously shown, the energy density flux is proportional to both intensity and phase gradient, see Eq. (3.6).
On the other hand, starting from the continuity equation for the field intensity, Eq. (3.2), the knowledge of $A(r, \tau, \zeta)$ and $\partial_\zeta A(r, \tau, \zeta)$ at a given point ζ in propagation allows the reconstruction of the components of **F**.

It is thus possible to reconstruct the (r, τ) distribution of the phase gradient at given ζ position by retrieving the components of **F**, if $A(r, \tau, \zeta)$ and $\partial_\zeta A(r, \tau, \zeta)$ are known quantities. This in particular requires the measurement of the full spatio-temporal distribution at two (or more) neighbour ζ points, provided that the evolution is sufficiently slow (so that the ζ-derivative may be approximated by a fi-

nite difference). This may be achieved by a set of measurements of the space-time resolved intensity with the three-dimensional mapping technique [160] described in the previous section. Moreover, an estimate of the nonlinear absorption terms of the nonlinear continuity equation, Eq. (3.22), which are intensity-dependent, could enable such a phase retrieval procedure also in the nonlinear case (e.g. in the filamentation regime).

This approach should be distinguished in two different cases, depending on the sign of GVD dispersion.
By assuming cylindrical symmetry and renormalizing the temporal coordinate as $\vartheta = \tau / \sqrt{k_0 \left| k_0'' \right|}$, the flux components become:

$$
\begin{cases}
F_r = \dfrac{1}{k_0} I \partial_r \phi & \text{(3.31)} \\[2ex]
F_\vartheta = \mp \dfrac{1}{k_0} I \partial_\vartheta \phi & \text{for } k_0'' \gtrless 0 \quad \text{(3.32)}
\end{cases}
$$

where I is the field intensity $|A|^2$ and ϕ the phase of the complex envelope.

For the normal GVD case ($k_0'' > 0$), the continuity equation [Eq. (3.2)] and the additional condition:

$$
\partial_\vartheta F_r + \partial_r F_\vartheta = (\partial_\vartheta \ln I) \cdot F_r + (\partial_r \ln I) \cdot F_\vartheta
$$

reduces to a system of two first order coupled differential equation for the longitudinal and transverse components of **F**:

$$
\begin{cases}
\partial_r u - \partial_\vartheta v = -\dfrac{u}{r} + Z & \text{(3.33)} \\[2ex]
\partial_\vartheta u - \partial_r v = G u - L v & \text{(3.34)}
\end{cases}
$$

where $u = F_r$ and $v = -F_\vartheta$ are the unknown functions to be retrieved, and $Z = -\partial_\zeta I$, $G = \partial_\vartheta(\ln I)$, $L = \partial_r(\ln I)$ are known quantities.
The retrieval procedure may be implemented for example by mean of a leap-frog scheme [163] and considering proper boundary and initial conditions (such as $F_r, F_\vartheta = 0$ sufficiently far from the pulse, i.e. for $r \to +\infty$ and $\vartheta \to \pm\infty$, and $F_r = 0$ exactly on axis $r = 0$).

For the anomalous GVD case ($k_0'' < 0$), Eq. (3.2) becomes a non homogeneous Poisson-like problem for the phase of the complex envelope:

$$
\mathcal{Z} = \partial_{rr}^2 \phi + \partial_{\vartheta\vartheta}^2 \phi + \frac{1}{r} \partial_r \phi + L \cdot \partial_r \phi + G \cdot \partial_\vartheta \phi \tag{3.35}
$$

where $\mathcal{Z} = -k_0 \partial_\zeta(\ln I)$, $G = \partial_\vartheta(\ln I)$, $L = \partial_r(\ln I)$ are known quantities.
By adding a further evolution dimension η to the problem, the equation is rewritten as a diffusion equation:

$$
\partial_\eta \phi = \partial_{rr}^2 \phi + \partial_{\vartheta\vartheta}^2 \phi + \frac{1}{r} \partial_r \phi + L \cdot \partial_r \phi + G \cdot \partial_\vartheta \phi - \mathcal{Z} \tag{3.36}
$$

By starting with a random initial condition at $\eta = 0$ and letting the system evolve along the evolution parameter η, under properly chosen boundary conditions, the solution of Eq. (3.35) is obtained in the limit $\eta \to +\infty$. The evolution of the system may be carried on by means of standard techniques such as the relaxation, or successive over-relaxation methods [163].

Preliminary numerical investigations demonstrate that this retrieval technique is able to retrieve the phase gradient profiles, and it appears to work better for the anomalous GVD case.

However, they also underline that the dynamic range for the spatio-temporal intensity data critically affects the accuracy of the retrieval or even the convergence of the algorithm itself. This may be explained by considering the fact that, in the underlying equations, numerical derivatives of the logarithm of the intensity are involved.

Chapter 4

Third harmonic generation within a filament

In this chapter we will study the process of third harmonic generation in the filamentation regime. In particular, starting from a series of experimental results of the spectral evolution of the third harmonic component along propagation distance, performed by the Ultrafast Laser Optics group at Leibniz Universität, Hannover, we will numerically simulate the experiment, reproduce and interpret the measurements. The simulations will allow for a prediction of the evolution of the pulse temporal profile and its duration. We will determine the relative contributions of self-phase modulation and third harmonic generation in the formation of the third harmonic pulse.

Finally, we will analyze the phase profile of the generated third harmonic field, with the goal of guiding experiments for obtaining very short pulses with duration ≤ 5 fs by a proper phase compensation.

4.1 Experiments

The set of experimental measurements were performed by the Ultrafast Laser Optics group of Prof. Milutin Kovačev and Prof. Uwe Morgner at the Institute of Quantum Optics, Leibniz Universität, Hannover, Germany. 1.4 mJ pulses at central wavelength 782 nm with Fourier limit duration 27 fs were delivered by a Ti:Sa chirped pulse amplifier system (Dragon, KMLabs), operating at 3 KHz.

The pulses were then focused by a concave mirror $f = 2$ m into a gas cell filled with argon or air at given pressure. This first 1 m long high pressure cell was ended by a laser-drilled pinhole (diameter about $200 - 800$ μm) which connected the first chamber to a vacuum cell at pressure of $\sim 4 - 14$ mbar, as represented in Fig. 4.1(a).
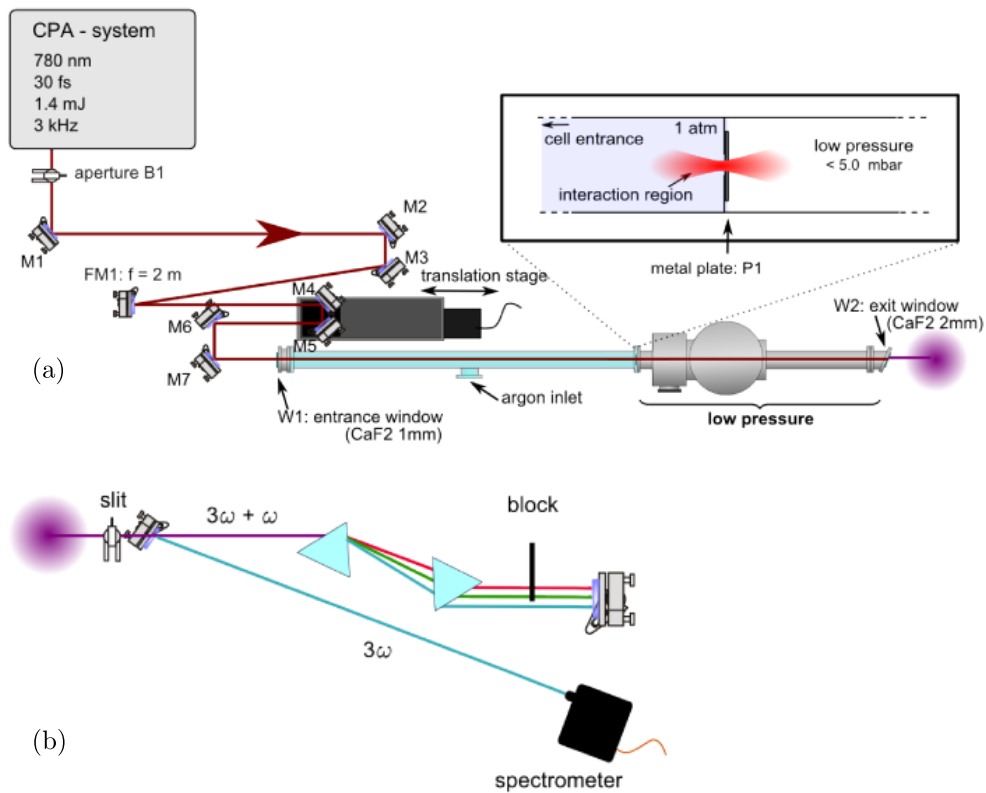
Figure 4.1: Experimental setup for the third harmonic measurements. a) Layout of the system of two chambers at different pressures. FM1 is the focus mirror; P1 is the pinhole (extraction pinhole) between the two cells. b) Setup for the spectral measurements, after propagation inside the low pressure chamber. Courtesy of D. S. Steingrube and E. Schulz.

The pulse energy after the entrance window was 0.675 mJ. After 1.25 m of propagation in the low pressure chamber, where nonlinear effects are strongly suppressed, the output beam was spatially dispersed by a set of two prisms: the fundamental beam was blocked by a razor blade and the remaining radiation was coupled into a spectrometer (AvaSpec-2048-SPU, Avantes), for spectral measurements, see Fig. 4.1(b).

The distance between the focusing mirror and the high pressure cell could be adjusted in a 30 cm range by mean of a translator stage. The beam underwent filamentation in the high pressure chamber and the translation stage allowed to longitudinally move the filament position at the extraction pinhole, where the regime abruptly stops in the low pressure cell. In this way, the filamentation process can be analyzed at different propagation distances.

Figure 4.2 shows the spectra of the third harmonic signal at different distances
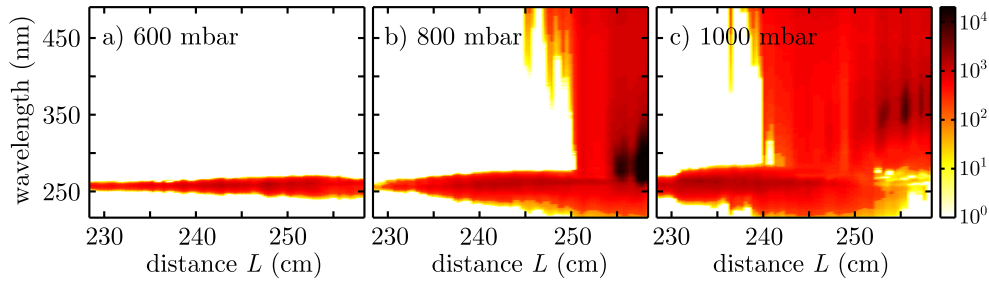
Figure 4.2: Experimental measurements of the evolution of the third harmonic signal (logarithmic plot over 4 decades) recorded by the spectrometer as a function of the distance L between the focusing mirror and the extraction pinhole. Three different pressure cases: a) 600 mbar, b) 800 mbar and c) 1000 mbar. Courtesy of D. Steingrube and E. Schulz.

L between the focusing mirror and the pinhole between the gas chamber and the low pressure cell, for three different pressure of argon: 600 mbar [Fig. 4.2(a)], 800 mbar [Fig. 4.2(b)] and 1000 mbar [Fig. 4.2(c)]. Varying the distance L between the focusing mirror and the extraction pinhole is equivalent to performing a scan over propagation distance of the filament.

At 230 cm after the mirror, the filament is truncated at the very beginning, while for increasing distance it could propagate further in the cell before truncation. The third harmonic signal ($\lambda = 261$ nm) present since the first stages is due to third harmonic generation by Kerr effect. Further in the filamentation regime, the self-phase modulation broadens the spectrum of the infrared pulse into a white-light continuum which extends up to the ultra-violet region overlapping with the initial third harmonic signal.

At lower pressure, the nonlinearity is weaker and the filament onset (nonlinear focus) is shifted to longer propagation distances. At 600 mbar [Fig. 4.2(a)], the third harmonic shows small spectral broadening.
At 1000 mbar the intensity of the third harmonic signal diminishes for large propagation distances, therefore the 800 mbar case just after the nonlinear focus seems the most promising for the synthesis of the shortest pulses by phase compensation of the spectral signal.

Figure 4.3 shows the calculated Fourier-limited pulse durations from the spectra of Fig. 4.2. The smallest Fourier-limit is 1.08 fs at 800 mbar, and 1.09 fs at 1000 mbar. By filtering this ultra-violet component and compensating for the frequency chirp in order to have flat spectral phases, one could thus obtain pulses with duration close to the optical cycle duration for the third harmonic component. However, this would require the knowledge of the spectral phase of the generated field.
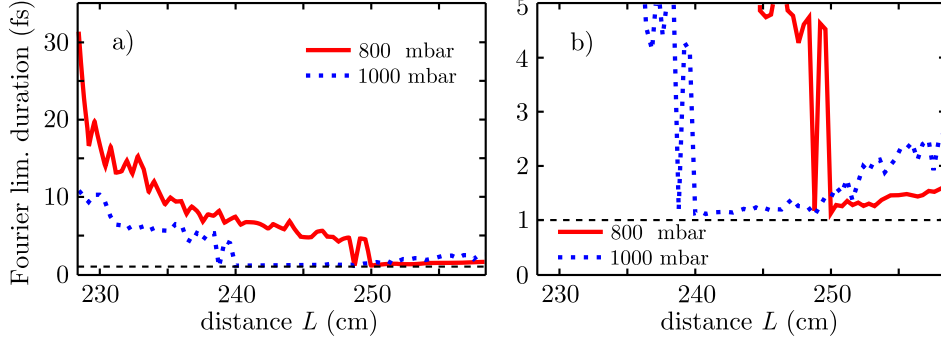
Figure 4.3: a) Fourier-limited pulse duration calculated from the spectra shown in Fig. 4.2 for the 800 and 1000 mbar cases. b) Zoom of figure a), which shows the minimum Fourier-limited duration reached in the two cases.

4.2   Numerical results

The simulations were performed by a field-resolving code based on the forward Maxwell equation, Eq. (1.18).

The propagation equations are written in the frame of the local time $\tau = t - z/v_g$ with t the time in the laboratory frame and $v_g = 1/k_0'$ the group velocity of the pulse.

The material parameters correspond to the argon gas, with dispersion relation given by a Sellmeier formulation [164] and ionization potential $U_i = 15.76$ eV. The optical Kerr effect is described by the nonlinear polarization $P_{NL}(r, \zeta, \omega) = \epsilon_0 \chi^{(3)} E^3(r, \zeta, \omega)$, where the third-order susceptibility is deduced from the measurements of Ref. [165], and corresponds to a nonlinear Kerr index coefficient $n_2 = 1.74 \times 10^{-19}$ cm^2/W at $p = 1$ atm gas pressure [166].

The nonlinear polarization comprises, as current terms, other two contributions: nonlinear losses associated with optical field ionization and plasma-induced defocusing and absorption. The electron plasma density is described by the evolution equation Eq. (1.44), with $\tau_c = 190$ fs the collision time of argon, and neglecting the avalanche contribution.

The field-dependent ionization rates $W(|E|)$ are computer with the Keldysh-PPT formulation, presented in section 1.5.6.

When changing the pressure, the refractive index is corrected by mean of the approximated Lorentz-Lorenz equation:

$$n^2 - 1 \simeq \frac{3A^{(mol)}p}{RT} \tag{4.1}$$

where $A^{(mol)}$ is the molar refractivity, $R \simeq 8.3144621$ J/(mol·K) the molar gas constant, p the gas pressure and T the absolute temperature. In this case we write:

$n(\omega, p) \simeq \sqrt{p(n^2(\omega) - 1) + 1}$, with $n(\omega)$ the refractive index at 1 atm and p the pressure in atm. Analogously, the nonlinear Kerr index is corrected as $n_2(p) = p \cdot n_2$ and the collision time as $\tau_c = \tau_c/p$, where p is expressed in atm.

The propagation equation is solved as detailed in Refs. [50, 99] by calculating the nonlinear polarization and currents in the direct domain (r, τ) at each step along the propagation axis ζ, then by temporal Fourier transforming these sources to the frequency domain and using them to propagate the frequency components of the laser pulse field to the next step by mean of a Crank-Nicolson scheme [163] along the radial coordinate, before the laser field is Fourier transformed back to the temporal domain. Dispersion is added in the frequency domain before the nonlinear propagation step.

The calculations start with a 35 fs (FWHM), 782 nm Gaussian laser pulse. The peak electric field corresponds to an initial energy of 0.675 mJ. To reproduce the experimental conditions, the pulse is positively chirped such that the Fourier limited pulse duration is 27 fs. The focusing conditions taking into account the divergence of the experimental beam, correspond to the initial distance $\zeta = 170$ cm from the focusing mirror, where this initial propagation of the pulse is evaluated with a spectral propagator.

At given ζ propagation distances inside the filament zone, the field is extracted and multiplied by a super-Gaussian function (order 6) to mimic the effect of the extraction pinhole between the high pressure and the low pressure chamber. The field is then linearly propagated in vacuum for further 125 cm and the resulting spectrum is spatially integrated over a radius of 5 mm.
This second step of propagation is based on the following approximations:

- abrupt transition between gas and vacuum;

- negligible dispersion and nonlinear effects in the low pressure stage, which is treated as vacuum.

The propagation in this case is performed by mean of a spectral code which solves Eq. (1.28) in the spectral $(k_\perp, \omega)$ domain, where $k_\perp$ is the transverse component of the wavevector in cylindrical coordinates.

Figure 4.4 shows the numerical radially integrated spectra for three different pressures of argon: 600 mbar [Fig. 4.4(a)], 800 mbar [Fig. 4.4(b)] and 1000 mbar [Fig. 4.4(c)].
By considering the initial $\zeta = 170$ cm, the nonlinear focus position roughly corresponds to the experimental position.
The green dashed lines in the figures delimit the zone where the numerical spectral profiles are qualitatively similar to the measured ones. In particular, the numerics confirm the shift of the nonlinear focus towards longer distances because of lower nonlinear effects. However, while the cases at 600 and 800 mbar are well
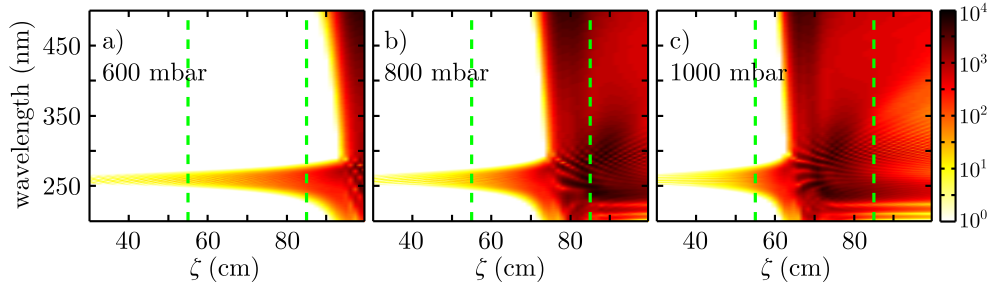
Figure 4.4: Numerical the evolution of the third harmonic signal (logarithmic plot over 4 decades) as a function of propagation distance ζ. Three different pressure cases: a) 600 mbar, b) 800 mbar and c) 1000 mbar. The green dashed lines delimit the region where the spectra are qualitatively similar to the experiments, Fig. 4.2.

reproduced, the 1000 mbar case departs from the experimental spectra at larger propagation distances (or larger distances L between the mirror and the extracting pinhole). In particular, the decrease of the third harmonic signal is not as pronounced as in experimental data.
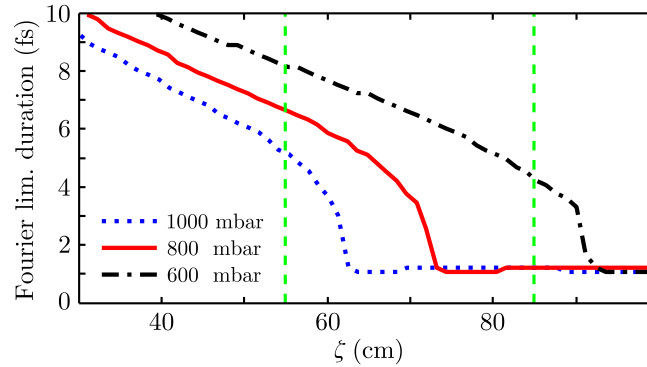
Figure 4.5: Fourier-limited pulse duration calculated from the numerical spectra of Fig. 4.4. The green dashed lines delimit the region where the spectra are qualitatively similar to the experiments, Fig. 4.2.

The Fourier limit duration obtained by considering the wavelength interval $220 \text{ nm} < \lambda < 480 \text{ nm}$ is displayed in Fig. 4.5. The results are qualitatively in agreement with the experimental data: the minimum transform-limited duration is 1.06 fs, similar to the $1.08 - 1.09$ fs from the experimental measurements. The numerics also show the trend towards larger Fourier-limited durations (~ 1.2 fs) for larger propagation distance, corresponding to the diminishing third harmonic signal. However, this increase of the Fourier-limited duration is more pronounced in the experimental data [up to ~ 2.5 fs in the 1000 mbar case, see Fig. 4.3(b)].

The numerics allow for a diagnostic of the nearfield (r, τ) distributions of the

third harmonic field and the evaluation of the spectral phase of the field, so that, after a proper compensation, the pulse could be compressed to the transform-limited duration.
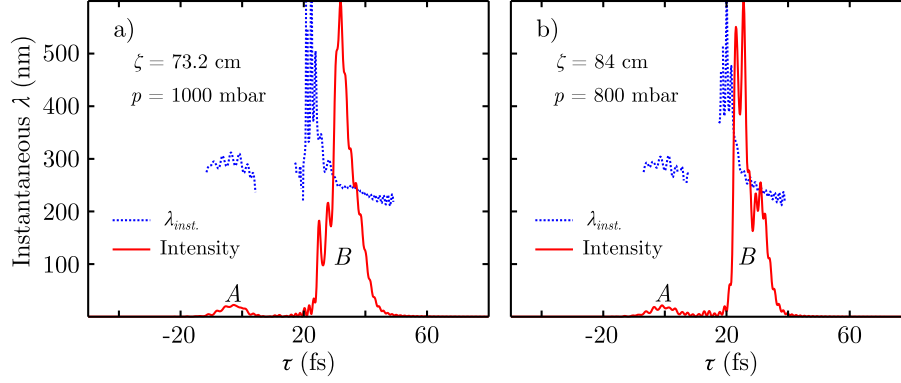
Figure 4.6: Intensity (red continuous curve) and instantaneous wavelength (blue dotted curve) for the axial component of the field after spectral filtering (considered wavelength interval: $220 \, \text{nm} < \lambda < 480 \, \text{nm}$). The intensity (arb. units) is renormalized. Cases: a) $\zeta = 73.2 \, \text{cm}$ at $p = 1000 \, \text{mbar}$, b) $\zeta = 84 \, \text{cm}$ at $p = 800 \, \text{mbar}$. A and B mark the contributions of the leading and trailing daughter peaks, respectively.

Figure 4.6(a) and 4.6(b) show the axial ($r = 0$) intensity temporal profile and instantaneous wavelength for the field when considering only the interval $220 \, \text{nm} < \lambda < 480 \, \text{nm}$, for the case: $\zeta = 73.2 \, \text{cm}$ at $p = 1000 \, \text{mbar}$ [Fig. 4.6(a)] and $\zeta = 84 \, \text{cm}$ at $p = 800 \, \text{mbar}$ [Fig. 4.6(b)]. The field is considered after the $125 \, \text{cm}$ linear propagation in vacuum.

The field in both cases is composed of two main contributions related to the daughter pulses originating in the filamentation regime: one corresponds to the leading pulse (A) and one to the trailing pulse (B), temporally delayed with respect to the first. Because of the generation of a trailing shock front [22, 167], the contribution from B is strongly blue-shifted and the instantaneous frequency reaches the third harmonic frequency.

Figure 4.7(a) and 4.7(b) show the corresponding spectral intensity and phase on axis. The green dashed curves and the black dotted curves are the fit of the phase profile with a 2nd order and 4th order power laws, respectively. The linear component of the spectral phase (related to a translation along the temporal τ axis) was subtracted in all the cases.
These fit, within a 95% confidence level, read:
$\phi_{1000}^{(2)}(\omega) = \left(3.49 \pm 0.23 \, \text{fs}^2 \right) \omega^2$
$\phi_{1000}^{(4)}(\omega) = \left(0.186 \pm 0.035 \, \text{fs}^4 \right) \omega^4 - \left(4.23 \pm 0.92 \, \text{fs}^3 \right) \omega^3 + \left(37.0 \pm 9.0 \, \text{fs}^2 \right) \omega^2$
for the $1000 \, \text{mbar}$ case, and
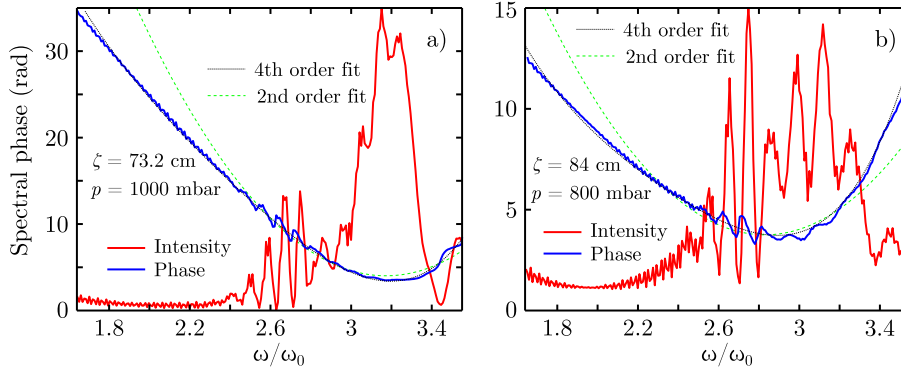
Figure 4.7: Intensity (red continuous curve) and phase (blue dotted curve; the linear component was subtracted) for the temporal spectral profile of the axial component of the field. The intensity (arb. units) is renormalized. Cases: a) $\zeta = 73.2$ cm at $p = 1000$ mbar, b) $\zeta = 84$ cm at $p = 800$ mbar. The green dashed curves and the black dotted curves are the best fit of the phase profiles with a 2nd order and a 4th order power laws, respectively.

$$\phi_{800}^{(2)}(\omega) = \left(1.62 \pm 0.10 \text{ fs}^2\right)\omega^2$$
$$\phi_{800}^{(4)}(\omega) = \left(0.133 \pm 0.022 \text{ fs}^4\right)\omega^4 - \left(2.97 \pm 0.57 \text{ fs}^3\right)\omega^3 + \left(25.5 \pm 5.5 \text{ fs}^2\right)\omega^2$$

for the 800 mbar case.

By multiplying the complex Fourier transform of the field by the phase term $\exp[-i\phi(\omega)]$ and back transforming to the temporal coordinate, Fig. 4.8 is obtained, for the 1000 mbar case: 2nd order [4.8(a)] and 4th order [4.8(b)] phase profiles, and 800 mbar case: 2nd order [4.8(c)] and 4th order [4.8(d)] phase profiles. The figures show the normalized field intensity (red continuous curve) and the instantaneous wavelength (blue dotted curve).

The compressed nearfield profiles exhibit a duration of 2.85 fs (2nd order) full width at half maximum (FWHM) and 1.6 fs FWHM (4th order) for the 1000 mbar case, and 2.07 fs FWHM (2nd order) and 1.37 fs (4th order) for the 800 mbar cases. As expected, the phase compensation with a 4th order function gives a shorter pulse. Moreover, the pulse obtained from the second order compensation exhibits a clear trailing tail of satellite peaks due to a third order spectral phase term. This suggests the possibility of a pulse with temporal Airy-like behavior, see chapter 7.

However, all the temporal profiles exhibit a precursor peak 25–30 fs before the main peak. This spurious peak is strongly suppressed for the 4th order correction, in particular for the 800 mbar case.

It is worth noting that the level of temporal compression critically depends on relative variations between the fit coefficients.

For the 1000 mbar case at $\zeta = 73.2$ cm, the total energy of the pulse after the
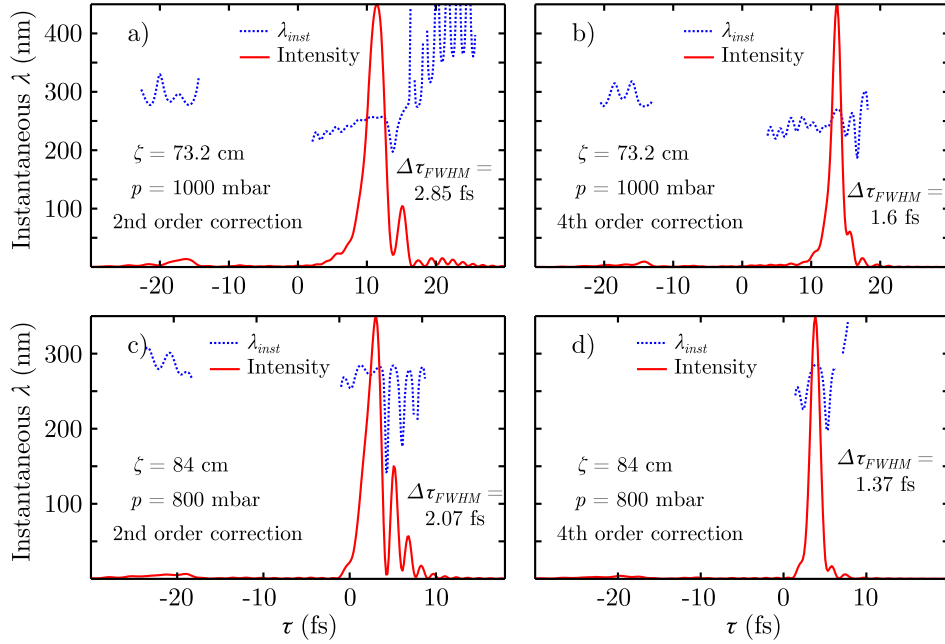
Figure 4.8: Intensity (red continuous curve; arb. units, renormalized) and instantaneous wavelength (blue dotted curve) for the temporal profiles obtained by spectral phase compensation. For case $\zeta = 73.2$ cm at $p = 1000$ mbar, a) 2nd order spectral phase, b) 4th order spectral phase. For case $\zeta = 84$ cm at $p = 800$ mbar, c) 2nd order spectral phase, d) 4th order spectral phase.

extraction pinhole is 125.7 μJ and the energy in the selected range of frequency is 8.3 μJ. For the 800 mbar case at $\zeta = 84$ cm, the total energy of the pulse after the extraction pinhole is 156.5 μJ and the energy in the selected range of frequency is 10.4 μJ. The initial energy for both cases is 0.675 mJ

In all the different cases a FWHM pulse with duration ≤ 3 fs is obtained, which becomes shorter than 2 fs for higher order compensation.
Experimental realizations would require the additional compensation of the phase term given by the spectral filter used to isolate the desired frequency interval.

4.3 Conclusions

In this chapter we analyzed the spectral evolution and the corresponding temporal profiles of the third harmonic component during filamentation in argon at various pressures. In particular, we numerically reproduced a series of experimental results obtained with cutting edge technologies.

We analyzed the temporal and spectral profiles of the ultraviolet component of the super-continuum and verified the possibility for a temporal compression of the

pulses. In particular, we studied the cases with a second-order and a fourth-order phase compensation.

We verified the possibility for compression to durations shorter than 3 fs.

The development of ultrashort pulses in the deep ultraviolet ($\lambda < 300$ nm) region has for example applications in time-domain studies of the electron dynamics in the valence shell of molecules and solids, in processes of chemical and biological interest [168–171].

Ultrashort pulses in the deep ultraviolet have been generated by spectral broadening and compression of ultraviolet pulses [172], direct third harmonic generation from multi-cycle [173] or few-cycle [174, 175] infrared pulses, and optical parametric amplification in gas-filled capillary waveguides [176] or in a filament [177].

The ultraviolet component of the super-continuum from a filament in argon generated by a 12 fs pump pulse in the infrared (obtained with an initial stage of spectral broadening by self-phase modulation and compression) has been demonstrated to be compressed to sub-30-fs [178] or sub-10-fs [179] pulses. Theoretical and experimental work on short-range filamentation ($\lesssim 3$ mm) form near single-cycle infrared pulses in gas at high pressure have shown the possibility of compression to sub-fs ultraviolet pulses [180].

The preliminary experimental results and the numerical work presented in this chapter pave the way for the generation of ultrashort pulses in the ultraviolet region with a similar procedure, but avoiding a first initial stage of 12-3 fs infrared pulse generation by the control of focusing conditions and the tuning of the gas pressure. Indeed, these results show that appreciable spectral broadening up to the third harmonic is possible with longer pulses. Furthermore, long-scale filaments permit the use of relatively low gas pressure.

Future development of this work will involve the experimental temporal characterization of the third harmonic component and possibly the compression of this ultraviolet component by phase compensation. Because of the strong spatio-temporal coupling arising from the filamentation process, different spectral phase compensations along the radial coordinate may be required, as shown for the generation of ultrashort pulses from the continuum in the near infrared-visible region [181]. This topic will deserve further investigation both from the experimental and the numerical point of view.

Chapter 5

High harmonic generation and carrier-envelope shearing

In this chapter we will perform a numerical study of the strongly nonlinear phenomenon of high harmonic generation (HHG) by spatio-temporally coupled wavepackets: conical wavepackets (CWPs), described in section 2.3.
We will show that, due to the characteristic features of CWPs, the process of HHG, for very short pulses, is strongly influenced by envelope velocity related effects. In particular, we will perform a deep numerical analysis on the selection of different quantum path contributions associated to the generation of isolated attosecond pulses. We will show the importance in this case of the instantaneous variation of the local intensity of the pump field, i.e. the variation of the carrier-to-envelope phase in propagation due to different phase and envelope velocities.

The analysis of the main effects and the interpretation of the numerical results presented in this chapter were performed in collaboration with Prof. Mette B. Gaarde of the Department of Physics and Astronomy, Louisiana State University, Baton Rouge, Louisiana (U.S.A.).

5.1   Numerical model

The simulations were performed by means of Eq. (1.18), in cylindrical symmetry, considering argon as the propagation medium and an input pulse centered at wavelength $\lambda_0 = 800$ nm. The electric field was divided into two components: *pump* and *harmonic field*, depending on whether $\omega < 10\omega_0$ or $\omega > 10\omega_0$, and accordingly modeling the nonlinear polarization.

For the pump laser pulse the nonlinear polarization comprised the optical Kerr effect and plasma effects, modeled as a current term.
The Kerr response was included through the complex counterpart of the nonlinear

polarization $P_{\mathrm{Kerr}} = \epsilon_0 \chi^{(3)} E^3(r, \zeta, \tau)$, with a third-order susceptibility $\chi^{(3)}$ value deduced from the measurements of Ref. [165], namely $n_2 = 1.74 \times 10^{-19}$ cm^2/W, at 1 atm pressure.

The plasma current comprised two parts: nonlinear losses (see section 1.5.2) and plasma induced defocusing and dispersion (see section 1.5.3).

Nonlinear losses were accounted for by the complex current:

$$\mathcal{J} = \frac{W(|E|^2)}{|E|^2} U_i n_0 \epsilon_0 c (\rho_0 - \rho) \mathcal{E}$$

where $W(|E|^2)$ is the field-dependent ionization rate and U_i the ionization potential. Ionization was described by an evolution equation for the density of neutral argon atoms

$$\partial_\tau \left[\rho_0 - \rho(r, \zeta, \tau) \right] = -W(|E|^2) \left[\rho_0 - \rho(r, \zeta, \tau) \right]$$

in which ρ represents the density of electrons generated by optical field ionization. Defocusing and dispersion from the generated plasma were accounted for by mean of Eq. (1.40), with $\sigma(\omega) \simeq i\Im \{\sigma(\omega)\}$ (plasma absorption was neglected, $\omega_0 \tau_c \gg 1$).

The ionization rates were derived by mean of the Keldysh-PPT formulation, as described in section 1.5.6.

Dispersion of the pump field was calculated with the formula given in Ref. [164]. The Kerr coefficient, the collision time, the neutral density and the material dispersion were corrected to take into account the pressure p of the gas, as described in the previous chapter.

For the harmonic field, the nonlinear polarization was obtained from the time-dependent dipole moment, calculated using the *strong field approximation* (SFA, section 1.6.2) multiplied by the density of neutral atoms. Its implementation strictly followed Ref. [50].

Dispersion and linear absorption were computed from the interpolation of the values taken from the database of the Lawrence Berkeley National Laboratory's Center for X-Ray Optics (CXRO), [182]. The CXRO website gives the atomic scattering factor f_1, f_2 as a function of wavelength for the desired material; the corresponding complex refractive index (where the imaginary part corresponds to absorption) is:

$$n = 1 - \frac{2\pi c^2}{\omega^2} \rho_0 r_e \left[f_1(\omega) + i f_2(\omega) \right] \tag{5.1}$$

where $r_e = e^2/(4\pi\epsilon_0 m_e c^2) \simeq 2.817940 \times 10^{-13}$ cm is the classical electron radius.

5.2   Numerical simulations

A series of simulations were launched by assuming initial pump pulses in the shape of finite-energy conical wavepackets (CWPs) (see section 2.3).
The temporal profiles were Gaussian profiles with 5 fs full width at half maximum (FWHM) duration and peak electric field corresponding to an initial cycle-averaged intensity of $I_0 = 2.7 \times 10^{14}$ W/cm^2. The CWPs were apodized by a spatial Gaussian function, with $w_0 = 0.68$ mm.

Three particular cases of CWPs were considered, corresponding to three different values of the tilt angle δ for a given propagation angle θ_0: a pulsed Bessel beam (PBB), a Bessel X-pulse (BXP) and a third CWP featuring $\delta = +\theta_0$. In particular, as described in detail in section 2.3, the plane-wave constituents of the PBB exhibit equal transverse k-vector (tilt angle $\delta = -\theta_0$) [66, 72], whilst in the BXP case equal propagation angle for each frequency ($\delta = 0$) [78].
From Eqs. (2.6) and (2.7), the PBB thus exhibits an envelope velocity smaller than its phase velocity $v < v_p$. In the BXP case, since the gas at low pressure is very weakly dispersive, these velocities are almost equal, $v \simeq v_p$. The third CWP case featured $\delta = +\theta_0$, in order to have a conical wavepacket with envelope velocity larger than the corresponding phase velocity $v > v_p$; in such sense we called this wavepacket "superluminal" pulse (SLP).
All the three CWPs present the same phase velocity $v_p = \omega_0/(k_0 \cos\theta_0)$, since the same cone angle $\theta_0 = 0.44°$ was used. This angle was chosen by scanning over different angle values to optimize the effects described in the following sections.

The propagation was simulated in a 1.3 cm cell filled with argon at pressure $p = 100$ mbar. The starting position $\zeta = 0$ was the center of the Bessel zone for the CWPs.

To date, SLP-like pulses have never been experimentally generated, but CWPs with peak velocity larger than their phase velocity have been shown to appear spontaneously during the filamentation of ultrashort pulses in Kerr media [96] (see section 2.5).

HHG by mean of PBBs may be obtained in an appropriate hollow-core fiber [58]. The modes of these fibers are precisely PBBs, as shown in section 1.6.3, and the fundamental-mode cone angle is related to the fiber inner radius a_0 by $a_0 = 2.4048c/(\omega_0 \sin\theta_0)$ [55]. A $0.44°$ cone angle may thus be obtained with an 80 μm diameter fiber. In this case, however, calculations should be corrected by taking into account the modifications induced by the fiber geometry with respect to the free-space geometry, such as a slightly modified v, linear losses and dispersion.

5.3   Carrier-envelope shearing

A dominant factor in determining the temporal profile of the generated harmonic field for the case of very short laser pulses is the initial carrier-to-envelope phase (CEP), i.e. the relative shift between the maximum of the real electric field and that of the envelope, because the HHG process is highly sensitive to the phase of the pump field.

The initial CEP is thus expected to play a relevant role in the HHG process, for both the temporal profile of the generated field and its spectral content, in particular for pulses in which phase and group velocity are very close to each other (as the Gaussian pulse case).

Since for a BXP the CEP varies little during propagation ($v \simeq v_p$), such consideration, i.e. a strong dependence of the emitted field on the initial CEP, is expected to be valid also in this case.
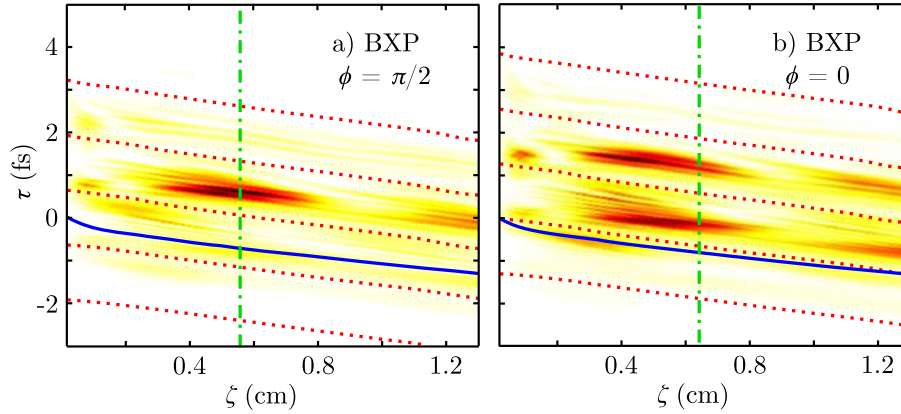
Figure 5.1: Axial temporal profile (linear scale) of the intensity of the harmonic field versus propagation distance ζ for the BXP case. Initial CEP: (a) $\phi = \pi/2$ rad and (b) $\phi = 0$ rad. The harmonic field was synthesized with no further spectral filtering other than a high-pass filter $\omega > 10\omega_0$. The solid blue curves and the dashed red curves show the propagation of the center of mass (envelope peak) and the positions of squared field maxima for the pump infrared pulse, respectively. The vertical green dashed-dotted lines mark the ζ positions chosen for the analysis of Fig. 5.3.

Figures 5.1(a) and 5.1(b) show the evolution of the temporal intensity profile for the axial component ($r = 0$) of the harmonic field as a function of the propagation distance, for two different values of the initial CEP, $\phi = \pi/2$ rad and $\phi = 0$ rad, respectively, in the BXP case.

The solid blue curves mark the temporal evolution of the envelope peak of the driving pulse; its slope is thus given by $1/v(\zeta) - 1/v_g$, since the simulations were performed in the reference system moving at the Gaussian pulse group velocity

$v_g = 1/k_0'$. The red dashed curves of slope $1/v_p(\zeta) - 1/v_g$ mark the peaks of the driving field (maxima and minima), which travel at the phase velocity $v_p(\zeta)$. In general envelope and phase velocity will not be constant as in the ideal infinite-energy BXP case, because of effects related to plasma generation, such as the defocusing of the trailing portion of the pulse therefore shifting the position of the center of mass of the envelope, and small corrections related to the Gaussian apodization [183]. Notwithstanding these small corrections, the slopes of dashed and continuous curves are in agreement with the BXP property $v \simeq v_p$.

The figures show a series of distinct extrema for the harmonic field intensity along the temporal coordinate with durations of a few hundreds of as, which follow with almost constant temporal delay the peaks of the pump field during propagation. Each of these extrema corresponds to an harmonic burst approximatively centered around the return time position of the cut-off trajectory [section 1.6.2]. These harmonic bursts exhibit intensity oscillations along the propagation distance ζ, which are related to phase matching properties for the HHG process [section 1.6.3]. Indeed, a given phase mismatch Δk implies an intensity modulation along propagation distance of the harmonic field, with periodicity inversely proportional to the value of Δk.

The harmonic field was not further filtered other than the $\omega > 10\omega_0$ high-pass filter.

An almost isolated temporal peak in the harmonic field is generated for the $\phi = \pi/2$ case, and the ratio between the second most intense peak and this main peak reaches the lowest value of 25% at $\zeta = 0.56$ cm, with a corresponding FWHM duration of 340 as.

This isolated peak generation may be explained in terms of *ionization gating*, which in this case works mainly through the space- and time-dependent plasma dispersion term.
The plasma refractive index causes a reshaping of the laser beam by advancing the peak of the laser pulse on axis, which effectively shortens the intense part of the pulse [184]. More importantly, the plasma contribution to the phase mismatch is time-dependent which means that the phase matching conditions change from one half-cycle of the laser field to the next [185, 186].
This leads, in the $\phi = \pi/2$ case, to good phase matching predominantly during one half-cycle of the driving field, whereas in the $\phi = 0$ case there are two half-cycles in which the harmonic radiation is phase matched, which leads to two attosecond bursts. These two bursts exhibit different time-frequency characteristics both in terms of their cut-off energy and in terms of the dominant quantum path contributions [see Fig. 5.3(a) in the next section], consistent with a rapidly changing phase mismatch [186].
The PBB and SLP may be expected to be different from the BXP case, since in

these two cases $v \neq v_p$. In particular, the harmonic profiles may be expected not to crucially depend on the initial CEP of the pulse, since the CEP of these pulses varies along the propagation distance ζ. Therefore, at a certain distance ζ in propagation, the optimal CEP for isolated pulse generation will then be encountered, even when starting from a non-optimal initial pump phase.
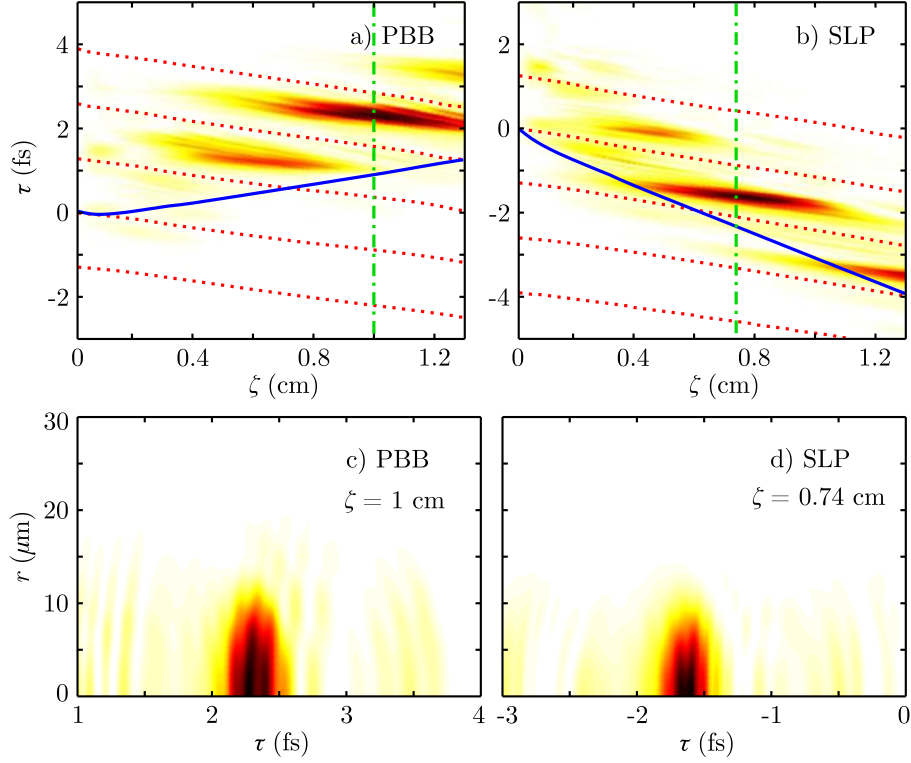
Figure 5.2: Axial temporal profile (linear scale) of the intensity of the harmonic field versus propagation distance ζ for the (a) PBB and (b) SLP cases. The harmonic field were synthesized with all the frequency contributions $\omega > 10\omega_0$. The solid blue curves and the dashed curves mark the propagation of the center of mass (envelope peak) of the driving infrared pulse and the positions of its squared field maxima, respectively. The vertical green dashed-dotted lines mark the ζ positions of best contrast between the main peak and the second most intense one. (c) and (d) show the nearfield (r, τ) intensity profile of the harmonic field (linear scale) for the PBB and the SLP case at the distance marked by the green dashed-dotted lines of (a) and (b), respectively.

Figures 5.2(a) and 5.2(b) show the (ζ, τ)-evolution of the intensity profile for the axial component ($r = 0$) of the harmonic field, analogous to Fig. 5.1, for the PBB and SLP cases, respectively. The initial CEP was 0 rad for both cases. As in the BXP case, the slopes of the dashed and continuous curves (related to the pump field local phase and envelope velocities, respectively) are in agreement

with the predictions of Eqs. (2.6) and (2.7) for the propagation of linear, non-apodized CWPs. In particular, the figures clearly show that although the phase velocity is the same for the BXP and these two cases, the envelope velocity (represented by the continuous blue curve) is larger or smaller than v_p for the SLP and PBB, respectively.

The mismatch between phase and envelope velocities determines during propagation a shift of the position of the envelope maximum, which effectively moves with respect to the carrier-wave propagation.
This effect gradually modifies the intensities of the field maxima and accordingly the related HHG process. The harmonic field is still generated along iso-phase curves of the pump field in the (ζ, τ) space, as in the BXP case [Fig. 5.1(a) and 5.1(b)]. The shift of the pump envelope induces a "shear" in the harmonic peak, which is negative (delayed, towards more positive times) for the PBB case and positive (advanced, towards more negative times) for the SLP. The harmonic field still exhibits intensity oscillations along ζ, but these are displaced following the effective motion of the pump envelope velocity. In the BXP case this phenomenon cannot be observed because of (almost) equal phase and envelope velocities.

This shearing effect continuously modifies the CEP of the pump wavepacket. At a certain ζ position, different for the two cases, it reduces to the optimal parameter for the generation of an almost isolated temporal peak in the harmonic field, similarly to Fig. 5.1(a).
In particular, from the simulations a 350–400 as (FWHM) pulse for the PBB case is observed between $\zeta = 0.9$ cm and $\zeta = 1.2$ cm. The ratio of the second highest peak to the intensity of the main peak is below 35% and the minimum ratio is 16% around $\zeta = 1$ cm, with a corresponding duration (FWHM) of 350 as. As in the BXP case, this result was obtained without any spectral filtering on the harmonic field except for the high-pass filter at $10\omega_0$, mimicking the action of an Aluminum filter, frequently used in experiments to separate the laser light from the harmonic light.
A 300–320 as pulse is obtained for the SLP case between $\zeta = 0.65$ cm and $\zeta = 0.9$ cm, with contrast below 35%, which reaches a minimum of 13.5% at $\zeta = 0.74$ cm, with a corresponding duration of 300 as.
The radial profiles of the harmonic field intensity in the PBB and SLP cases are shown in Figs. 5.2(c) and 5.2(d), respectively, highlighting the smooth spatio-temporal profiles of the harmonic pulses that are spatially confined on axis within a 20 μm radius, roughly corresponding to the most intense part of the pump field. The total attosecond pulse energies [obtained by integration over the whole (r, τ) space] are 23 pJ and 8 pJ for the PBB and SLP cases, respectively.

5.4   Quantum trajectory contributions

To further investigate the role of this effective shearing effect on HHG and the related phase matching properties, the time-frequency dependence [187] of the harmonic field at the point of best contrast was evaluated for the different cases. Figure 5.3 shows (in logarithmic scale over 2 decades) the frequency-resolved spectral analysis (FROG) [156] for the axial ($r = 0$) harmonic field in the cases: (a) BXP with initial CEP $\phi = 0$ rad, (b) BXP with $\phi = \pi/2$ rad, (c) PBB, and (d) SLP, at the ζ positions marked by the dashed-dotted lines in Figs. 5.1 and 5.2. The dashed curves represent the axial intensity profiles of the harmonic field.

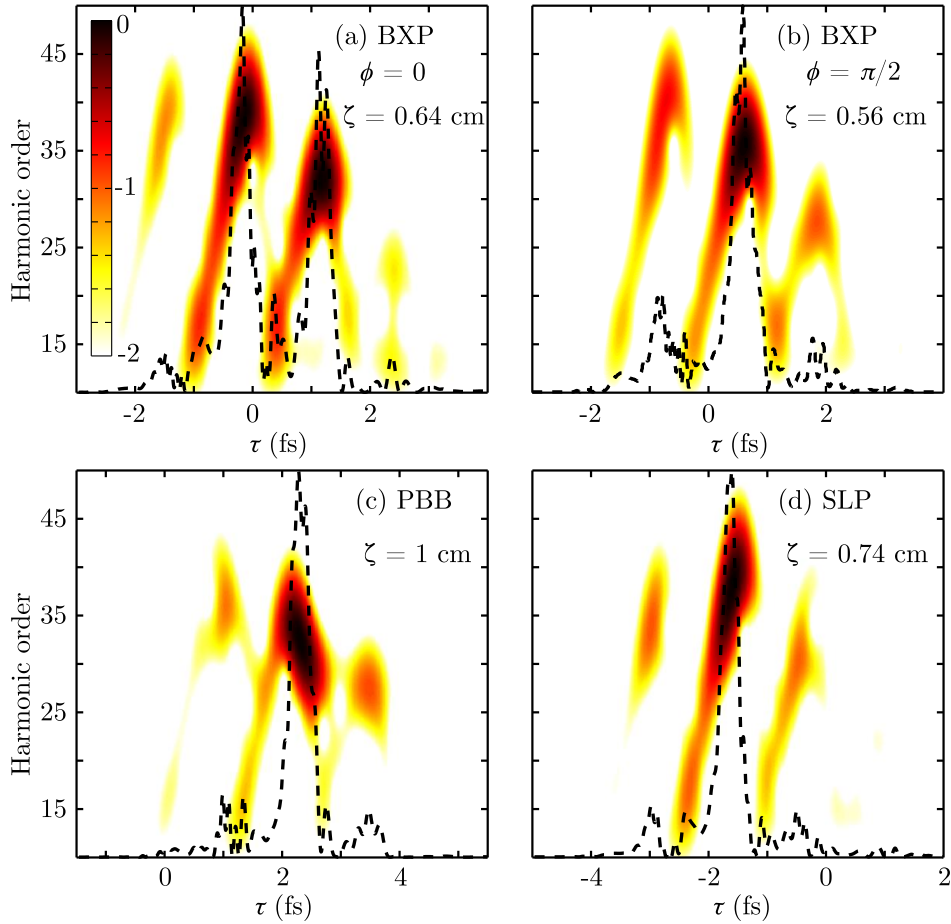**Figure 5.3:** Temporal gated spectral analysis of the axial component of the harmonic field (logarithmic scale over two decades) at given propagation distance: (a) BXP ($\phi = 0$ rad) at $\zeta = 0.64$ cm, (b) BXP ($\phi = \pi/2$ rad) at $\zeta = 0.56$ cm, (c) PBB at $\zeta = 1$ cm, (d) SLP at $\zeta = 0.74$ cm. The dashed curves represent the temporal intensity profile of the harmonic field.

The FROG analysis were performed by numerically gating the harmonic field with a very short Gaussian function of duration $T_p = 0.2$ fs and performing a Fourier transform of the resulting field.

Figure 5.3 shows the typical characteristics of harmonic emission. The harmonic burst is chirped; in particular, as represented by the semi-classical model, it exhibits chirp of two opposite signs, corresponding to the two main quantum paths: short and long trajectories.

Indeed, the same harmonic frequency is present at two different temporal positions according to the different recombination times of the two trajectories (see section 1.6.2). The time-gated spectral analysis thus shows a spectral intensity in the form of a downside-up "V". The "vertex" corresponds to the cut-off frequency; the front tail (rising tail) is the short path contribution, while the trailing tail (descending tail) is the long trajectory contribution.

The shearing effect not only affects the temporal profile of the harmonic field, but also acts as a gating mechanism in the spectral domain.

In particular, in the BXP case [Fig. 5.3(a) and 5.3(b)] the main portion of the spectrum associated to the temporal intensity peaks falls in the region around the cut-off frequency (the vertex of the "V"). These regions come from both short- and long-path contributions [50].

In the PBB and SLP case [Fig. 5.3(c) and 5.3(d), respectively] the main contributions come from regions near the cut-off, which can be identified as corresponding to long quantum trajectories for the PBB case and short trajectories for the SLP case.
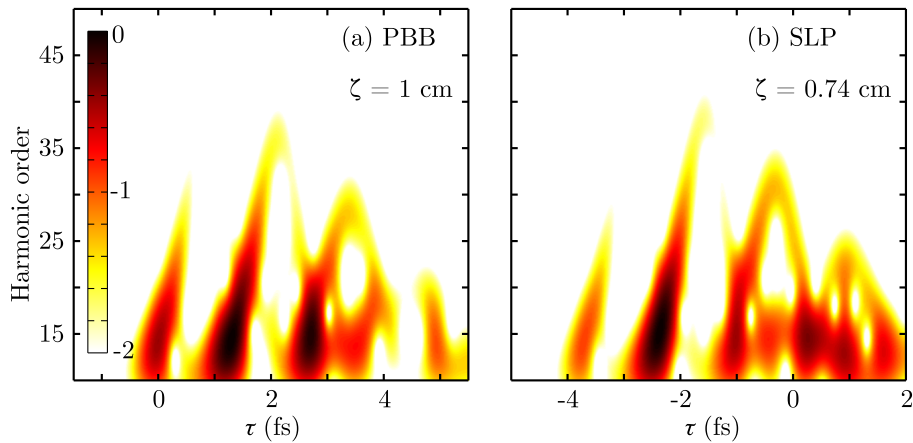

Figure 5.4: Temporal gated spectral analysis of the axial component of the nonlinear polarization (logarithmic scale over two decades) for the cases: (a) PBB at $\zeta = 1$ cm, (b) SLP at $\zeta = 0.74$ cm.

This effect is a propagation effect. Indeed, Fig. 5.4(a) and 5.4(b) show the

FROG analysis (logarithmic scale over 2 decades) of the axial component of the nonlinear polarization, evaluated with the SFA, at the same propagation distances of Figs. 5.3(c) and 5.3(d) for the PBB and SLP cases, respectively. The nonlinear polarization is the source term in the generation of the harmonic field. The instantaneous component of the harmonic field which coherently sums with the previously generated field is proportional to this term. In both cases, the main contribution is related to short trajectories and lower frequencies. The effect of Fig. 5.3 is therefore a propagation effect related to phase matching.

The selection of the quantum trajectories contributions may be qualitatively explained by considering the evolution along propagation ζ of the instantaneous intensity (squared electric field) maxima of the driving field in the different cases, shown in Fig. 5.5.

In particular, for the SLP case around $\zeta = 0.74$ cm, the intensity of the pump field carrier peak corresponding to the harmonic burst associated to the isolated pulse is increasing versus propagation distance ζ (blue dashed curve).

In the PBB case, around $\zeta = 1$ cm, the value of the field peak is locally decreasing (black continuous curve).
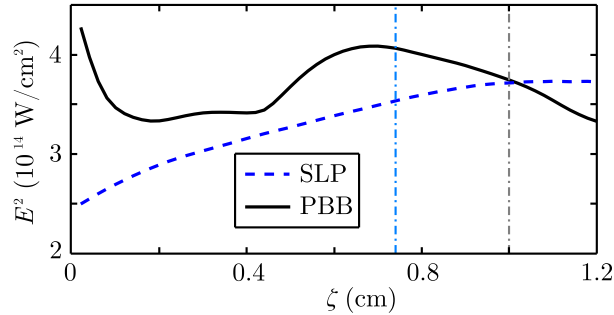
Figure 5.5: Evolution along propagation distance ζ of the instantaneous value of the squared electric field peak of the pump corresponding to the harmonic burst associated to the isolated pulse. Black continuous curve: PBB case. Blue dashed curve: SLP case. The vertical dashed-dotted lines mark the propagation distances under examination ($\zeta = 1$ cm for the PBB; $\zeta = 0.74$ cm for the SLP).

This effect determines different signs for the dipole phase contribution term in the two cases [188], since this term linearly depends on the field intensity [section 1.6.3].

By adopting the sign convention of [50], each contribution to the phase matching for the harmonic field generation may be isolated.

- The geometric term is always positive for both PBB and SLP, since the effective pump wavevector on axis is shortened in CWPs, see section 1.6.3

and Refs. [59, 60, 189].

- The plasma contribution is positive and similar for both cases, as shown in Fig. 5.6 by the temporal profiles of the axial ($r = 0$) plasma density.

- The dipole term depends on the gradient along ζ of the instantaneous intensity and thus it is negative for the PBB and positive for the SLP pulses, Fig. 5.5.

In both cases, the absolute value of the dipole contribution will be small and close to zero for short trajectories and large for the long trajectories [42, 190]. Therefore, the large positive Δk contribution from the first terms in the PBB case may be compensated or partially compensated for by the large negative dipole contribution from the long trajectories.

On the other hand, in the SLP case, all the contributions are positive and the minimum Δk is obtained for the smallest possible dipole term, i.e. the short trajectory term.
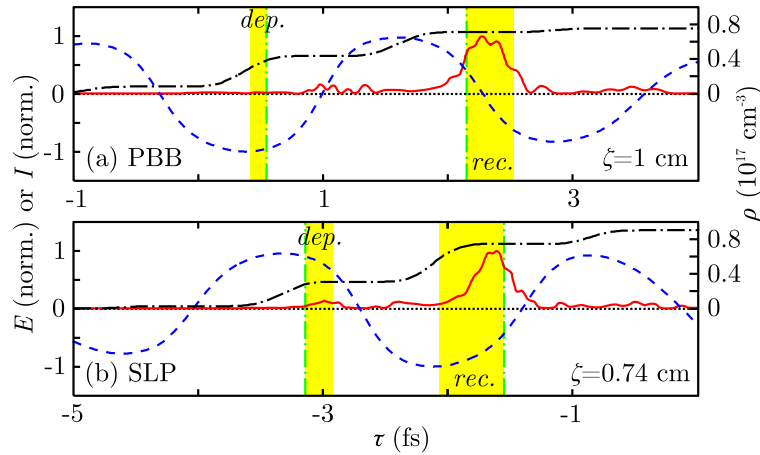
Figure 5.6: Blue dashed curve: electric field of the pump (normalized; left axis); red continuous curve: intensity of the harmonic field (normalized; left axis); black dashed-dotted curve: plasma density (right axis), at $r = 0$ versus local time τ for (a) PBB at $\zeta = 1$ cm and (b) SLP at $\zeta = 0.74$ cm. The yellow areas represent the departure (*dep.*) and recollision (*rec.*) times for the electrons in the two cases assuming the classical approach, for long (a) and short (b) trajectories. The vertical green dashed-dotted lines refer to the trajectories with return energy corresponding to the cut-off.

Moreover, Fig. 5.6 confirms, by mean of the classical approach, the main contribution of long trajectories for the PBB case since the typical recollision times for this quantum path contribution [*rec.* yellow area in Fig. 5.6(a)] correspond to the harmonic intensity peaks. Analogous considerations can be drawn for the short trajectories contributions in the SLP case [*rec.* yellow area in Fig. 5.6(b)].

5.5   Conclusions

In this chapter, we have studied HHG with ultrashort CWPs. In particular, we investigated the role of the envelope velocity in the temporal and spectral content of the emitted harmonic radiation. For very short pulses (5 fs wavepackets), we identified two main results:

- A shearing effect in the temporal domain: harmonic bursts are related to the phase of the pump field, thus their emission follows iso-phase curves; on the other hand, the CEP constantly varies, determining a later shift of the peak envelope of harmonic maxima (related to phase matching) along the propagation direction. This locally leads to the selection of almost isolated attosecond pulses.

- The selection of different quantum path contributions: the variation of the local intensity due to the difference between phase and envelope velocities determines different phase matching contributions. In particular, the cases $v < v_p$ and $v > v_p$ determine an enhancement of the contribution from long or short quantum trajectories around the cutoff, respectively.

These effects are most evident for very short pulses (less than 3 optical cycles) due to the fact that they rely on the instantaneous variation of the local intensity of the pump field, i.e. on the variation of the CEP in propagation.
Given the phase-matching nature of the process, for a given gas and gas pressure, there is an optimal value of the Bessel cone-angle that achieves isolated pulse generation, which was found by scanning over different angle values. In an experimental framework it would be easier to scan over the gas pressure.

The selection of the quantum path contribution enables a tuning of the temporal and spatial characteristics of the emitted harmonic field [45, 46, 48].

Possible experimental realization of the numerics presented in this chapter may rely on the fact that hollow-core fiber modes are truncated PBBs. However, this would require corrections due to the modifications induced by the fiber geometry with respect to the free-space geometry (slightly different envelope velocity v, linear losses and dispersion).
CWPs from a filament may also be regarded as candidates for experimental realizations. Indeed, HHG directly from a filament has been demonstrated both from theoretical and experimental results [57, 191–193]. The peak envelope velocities of the daughter pulses may be tuned by changing the pump pulse initial parameters. Numerical simulations can be performed to define the best scenario for HHG in filamentation, by controlling the temporal shape and propagation properties of these daughter peaks.

Ultraviolet and soft X-ray attosecond pulses from HHG are used as probes for time-resolved studies of ultrafast dynamics of electronic wavepackets in various physical systems [7, 8], such as molecular orbital reconstruction [194], real time observation of valence electrons motions [195], atomic inner-shell spectroscopy [196], measuring photoelectron ejection from surfaces [197].

Chapter 6

Quantum trajectories interference in HHG

In this chapter we will study the spatio-temporal profile of low-order harmonics generated in gas in a semi-infinite gas-cell configuration with a Gaussian pulse.

In particular, we will numerically reproduce a series of experimental results of HHG obtained by the Attoscience and Ultrafast Optics group at the Institut de Ciències Fotòniques of Barcelona. These measurements show the generation of a ring structure in the spatio-temporal farfield (wavelength and propagation angles) intensity distribution of low order harmonics from HHG in argon. Based on the numerical results, this pattern will be interpreted as the interference between different quantum trajectory contributions. The quantum path interferences, first observed in 2008 [198–200], offer insight into the interplay between the microscopic and macroscopic (related to phase matching properties) responses of the HHG process.

We will show that in this particular case, contrary to the case described in the previous chapter, the process is dominated by the instantaneous response of the medium because of the high absorption corresponding to the wavelength under examination.

6.1   Measurements

The experimental measurements were performed by the Attoscience and Ultrafast Optics group of Prof. Jens Biegert at the Institut de Ciències Fotòniques (ICFO), Castelldefels (Barcelona), Spain.

The setup is represented in Fig. 6.1. The input laser beam was a 30 fs pulse (not shot-to-shot CEP stabilized) at wavelength 800 nm, 5 KHz repetition rate, delivered by an amplified Ti:Sapphire system (Red Dragon Laser, KM Labs, Boul-
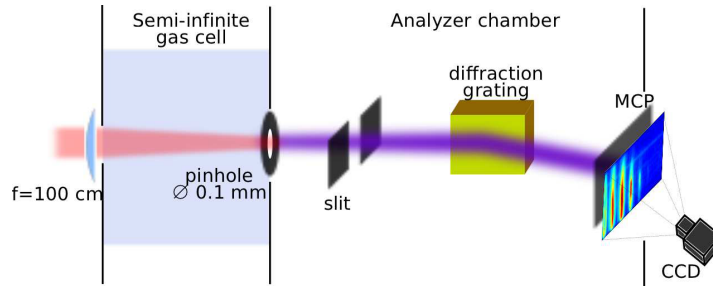
Figure 6.1: Representation of the experimental setup, described in the text. Courtesy of S. M. Teichmann.

der, Colorado, USA). The pump beam was focused by a $f = 100$ cm focusing mirror into a 1 m long cell filled with argon at 75 mbar pressure, terminating with a 100 μm diameter pinhole which separates the gas chamber from the vacuum chambers. The focal position of the beam was about 1 cm from the pinhole.

The field passed through the pinhole and, after an Aluminum filter which blocked the infrared radiation, propagated into the (spatial) farfield finally impinging onto a vertical slit and a reflective grating (1000 lines/mm, Hitachi), which spatially separated the different frequency components.

The resulting intensity distributions, featuring propagation angles along the vertical coordinate and temporal frequencies along the horizontal, was then recorded by the combination of a micro-channel plate (MCP, Hamamatsu) with a fluorescent back screen and a CCD camera.
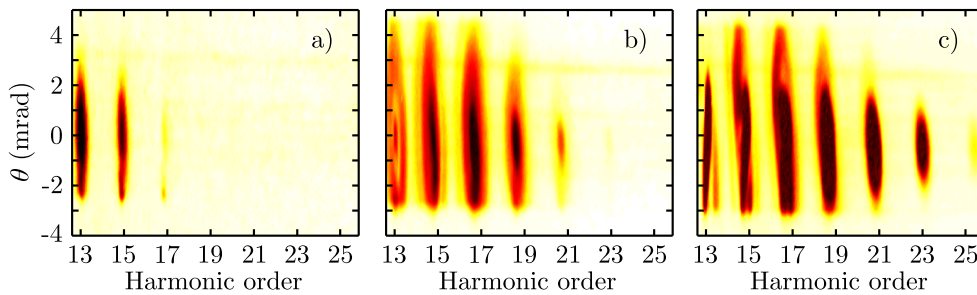
Figure 6.2: Spectrally resolved (propagation angle and harmonic order) HHG measurements in argon at 75 mbar for three pulse energy cases: (a) 400 μJ, (b) 600 μJ, and (c) 1 mJ. The 13th harmonic signal in case (b) clearly exhibits a ring structure around a central core.

Figure 6.2(a), 6.2(b) and 6.2(c) show the spectral angle-harmonic order intensity distributions for the generated field for three different energy cases: 400 μJ, 600 μJ and 1000 μJ. As predicted by the cut-off law, Eq. (1.57), the highest measured harmonic order increases with the intensity of the field.

In particular, in Fig. 6.2(b), the 13th harmonic exhibits a clear ring structure around a central peak. With increasing energy, Fig. 6.2(c), the spectra becomes asymmetric and the ring shape is lost.
Similarly to the spectral distribution, the nearfield (r, τ) intensity distribution for the 13th harmonic of case (b) is expected to feature a concentric ring structure.

This behavior may be understood in terms of *quantum path interference* [198, 200].
As explained in section 1.6.2, the main contribution at a given frequency ω_q in the harmonic spectrum comes from two different electron trajectory contributions, namely short and long quantum trajectories.
The phase of this quantum contributions is directly proportional to the intensity of the wavepacket, with different coefficients for the two quantum paths. In particular, the phase associated to the long trajectories varies faster than the one associated to the short trajectories.

The superposition of these two contributions, when their relative amplitudes are similar, is expected to generate an interference pattern along both the temporal and the spatial domain. At given propagation distance ζ, the intensity of the pump field changes along the temporal and the transverse spatial coordinate: the locally generated harmonic field will then exhibit a ring pattern corresponding to the interference of short and long contributions along both coordinates.

The locally generated interference is expected to be observed in the output field if the absorption length is shorter than the coherence length for the harmonic field at a given frequency, so that the contribution from the previously generated field is strongly suppressed.

The asymmetry in the structures measured at higher energy is due to the increase of the free electron plasma density [201], which mainly affects the trailing part of the pulse.

Usually, HHG experiments are performed by focusing the laser beam on a gas jet and this interference pattern is difficult to observe since the spatial and temporal dependence of the harmonic phase smears out the interferences in the macroscopic response, and other effects, such as, for example, the shot-to-shot change of laser focus position because of pointing instability, tend to wash out the interference pattern when averaging the intensity profiles.
In order to observe quantum path interference, a series of technical steps are usually taken to minimize the smearing effect: for example, a farfield spectral filtering is used to isolate a portion of the emitted harmonic field. Since long trajectories have a stronger divergence, an off-axis window is able to stop most of the short trajectories component so that in the measured field both quantum path terms have approximatively the same weight and the interference pattern is enhanced [198, 202].
The experiments show that in this particular case quantum trajectories interference

could be observed even without the need of spatial filtering.

6.2   Numerical simulations

We performed a series of numerical simulations to interpret the experimental results.

The numerical model and code were the same as that used for the simulations of chapter 5. In particular, the pump at central frequency ω_0 and the harmonic field were propagated by a carrier-resolving code in cylindrical symmetry. The component of the field at frequencies $0.25 < (\omega/\omega_0) < 7$ were chosen as the pump field, while the harmonic field was considered for $\omega > 10\omega_0$.
The nonlinear polarization included:

- Kerr response, nonlinear losses based on Keldysh-PPT ionization rates, and plasma-induced defocusing, for the pump field;

- the time-dependent dipole moment computed by means of the SFA, for the harmonic field.

The medium was modeled as argon at 75 mbar pressure, see chapter 5 for medium parameters. The dispersion was given by a Sellmeier formulation for the pump and dispersion and absorption from the interpolation of the atomic scattering factors [182] for the harmonic field.

The input beam was chosen to reproduce the experimental setup, i.e. 30 fs FWHM duration. However, to reduce the nonlinear propagation length, the focal length was reduced by a factor ~ 2 and consequently the Gaussian beam width was adjusted in order to reach in the focus the same intensity as in the experiment. The initial stage of propagation was performed by assuming linear propagation and using analytical formulas for Gaussian optics. The energy was 170 μJ, the initial beam width $w_0 = 150$ μm and the initial beam curvature $f = 3.2$ cm, so that the focus position is located at $\zeta = 2.8$ cm.

Figure 6.3(a), 6.3(b) and 6.3(c) show the harmonic spectra at three different propagation distances: 0.8 cm before the focus, at the focus and 0.68 cm after the focus, respectively. The experimental features are well reproduced. In particular, in Fig. 6.3(c) a ring structure around a central core is formed in correspondence of the 13th harmonic, as shown in the inset.
The 13th harmonic spectrum exhibits a ring structure also in the case before the focus [inset of Fig. 6.3(a)], although the overall divergence is smaller (the ring is smaller along the propagation angle coordinate). In correspondence of the focus the emission is mainly in the axial direction; a very faint ring structure is observed in this case at -3 decades, extending up to an angular aperture of ~ 8 mrad.
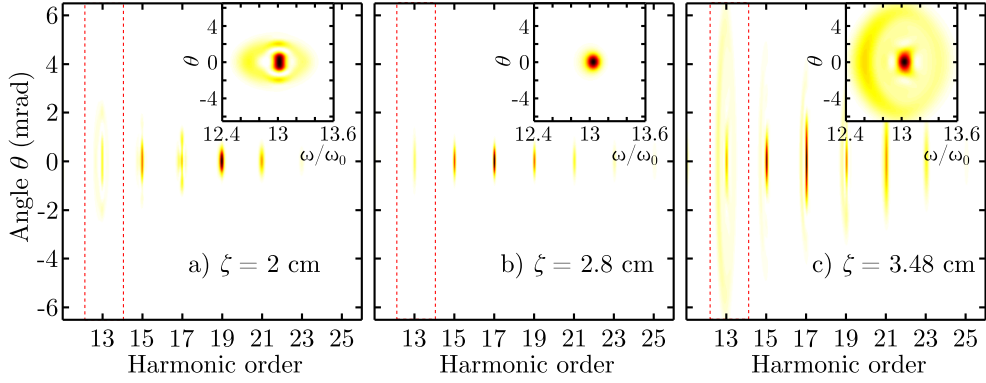
Figure 6.3: Spectrally resolved (propagation angle and harmonic order) HHG in argon at 75 mbar at three propagation distances: (a) $\zeta = 2$ cm, (b) $\zeta = 2.8$ cm (focus of the beam), and (c) $\zeta = 3.48$ cm. The intensity plots are in linear scale. The insets show the renormalized spectral intensity of the 13th harmonic, corresponding to the spectral region delimited by the dashed red lines.

By considering the spectral region $12 < (\omega/\omega_0) < 14$, the actual nearfields corresponding to the harmonic field at the 13th harmonic are retrieved by inverse Fourier transform of this spectral region. The results are shown in Fig. 6.4. A Bessel-like and a clear ring structure do appear in the nearfield for the two cases before and after the focus. Also at the focus position the spatio-temporal structure takes a Bessel-like shape, due to the very weak ring structure previously described.

A temporal gated spectrally resolved analysis was performed on the numerical results on axis ($r = 0$), by means of a Gaussian gate function of duration $T_p = 0.2$ fs. Figure 6.5 shows the results of this analysis in the region around $\tau = 0$ (center of the pump pulse), for the three propagation distances.
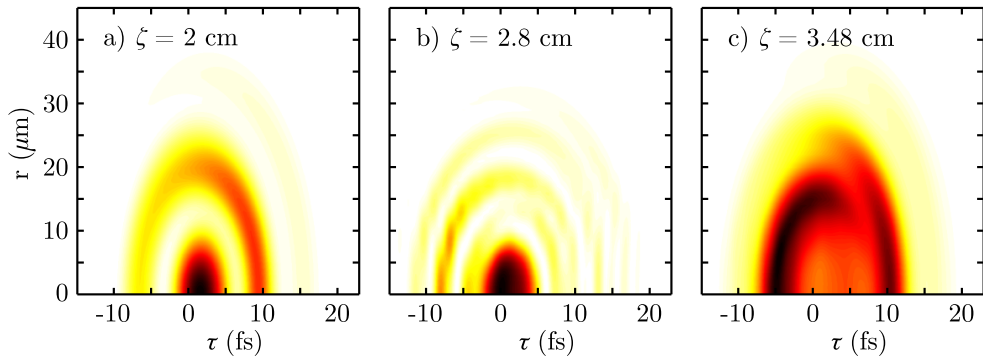
Figure 6.4: Nearfield of the 13th harmonic signal, evaluated by spectral filtering the region $12 < (\omega/\omega_0) < 14$. Propagation distances: (a) $\zeta = 2$ cm, (b) $\zeta = 2.8$ cm (focus of the beam), and (c) $\zeta = 3.48$ cm. Intensity plots in linear scale.
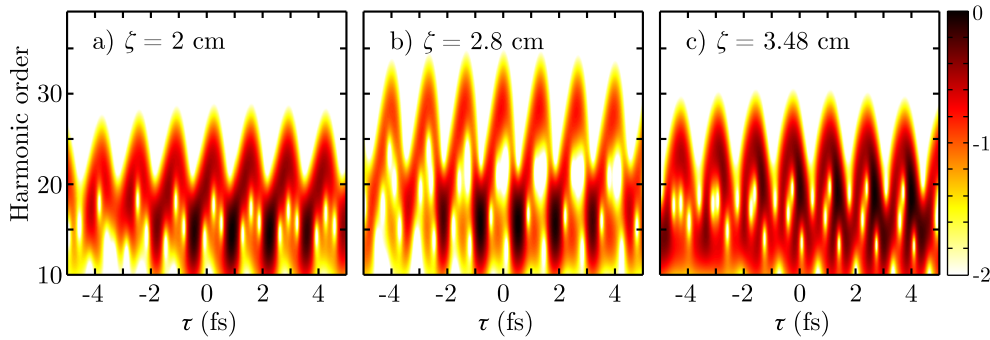
Figure 6.5: Time-gated spectral analysis (logarithmic plot over 2 decades) of the axial component ($r = 0$) of the harmonic field at propagation distances: (a) $\zeta = 2$ cm, (b) $\zeta = 2.8$ cm (focus of the beam), and (c) $\zeta = 3.48$ cm.

By looking at the harmonic contribution at low frequencies, Fig. 6.5(c) clearly show the simultaneous contribution from both short and long quantum trajectories, represented by the rising and falling slopes of the arc patterns (as described in the previous chapter). In particular, the intensities for these two components are comparable. This therefore supports the interpretation of the ring structure as interference between quantum trajectory contributions.

However, similar considerations do not apply to the other two cases, since in Fig. 6.5(a) and 6.5(b) this analysis tool does not give a clear indication as in the $\zeta = 3.84$ cm (after the focus) case.

A second set of simulations were thus launched, with absorption coefficients multiplied by a factor $1/100$, i.e. with an absorption length 100 times longer than in the previous simulations, in order to verify if this interference effect may be ascribed to propagation phase-matching effects or instantaneous effect. In particular, quantum path interference is an "instantaneous" effect, i.e. interference pattern are created when considering a single propagation distance. Other effects, such as Maker fringes [203–205], emerge because of phase matching effects, since they require propagation and interference with the field generated at previous positions.

Figures 6.6 and 6.7 show the spectral intensity evolution along propagation distance ζ at propagation angle $\theta = 0°$ for the frequency range around the 13th harmonic [Fig. 6.6], and at frequency $\omega = 13\omega_0$ as a function of propagation angles θ [Fig. 6.7]. The different cases correspond to: a) normal absorption coefficients, b) reduced absorption, and c) the instantaneous nonlinear polarization, evaluated with the SFA.

The figures show that in the particular case under examination the process is dominated by the instantaneous response of the atomic polarization, since cases a) and c) are almost identical. This is due to the very short absorption length correspond-
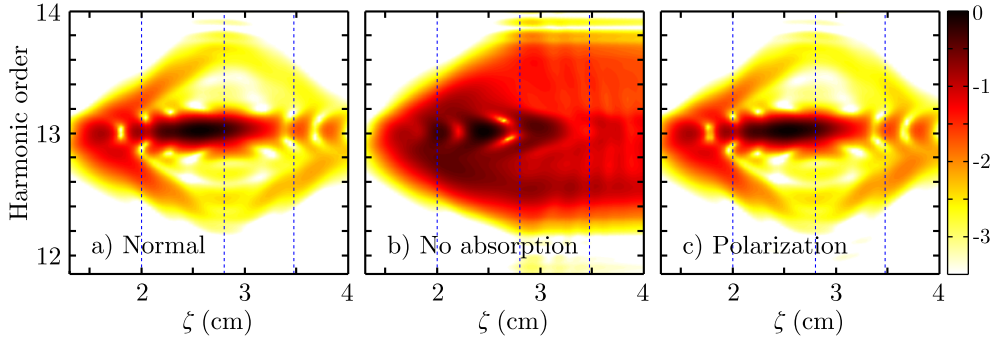
Figure 6.6: Evolution along propagation distance as a function of harmonic frequency (around $\omega = 13\omega_0$) of the spectral intensity (logarithmic plot over 3.5 decades) of the harmonic output at propagation angle $\theta = 0$. Cases: (a) with normal absorption coefficients, (b) with reduced absorption coefficients. Case (c) is the spectral intensity for the instantaneous nonlinear polarization, evaluated with the SFA. The vertical dashed lines represent the propagation distances considered in the previous analysis.
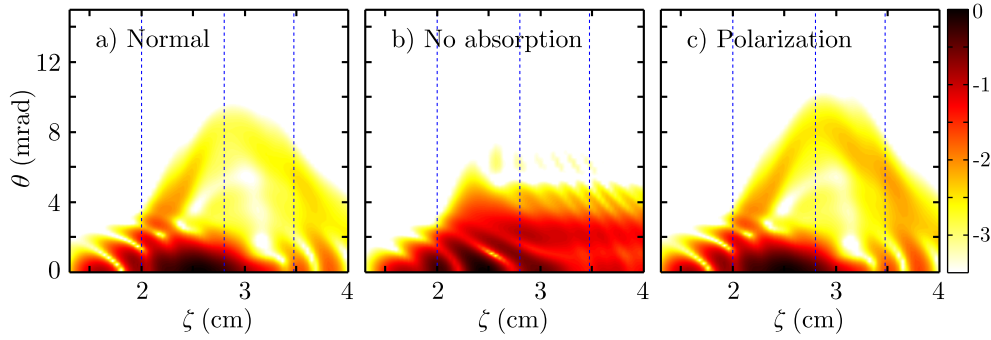
Figure 6.7: Evolution along propagation distance as a function of the propagation angle θ of the spectral intensity (logarithmic plot over 3.5 decades) of the harmonic output at frequency $\omega = 13\omega_0$. Cases: (a) with normal absorption coefficients, (b) with reduced absorption coefficients. Case (c) is the spectral intensity for the instantaneous nonlinear polarization, evaluated with the SFA. The vertical dashed lines represent the propagation distances considered in the previous analysis.

ing to low harmonic orders: the dynamics is dominated by the instantaneous contribution given by the nonlinear polarization, which, on the other hand, depends on the instantaneous pump field. These results thus exclude that this interference pattern is a build-up effect.

The case with reduced absorption is similar to the profiles given by the analysis of the nonlinear polarization (i.e. instantaneous effect) for the initial propagation distances, even if the spectral intensity modulations are smeared out. The intensity of the pump field and the intensity of the locally generated field are increasing, so

the importance of previous contributions is diminished.

On the other hand, this high intensity field generated in the region before and in correspondence of the focus is not absorbed in propagation because of the reduced absorption and it interferes with the field generated at successive propagation distances thus covering the structures originating from the nonlinear polarization in this after-focus region.

The ζ-varying size of the spectral modulation patterns may also be qualitatively understood in terms of quantum trajectories interference. The relative phase between the two contributions at given harmonic frequency is $\Delta\alpha^{(s-l)}I(r,\tau)$, where $\Delta\alpha = |\alpha^{(s)} - \alpha^{(l)}|$. When intensity increases, the instantaneous relative phase varies more rapidly along the spatial and temporal coordinates, determining a more dense fringe pattern in both directions (if we consider comparable contributions). This translates in the farfield (θ,ω) to a wider ring structure, if no particular phase profiles are assumed (or if the converging/diverging phase profile for the given frequency varies little along propagation distance).

6.3 Conclusions

In this chapter we analyzed the local interference between quantum trajectory contribution in HHG. In particular, starting from experimental measurements from a group of experts in this field, we reproduced and studied the results.

We found that in the particular regime under examination a ring is observed in the spatio-temporal farfield of the harmonic radiation at a low harmonic order order. The simulations showed that in this case the instantaneous harmonic contribution dominates with respect to phase-matching related effects, and we therefore interpreted the ring structure as the instantaneous interference pattern between short and long quantum trajectory contributions.

Possible future work on this field may involve a scan over propagation distances of the output harmonic field, in order to verify the numerical findings of Figs. 6.6 and 6.7, i.e. a variation of the interference pattern periodicity depending on the relative position with respect to the focal position. This could be performed by means of a ζ-scan in an experimental setup similar to the one shown in chapter 4, with the particular technical solutions of Ref. [191] for handling high harmonic propagation in vacuum.

Chapter 7

Nonlinear Airy Beams

This final chapter will deal with a particular class of monochromatic beams, the *Airy beams* [9, 10, 206]. These beams are (weakly) localized infinite-energy solution of the linear propagation equation which are stationary, i.e. their intensity shape profiles do not change in propagation, in an accelerating reference system. Contrary to conical wavepackets, Airy beams may be defined also in a 1-dimensional environment. They are characterized by a main intensity lobe that decays exponentially to zero on one side and decays with damped oscillations on the other. Finite energy realizations, in the shape of apodized Airy beams, preserve, for a finite propagation distance, the characteristic property that the main intensity lobe propagates free of diffraction whilst bending in the transverse direction, in the case of spatial Airy, or accelerating along the propagation direction, in the case of temporal Airy profile [207]. The ballistic properties of Airy beams [208] lead them to particular applications such as optically mediated particle clearing [209] or generation of curved plasma filaments [210].

In this chapter we will derive by means of analytical calculations and numerical integration the shape of stationary Airy-like solutions in the case of Kerr nonlinearity and nonlinear absorption. We will also present numerical and results to verify the possible generation of such nonlinear Airy-like beams. Finally, we will describe a series of experimental results confirming the numerical findings. These measurements were performed by the Ultrashort Non-linear Interactions and Sources group at the Foundation for Research and Technology Hellas (FORTH) of Heraklion, Greece.

7.1 Theoretical calculations

The propagation of the complex envelope of a *monochromatic* beam of frequency ω_0 in *one spatial dimension* can be described in the nonlinear case by a nonlinear

Schrödinger equation, derived from Eq. (1.27) with Kerr [Eq. (1.32)] and multi-photon absorption [Eq. (1.37)] terms:

$$\partial_z A = \frac{i}{2k_0}\partial_{xx}^2 A + ik_0\frac{n_2}{n_0}|A|^2 A - \frac{\beta^{(K)}}{2}|A|^{2K-2}A \qquad (7.1)$$

where for simplicity A is rescaled such that $|A|^2 = I$ represents the intensity of the electric field, and the coefficient describing the depletion of neutral atoms $(1 - \rho/\rho_0)$ is neglected in the nonlinear absorption term. K and $\beta^{(K)} \geq 0$ are the order and the coefficient of multiphoton absorption, respectively, see section 1.5.2. The nonlinear Kerr modification of the refractive index is $\delta n = n_2|A|^2$, see section 1.5.1.

Contrary to Eq. (1.27), only one transverse spatial dimension is considered in this case, and we are assuming the beam to be monochromatic, such that $A = A(x, z)$. Therefore, the change of reference frame given by Eq. (1.19) is not needed, and z is the propagation distance. Equation (7.1) is still derived assuming that the second order derivative $\partial_{zz}^2 A$ is negligible with respect to the first order term $2ik_0\partial_z A$.

In the linear case, Eq. (7.1) admits the Airy beam solution [206]:

$$A = \mathrm{Ai}(y)\exp\left[i\left(y\frac{\zeta}{2} + \frac{\zeta^3}{24}\right)\right] \qquad (7.2)$$

whose intensity profile is in the shape of a squared Airy function $\mathrm{Ai}(y)$ [211], and it is invariant in the *uniformly accelerated reference system* defined by the normalized coordinates:

$$
\begin{cases}
\zeta = \dfrac{z}{k_0 w_0^2} & (7.3) \\[2ex]
y = \dfrac{x}{w_0} - \dfrac{z^2}{4k_0^2 w_0^4} & (7.4)
\end{cases}
$$

with w_0 a typical length scale so that the acceleration, or curvature, in the (x, z) plane is given by $1/2k_0^2 w_0^3$.

Provided that Airy beams are stationary solutions in the accelerated reference system in the pure linear case, we are interested in finding *stationary* solutions in Airy-like shape also in the nonlinear case, Eq. (7.1). In particular, stationarity in this case means that the intensity profiles of the solutions do not change along propagation in the uniformly accelerated reference system. Moreover, we are searching for the nonlinear solutions that reduce to the Airy beams case in the absence of nonlinearity.

We thus expect that in the regions in which intensity is lower and thus nonlinear effects become less relevant, namely for $y \rightarrow \pm\infty$, the modulus of the solution

would approach the asymptotic approximations of the Airy function [211]:

$$\begin{cases} \mathrm{Ai}(y) \sim \dfrac{|y|^{-1/4}}{\pi^{1/2}} \sin\left(\dfrac{2}{3}|y|^{3/2} + \dfrac{\pi}{4}\right) & \text{for } y \to -\infty \quad (7.5) \\[2ex] \mathrm{Ai}(y) \sim \dfrac{y^{-1/4}}{2\pi^{1/2}} \exp\left(-\dfrac{2}{3}y^{3/2}\right) & \text{for } y \to +\infty \quad (7.6) \end{cases}$$

We therefore impose the constraints of a weakly localized tail (damped oscillating behavior) toward $y \to -\infty$ and an exponentially decaying tail toward $y \to +\infty$.

Equation (7.1) is rewritten in normalized units in the accelerated reference frame as:

$$\partial_\zeta A - \frac{1}{2}\zeta\partial_y A = \frac{i}{2}\partial_{yy}^2 A + i\gamma|A|^2 A - \alpha_{NL}|A|^{2K-2}A \qquad (7.7)$$

where the nonlinear parameters read as: $\gamma = k_0^2 n_2 w_0^2 / n_0$ and $\alpha_{NL} = \beta^{(K)} k_0 w_0^2 / 2$.

By following the procedure of Ref. [140], we consider modulus and phase of the complex envelope $A = \mathcal{A}(y,\zeta)\exp[i\phi(y,\zeta)]$, with $\mathcal{A} = |A|$. Substituting into Eq. (7.7) and gathering real and imaginary terms, the following system of equations is obtained:

$$\begin{cases} \partial_\zeta \mathcal{A}^2 - \zeta\mathcal{A}\partial_y\mathcal{A} = -2\mathcal{A}\partial_y\mathcal{A}\partial_y\phi - \mathcal{A}^2\partial_{yy}^2\phi - 2\alpha_{NL}\mathcal{A}^{2K} & (7.8) \\[2ex] \mathcal{A}\partial_\zeta\phi - \dfrac{1}{2}\zeta\mathcal{A}\partial_y\phi = \dfrac{1}{2}\partial_{yy}^2\mathcal{A} + \gamma\mathcal{A}^3 - \dfrac{\mathcal{A}}{2}\left(\partial_y\phi\right)^2 & (7.9) \end{cases}$$

The condition that the intensity $\mathcal{A}^2$ of the solution does not vary along ζ reverts to the constrain $\partial_\zeta\mathcal{A}^2 = 0$. Moreover, since we want the solutions to approach the linear Airy beam behavior of Eq. (7.2) for decreasing intensity or vanishing nonlinear terms, we assume for the phase the form:

$$\phi(y,\zeta) = \frac{\zeta}{2}y + \psi(y) + \frac{\zeta^3}{24} \qquad (7.10)$$

where $\psi(y)$ represents the additional phase term due to the nonlinear behavior. Equations (7.8) and (7.9) with these assumptions become:

$$\begin{cases} \partial_y\left(\mathcal{A}^2\partial_y\psi\right) = -2\alpha_{NL}\mathcal{A}^{2K} & (7.11) \\[2ex] \mathcal{A}\dfrac{y}{2} - \dfrac{1}{2}\partial_{yy}^2\mathcal{A} + \dfrac{\mathcal{A}}{2}\left(\partial_y\psi\right)^2 - \gamma\mathcal{A}^3 = 0 & (7.12) \end{cases}$$

Equation (7.11) may be rewritten as:

$$\mathcal{N}_y = \mathcal{A}^2\partial_y\psi = 2\alpha_{NL}\int_y^{+\infty}\mathcal{A}^{2K}\,\mathrm{d}y \qquad (7.13)$$

In particular, $\mathcal{N}_y$ represents the net power flux per unit propagation length through a y-boundary of a semi infinite domain $[y, +\infty)$ in the accelerating reference frame, which compensates for the power lost by nonlinear losses within this domain. Equation (7.11) is thus analogous to the continuity equation in presence of losses Eq. (3.22).

In the linear case $\alpha_{NL} = 0$, which implies $\mathcal{N}_y = 0$; the term $\psi(y)$ is thus a constant and Eq (7.10) reverts to the phase term corresponding to the linear Airy beam [9, 206].

Assuming total nonlinear losses to be finite, $\mathcal{N}_y$ increases from $\mathcal{N}_{+\infty} = 0$ at $y \to +\infty$ to $\mathcal{N}_{-\infty} = 2\alpha_{NL} \int_{-\infty}^{+\infty} \mathcal{A}^{2K} \, \mathrm{d}y$ at $y \to -\infty$, thereby establishing an additional curvature of the phase front in the weakly decaying tail of the beam, since $\partial_y \psi \to \mathcal{N}_{-\infty}/\mathcal{A}^2$, whereas the exponentially decaying tail has the curvature of the Airy beam. From the asymptotic behavior, we infer that finite nonlinear losses requires $K > 2$.

By introducing the new spatial coordinate $\varrho = \mathrm{sgn}(y)|y|^{3/2}$, where $\mathrm{sgn}(x)$ is the sign function, and $B(\varrho) = \mathcal{A}(y)|\varrho|^{1/6}$, we rewrite Eq. (7.12) in the limit $y, \varrho \to \pm\infty$:

$$
\begin{cases}
\partial_{\varrho\varrho}^2 B = \dfrac{4}{9} B & \text{for } \varrho \to +\infty \qquad (7.14) \\[3mm]
\partial_{\varrho\varrho}^2 B = -\dfrac{4}{9} B + \dfrac{4}{9}\dfrac{\mathcal{N}_{-\infty}^2}{B^3} & \text{for } \varrho \to -\infty \qquad (7.15)
\end{cases}
$$

Equation (7.14) admits exponentially decaying solutions $B \propto \exp[-(2/3)\varrho]$, as expected, while in the $\varrho \to -\infty$ case Eq. (7.15) admits solutions in the form:

$$
B^2(\varrho) = B_{-\infty}^2 \left[1 + C \sin\left(\frac{4}{3} |\varrho| \right) \right] \qquad (7.16)
$$

These exhibit oscillations of finite amplitude around the mean value $B_{-\infty}$ with contrast

$$
C = \left(1 - \frac{\mathcal{N}_{-\infty}^2}{B_{-\infty}^4} \right)^{1/2}
$$

decreasing as the amount of total losses increases. In the absence of nonlinear absorption ($N_{-\infty} \to 0$), Eq. (7.16) with maximum contrast $C = 1$ reduces to the asymptotics of Eq. (7.5). The contrast vanishes for $B_{-\infty}^2 = \mathcal{N}_{-\infty}$, showing that no solution exists above a certain threshold of total losses.

In analogy with the physics of nonlinear Bessel beams [140], nonlinear Airy solutions can be described as Airy beams reshaped by nonlinear absorption and Kerr effect, the former being responsible for the power flux from the weakly decaying tail toward the intense lobes where nonlinear absorption occurs and the latter of a nonlinear phase shift [212]. This may be expressed by considering the

expansion of the Airy function as the superposition of two linearly independent Hankel functions [211]:

$$\text{Ai}(y) = \frac{1}{2}\sqrt{\frac{|y|}{3}}\sum_{l=1}^{2} a_l \exp\left[i\frac{\pi}{6}(-1)^{l+1}\right] H_{1/3}^{(l)}\left(\frac{2}{3}|y|^{3/2}\right) \quad \text{for } y < 0 \quad (7.17)$$

where $a_1 = a_2 = 1$. Each of these Hankel profiles may be interpreted as carrying energy in the direction of, or opposite to the main lobe. In presence of absorptions, the amplitudes a_l are expected to be different from each other, thus originating a net power flux compensating for the losses. This is the origin of the lowering of the contrast in the oscillating tail.

7.2 Nonlinear solutions

Numerically integrating Eqs. (7.11) and (7.12) from $+\infty$ to $-\infty$ starting from the linear asymptotic behavior, we retrieve the intensity and phase profiles of the nonlinear solutions.
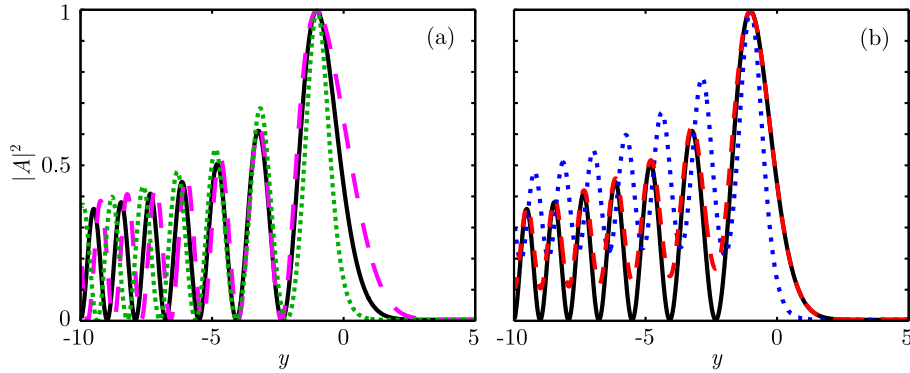
Figure 7.1: Nonlinear solutions compared to the linear one (black solid curve). Intensities are normalized to their maximum value and peak positions are shifted in order to overlap to the peak of the linear solution. (a) Pure Kerr solutions ($\alpha_{NL} = 0$) in the positive ($n_2 > 0$, green dotted curve) and negative ($n_2 < 0$, magenta dashed curve) Kerr nonlinearity case. (b) Solutions in presence of multiphoton absorption with $K = 5$, in the pure absorption case ($\gamma = 0$, red dashed curve) and positive Kerr and absorption (blue dotted curve). Thanks to rescaling properties of normalized units, these profiles apply to different media with the given multiphoton absorption order.

Figure 7.1(a) shows the normalized intensity profiles in the pure Kerr case, i.e. $\alpha_{NL} = 0$, in the positive and negative γ coefficient cases, corresponding to focusing ($n_2 > 0$) and defocusing ($n_2 < 0$) Kerr nonlinearity, respectively. The profiles were shifted along the y-axis to overlap to the maximum intensity peak of
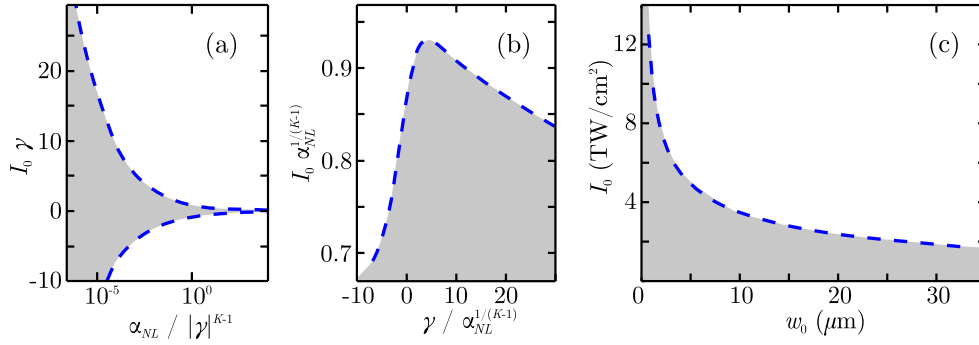
Figure 7.2: Domain of existence (shaded region) of nonlinear Airy-like solution. (a) and (b) as a function of normalized quantities, where I_0 is the maximum intensity at the peak of the profile [in (a) the horizontal axis is in logarithmic scale]. (c) is the existence domain in the case of water at $\lambda_0 = 800$ nm (see the text for parameter values) as a function of maximum intensity I_0 and width w_0 of the corresponding linear solution.

the linear case. In general, starting from the same initial conditions in the $y > 0$ semi-axis, the main intensity peak is shifted toward $y > 0$ for positive γ and in the opposite direction for negative γ, with respect to the linear case.

The width of the main lobe is narrower or wider depending on the sign (positive and negative, respectively) of the nonlinear coefficient. Since the reference system is the one referring to the linear case, the nonlinear solution still preserve the acceleration property of the linear Airy beam, although the relation between the width of the main lobe and the peak acceleration does no longer hold, due to the nonlinear behavior.

The solutions in the pure Kerr case were first derived in the context of the nonlinear Schrödinger equation in Ref. [213] and have recently been deeply investigated in Ref. [214]. These profiles have the form of Painlevé transcendents of second type.

The effect of multiphoton absorption, Fig. 7.1(b) (red dashed curve) for multiphoton order $K = 5$ and $\gamma = 0$, as explained in the previous section, is the reduction of the contrast C of the decaying oscillations. Increasing nonlinear absorption reduces the contrast of oscillations.

The simultaneous presence of both Kerr nonlinearity and multiphoton absorption determines features characteristic of each regime, Fig. 7.1(b) blue dotted curve, namely the narrowing of the central peak and the reduction of contrast.

We performed a scan in the parameters space to derive the region of existence of the stationary nonlinear solutions. The results, for $K = 5$, are shown in Fig. 7.2. The region of existence depends on a set of parameters, namely α_{NL}, γ and I_0, where I_0 is the maximum intensity of the nonlinear profile (i.e. the intensity of the main peak). Proper renormalization enables the plot to be performed as a func-

tion of two independent parameters. Figures 7.2(a) [with independent parameters $\alpha_{NL}/|\gamma|^{K-1}$ and γI_0] and 7.2(b) [with independent parameters $\gamma/\alpha_{NL}^{1/(K-1)}$ and $I_0\alpha_{NL}^{1/(K-1)}$] refer to these normalized units [a third possible choice of independent parameters could be $\alpha_{NL}I_0^{(K-1)}$ and γI_0]; by properly renormalizing the figure axis, Fig. 7.2(a) can be transformed into Fig. 7.2(b), and vice versa (except for the points in which $\alpha_{NL} = 0$ or $\gamma = 0$).

The shaded areas are the areas of existence of nonlinear solution. In particular, as previously shown, at fixed γ and given I_0 the solutions exist up to a certain maximum value of α_{NL}. For the pure Kerr case ($\alpha_{NL} = 0$), solutions exist $\forall n_2 > 0$. In the Kerr defocusing case, solutions have been shown [213, 214] to exist for $-\mathcal{M}^2 < \gamma I_0^{(\text{linear})} < 0$, where $I_0^{(\text{linear})}$ is the maximum intensity of the corresponding linear solution (i.e. the linear solution numerically obtained by starting from the same initial condition at $y \to +\infty$), and $\mathcal{M} = \max\{\text{Ai}(y)\}$ for $y \in \mathbb{R}$. However, the actual maximum intensity I_0 of the nonlinear profile is not limited, since it growths towards $+\infty$ as the (negative) quantity $\gamma I_0^{(\text{linear})}$ approaches the lower limit value.

Figure 7.2(c) shows the existence domain in the (I_0, w_0) space in the case of water at $\lambda_0 = 800$ nm, with $n_2 = 2.6 \times 10^{-16}$ cm^2/W [152], $n_0 = 1.3286$ and $\beta^{(5)} = 8.3 \times 10^{-50}$ cm^7/W^4 ($K = 5$ as before); w_0 is the width of the corresponding linear solution, which represents the acceleration $1/2k_0^2w_0^3$. The figure shows that within this choice of parameters, for a given acceleration of the profile (i.e. given w_0) nonlinear solutions exist up to a maximum intensity value.

7.3 Numerical and experimental verification

A relevant question is whether it is actually possible to excite or experimentally observe stationary nonlinear Airy beams. A series of problems may affect the experimental realization.

Firstly, these solutions carry infinite energy. In practical realizations of the beams one would resort to finite energy realizations that cannot guarantee perfect stationarity. However, as in the linear case in which finite energy Airy beams still exhibit the main stationary features over a limited distance [10], analogous to the Bessel zone for the propagation of finite energy Bessel beams, we may expect the nonlinear Airy to emerge during propagation in the nonlinear regime in a limited region along propagation distance. The rationale behind this reasoning is also based on the observation that stationary waveforms have been shown to act as attractor states for the dynamical evolution of laser beams and pulses in the nonlinear regime, for example dynamically evolving X-waves during ultrashort laser pulse filamentation [95, 96], and nonlinear unbalanced Bessel beams during

the evolution of high intensity Bessel beams [140, 212].

Secondly, the shaded regions of Fig. 7.2 represent the parameter area in which stationary nonlinear solutions exist, but a *stability analysis* of the solutions has not been performed yet. In particular, even if the theoretical solution does exist for a certain set of parameters, if such a solution falls inside an unstable zone, small perturbations will be amplified and the beam itself will evolve towards different profiles. On the base of the similarity with the nonlinear unbalanced Bessel beams, we may expect that nonlinear losses could determine a stabilizing factor for the solution. It is worth underlining that also unstable solutions may be locally obtained during the dynamical evolution of laser beams, such as the spatial Townes profile [134], observed close to the nonlinear focus of a self-focusing intense Gaussian beam [215].

Thirdly, the solutions were found in the pure one-dimensional case (i.e. no temporal evolution, no second transverse spatial coordinate). For what concerns two-dimensional solutions, in the linear case the existence of factorized solutions in the form of the product of two perpendicular one-dimensional Airy beams has been verified [9], but in general factorizability does not hold in the nonlinear case. Furthermore, the additional temporal coordinate may give rise to a series of instabilities which in an experimental framework could prevent the observation of nonlinear Airy solutions. For example, filamentation-like instabilities [216] could prevent or mask nonlinear Airy profiles.

We performed a series of numerical simulations, solving Eq. (7.1) for the same material parameters as in Fig. 7.2(c), i.e. in water at $\lambda_0 = 800$ nm input wavelength, for various increasing input intensities. The Airy beam was generated by applying a cubic phase mask to a Gaussian beam (FWHM=2.4 mm) followed by a focusing lens with focal length $f = 10$ cm after a linear propagation of distance f, to mimic a possible experimental setup. The Fourier transform of the input beam is then obtained in the focal plane of the lens [10]. This layout is schematically represented in the top-right corner of Fig. 7.3. The width of the corresponding linear Airy beam in the focal plane of the lens will be $w_0 = \mathcal{C}^{1/3} f / k_0$, where $\mathcal{C}$ is the cubic phase coefficient $\varphi = i\mathcal{C}x^3/3$. The acceleration of the linear profile is $1/2k_0^2 w_0^3 = k_0/(2\mathcal{C}f^3)$. A strong acceleration thus requires a short focal length f or a weak initial cubic phase coefficient $\mathcal{C}$. However, it also requires a large initial Gaussian apodization (corresponding to a broad spectral band) such that the Airy behavior is not completely masked by the Gaussian propagation.

The numerical results are shown as intensity plot versus transverse coordinate x and propagation coordinate z in Figs. 7.3(a), 7.3(b) and 7.3(c). Figure 7.3(a) shows the linear propagation of the finite-energy Airy beam for reference; at the focus position $z = 20$ cm the intensity profile, black curve of Fig. 7.3(d), is an apodized Airy profile. Figures 7.3(b) and 7.3(c) show the propagation for two high power cases: (b) for initial power 0.8 GW and (c) for 4.7 GW. The maximum
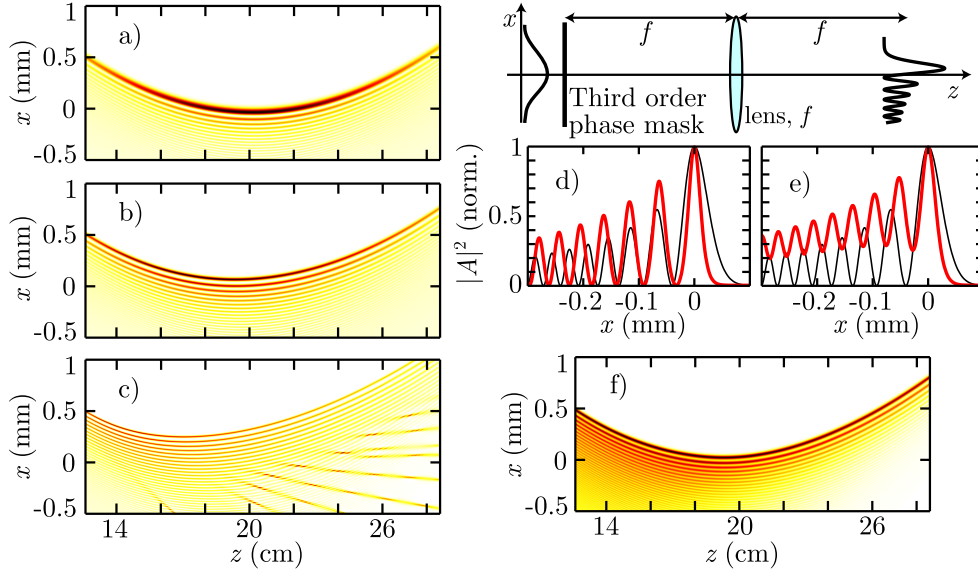
Figure 7.3: Numerical results: propagation in water with focal length $f = 10$ cm. The optical layout used to transform an input Gaussian beam with a spatial third order chirp into an Airy beam is shown in the top-right corner. Intensity evolution of (a) linear Airy with $w_0 = 30.3\,\mu$m, (b) Nonlinear Airy with peak intensity $I_0 = 0.2$ TW/cm^2, (c) Nonlinear Airy with peak intensity $I_0 = 1.2$ TW/cm^2. Intensity profile for case (b) is shown (red curve) in (d) compared to the linear one (black curve), both normalized. (f) Intensity evolution in the nonlinear case with artificially increased absorption coefficients, and (e) intensity profile (red curve) compared to the linear case, both normalized. The profiles of (d) and (e) are shown in the focal plane ($z = 20$ cm) of lens f.

intensities reached during propagation are: (b) 0.2 TW/cm^2 and (c) 1.2 TW/cm^2. A remarkable feature of these profiles is the formation of a slight asymmetry in the parabolic trajectory, barely visible in Fig. 7.3(b) and more evident in Fig. 7.3(c). This asymmetry is related to Kerr-induced self-focusing effect. This effect induces an effective focusing lens and, indeed, by slightly adjusting the position of the initial focusing lens f it is possible to partially compensate for this phase distortion. Complete compensation cannot be achieved at large distortions (i.e. at high peak intensities) due to the distributed nature and varying effective focal length of the Kerr lens.

The higher peak intensity generates also "tangential" emissions that propagate in straight lines at an angle from the main parabolic trajectory of the Airy main lobe. Similar tangential emission has already been experimentally observed [216]. This seems to indicate an instability in the nonlinear Airy profile which incurs as the parameters approach the border of the area of stationary-solution values, Fig. 7.2(c). In Ref. [214] this instability was found to emerge when, in the pure

Kerr case, the width of the main lobe is wider than twice the width of the soliton (shape-invariant hyperbolic secant solution of the nonlinear Schrödinger equation, see e.g. Ref. [217]) associated to the maximum peak intensity.

Figure 7.3(d) show a line-out of the beam profile of the (b)-case (red curve) at $z = 20$ cm, i.e. in the focal plane of the lens, compared to the linear case (black curve). The contraction of the main lobe, which also affects the periodicity of the side lobes, is clearly evident, whilst the effect of nonlinear losses, i.e. loss of contrast in the side-lobe oscillations, is hardly discernible.
We therefore performed an additional simulation, Fig. 7.3(f), with an initial power mid-way between cases (b) and (c), in the same medium with an increased nonlinear absorption coefficient, $\beta^{(5)} = 8.3 \times 10^{-45}$ cm^7/W^4. Figure 7.3(e) shows the intensity profile at the focus for this artificial case compared to the linear case: the strong reduction in the contrast of the Airy beam oscillations is now clear, indicating the presence of an inward flux that is stabilizing the energy loss in the main lobe.

7.4 Experimental results

A series of experiments were performed to verify the generation of nonlinear Airy profiles. The experiments were performed by the Ultrashort Non-linear Interactions and Sources (UNIS) group of Prof. Stelios Tzortzakis at the Institute of Electronic Structure and Laser at the Foundation for Research and Technology Hellas (IESL-FORTH), Heraklion, Greece.

One-dimensional Airy beams with increasing input energy were launched into two different nonlinear media: a 2 cm thick cuvette filled with water and a 2.5 cm thick sample of Polymethyl-methacrylate polymer (PMMA).
The experimental setup, shown in Fig. 7.4(a), comprised a spatial light modulator (SLM, Hamamatsu LCOS), which impressed onto a Gaussian shaped beam delivered by an amplified Ti:Sapph laser (35 fs pulse duration, 800 nm wavelength) a cubic spatial phase, together with a quadratic one corresponding to a cylindrical Fourier lens (one-dimensional counterpart of the setup of Ref. [218]). The beam then propagated through the nonlinear sample and the beam profile at the exit surface was imaged onto a CCD camera.

Figure 7.4(b) shows the nonlinear Airy spatial fluence profiles in logarithmic scale for three different input energies, 25 nJ (corresponding to linear propagation, blue dotted curve), 350 μJ (red curve) , and 530 μJ (black dashed curve), for an input cubic phase profile such that the linear Airy main lobe full width at half maximum (FWHM) is 159 μm. The main lobe undergoes an evident contraction that increases with increasing energy, in agreement with the theoretical prediction
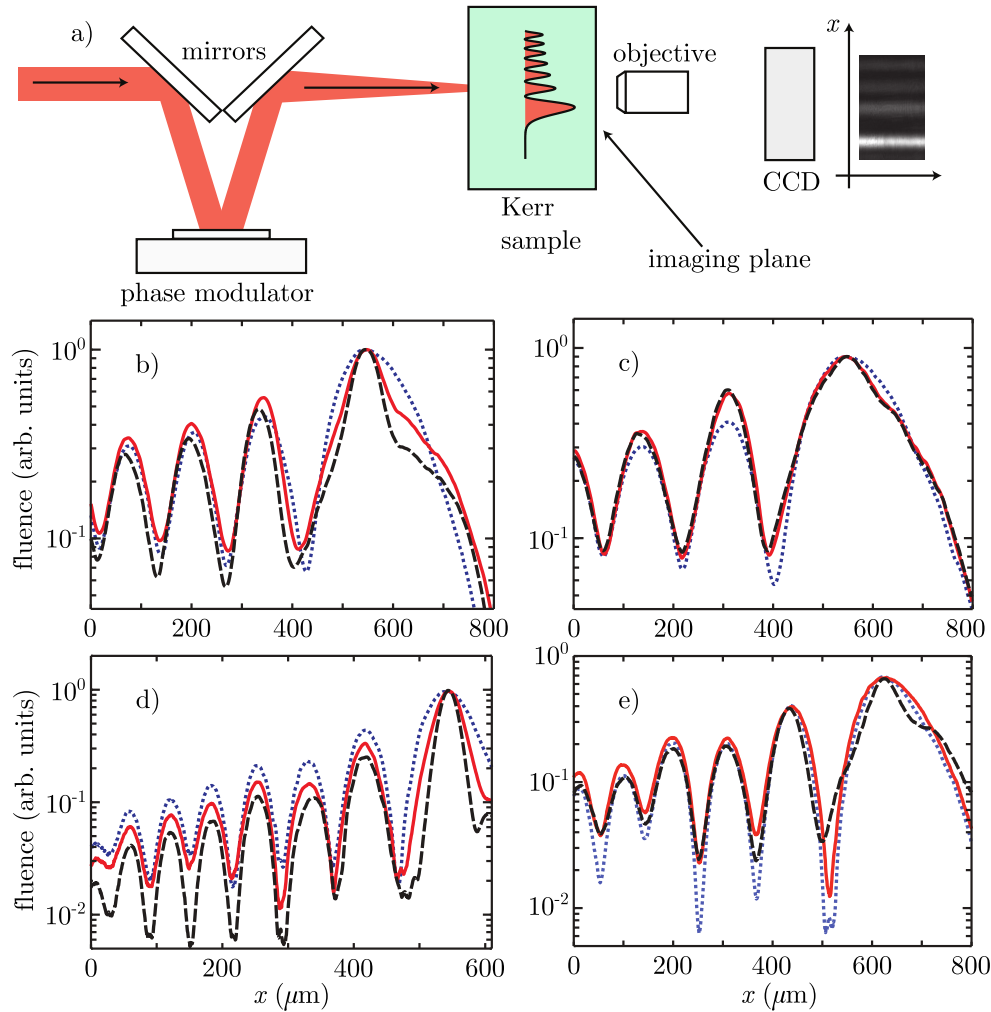
Figure 7.4: Experimental results: (a) experimental layout. Output fluence profiles in logarithmic scale for water: three input energies 25 nJ (blue dotted curve), 350 μJ (red solid curve), and 530 μJ (black dashed curve), for an input Airy with linear main lobe FWHM of (b) 159 μm and (c) 182 μm. Output fluence profiles in logarithmic scale for PMMA: energies 25 nJ (blue dotted curve), 78 μJ (red solid curve), and 246 μJ (black dashed curve), for an input Airy with linear main lobe FWHM of (d) 78 μm and (e) 136 μm.

[Fig. 7.1(a)] for the Kerr-dominated nonlinear Airy beam. In this regime the Airy propagation dynamics thus appear to be dominated by Kerr nonlinear effects.

Figure 7.4(c) shows the results for the same energies as in Fig. 7.4(b), starting from a different initial cubic phase term, corresponding to a wider FWHM of the linear Airy lobe: 182 μm. The reduced density of the Airy peaks and the correspondingly lower spatial intensity gradients imply that now both self-focusing

effects and the energy flux within the beam are weaker. Indeed, Kerr self-focusing effects are nearly absent. On the other hand, even if in both Figs. 7.4(b) and 7.4(c) the decrease of contrast due to nonlinear absorptions [see Fig. 7.1(b)] is hardly noticeable, it is more marked in this wider Airy lobe case.

A second set of measurements was performed in PMMA, with higher losses, due to the lower multiphoton absorption photon number, $K = 3$. As for the case of water, two different Airy widths were tested, namely 78 μm [Fig. 7.4(d)] and 136 μm [Fig. 7.4(e)] at three different energies 25 nJ (linear propagation, blue dotted curve), 78 μJ (red curve) and 246 μJ (black dashed curve). The dynamics are similar as in water: we observe a narrowing of the main lobe, and the larger Airy main peak case leading to increased nonlinear losses effects.
Although lacking the same resolution and dynamic range of the numerics, the experiments qualitatively show the predicted trends for the stationary nonlinear Airy beam.

7.5   Conclusions

In this chapter we demonstrated the existence of Airy-like solutions which preserve their intensity shape in an accelerating reference frame, in presence of Kerr nonlinearity and nonlinear losses. We numerically derived their typical features and linked them to the nonlinear effects of the medium.

We also performed a series of numerical simulations to mimic real experiments to verify the spontaneous generation of such beams over finite propagation distance in the finite-energy case. The simulations confirmed the theoretical findings, and we identified a regime of tangent-like instability, already observed [216] and discussed [214].

We presented a series of experiments qualitatively confirming the shape of nonlinear Airy solution in high intensity propagation in Kerr media.

Stationary nonlinear Airy beams could find practical applications in a similar fashion to stationary Bessel beams in technical improvements in the field of optical material micromachining [2, 219, 220].

Possible future development may be the study of the existence of Airy-shaped and nonlinear stationary solutions in a 2- or 3-dimensional environment. Moreover, following the development of light beams accelerating over arbitrary convex trajectories [221, 222], a study may be performed on their behavior in the nonlinear (Kerr and nonlinear losses) regime. An intriguing possibility could be the existence of nonlinear solutions accelerating over arbitrary trajectories.

Conclusions

In this thesis we investigated the role of conical wavepackets and laser pulse filamentation in potential applications at the frontier of nonlinear optics and high-field physics, such as high harmonic generation.
In particular, we developed a series of numerical codes and analysis tools to simulate and interpret the propagation of ultrashort laser pulses in nonlinear regimes, and the generation and co-propagation of high harmonics.

We concentrated our attention on the analysis of the spatio-temporal features of conical wavepackets, such as the property of independent tuning of phase and peak envelope velocity.
We developed a numerical tool for the analysis of the energy redistribution in the local frame of optical pulses, that we called energy density flux. By means of the energy density flux, we could interpret the specific properties of conical wavepackets from a simple geometrical perspective, and we found flux features characterizing the behavior of apodized conical wavepackets. These results in the linear case were verified by experimental measurements performed at the Institut de Ciències Fotòniques (ICFO) of Barcelona.
Moreover, we extended the energy flux investigation to the nonlinear case and, by means of a generalization of an existing phase retrieval technique, we analyzed a series of real data concerning the regime of ultrashort pulse filamentation. We were able to retrieve the typical energy flux signature of conical wavepacket in the experimental measurements of the filament, which was confirmed by numerical simulations.

The filamentation regime was also addressed from a different point of view: we studied the evolution along propagation distance of the ultraviolet spectral component around the third harmonic of the pump pulse. By means of a series of numerical simulations, we derived the temporal profiles of this spectral frequency range and the corresponding phase, and verified the possibility of pulse compression for the generation of few-cycle pulses (duration ≤ 3 fs) in the near and deep ultraviolet. This work was performed in tight collaboration with the experimental Ultrafast Laser Optics group at the Leibniz Universität of Hannover, that provided the set of measurements which constituted the starting point for this investigation.

Ultrashort pulses in the ultraviolet and soft X-ray region can also be generated in a different nonlinear process, namely high harmonic generation (HHG). We analyzed the influence of the peculiar carrier-envelope features of conical wavepackets in harmonic temporal and spectral output from HHG with very short pulses in argon. We found that the relative shift of the envelope with respect to the carrier wave (related to the difference between phase and envelope velocities on axis) determined in our case two main effects.

The first one was the local (along propagation distance) generation of almost isolated pulses of 300-350 as duration.

The second one was the selection of quantum trajectory contribution (and therefore associated temporal chirp and divergence) via a phase matching effect related to the instantaneous intensity of the field peaks. In the particular case under examination, we found an enhancement of the long trajectory contribution for a peak envelope velocity v smaller than the phase velocity, and an enhancement of the short trajectory contribution for the opposite case.

The effect of the simultaneous presence of different quantum trajectory contributions in HHG was also analyzed in the case of loosely focused Gaussian pulses. The numerical studies started from a series of experimental results performed by the Attoscience and Ultrafast Optics group at the ICFO of Barcelona. These measurements exhibited a clear ring-shaped structure in the spatio-temporal farfield (i.e. wavelength and propagation angles) of low order harmonics. We performed a set of numerical simulations, which revealed that this effect is mainly related to the instantaneous nonlinear polarization. We could therefore exclude phase matching processes. We thus described the complex spectral pattern as due to an interference between the two main quantum trajectory contributions, and we investigated its evolution along propagation distance in correspondence of the focus of the Gaussian beam.

Finally, we presented our results concerning a particular kind of monochromatic wavepackets: Airy beams. We found and described stationary nonlinear Airy-like solutions in presence of instantaneous Kerr effect and nonlinear losses. These profiles, in particular, present features similar to the unbalanced Bessel beam case [140], namely a reduction of oscillation contrast which determines a net energy flux towards the main peak of the beam, where absorption takes place. We numerically investigated and verified the generation of such stationary profiles, in view of possible experimental realizations.

These experiments were performed by the Ultrashort Non-linear Interactions and Sources group at the Foundation for Research and Technology Hellas in Heraklion, Greece. The experimental results are in agreement with our theoretical predictions.

In conclusion, we underline possible future work along the research lines developed during this thesis.

In the field of the energy flux density studies we proposed a phase retrieval technique derived from the mathematics at the base of this numerical tool. We presented a series of very preliminary results at the end of chapter 3. These initial studies can be brought into more depth and eventually applied to an actual experimental framework.

A parallel future perspective is the application of the energy flux tool for the study and the comprehension of other optical systems based on the same evolution equation (nonlinear Schrödinger equation), such as nonlinear propagation in optical fibers [16].

The work on the spectral evolution along the filament and the subsequent ultraviolet component isolation and compression is still a topic under development. In particular, experimental measurements of the temporal profile of the third harmonic component are already scheduled in the following months. These in turn will determine the needs for a set of parallel numerical simulations for parameter optimization.

HHG by conical wavepackets has been studied in this thesis only from a numerical point of view. Therefore a future perspective of these studies is their experimental realizations with very short laser pulses. We proposed possible experimental scenarî, such as the generation of pulsed Bessel beams in hollow core fibers; however, these will require further simulations to take into account propagation features possibly different from the numerical case presented in chapter 5.

The work on quantum trajectory interference deserves further inspection. In particular a scan of the evolution of these interference patterns along propagation distance would bring a great help in understanding the phenomenon, for the fine tuning of the harmonic output.

Finally, the work on stationary nonlinear Airy is linked to possible applications such as material machining. Possible future development of this work may be the study in the 2- and 3- dimensional case. In particular, a review of all the possible instability channels could help all nonlinear applications related to laterally or temporally accelerating pulses.

An intriguing development of the 1-dimensional case is the study of possible stationary nonlinear beams accelerating along arbitrary convex trajectories.

Appendix A

Publications and presentations

A.1   Publications

Before the Ph.D. studies

1. D. Faccio, A. Dubietis, G. Tamosauskas, P. Polesana, G. Valiulis, A. Piskarskas, A. Lotti, A. Couairon, P. Di Trapani, **Phase- and group-matched nonlinear interactions mediated by multiple filamentation in Kerr media**, *Phys. Rev. A* **76**(5), 055802 (2007).
[doi: 10.1103/PhysRevA.76.055802]

2. D. Faccio, A. Averchi, A. Lotti, P. Di Trapani, A. Couairon, D. Papazoglou, S. Tzortzakis, **Ultrashort laser pulse filamentation from spontaneous X Wave formation in air**, *Opt. Express* **16**(3), 1546–1551 (2008).
[doi: 10.1364/OE.16.001565]

3. D. Faccio, A. Lotti, M. Kolesik, J. V. Moloney, S. Tzortzakis, A. Couairon, P. Di Trapani, **Spontaneous emergence of pulses with constant carrier-envelope phase in femtosecond filamentation**, *Opt. Express* **16**(15), 11103–11114 (2008). [doi: 10.1364/OE.16.011103]

4. F. Bragheri, D. Faccio, F. Bonaretti, A. Lotti, M. Clerici, O. Jedrkiewicz, C. Liberale, S. Henin, L. Tartara, V. Degiorgio, P. Di Trapani, **Complete retrieval of the field of ultrashort optical pulses using the angle-frequency spectrum**, *Opt. Lett.* **33**(24), 2952–2954 (2008).
[doi: 10.1364/OL.33.002952]

5. D. Faccio, M. Clerici, A. Averchi, A. Lotti, O. Jedrkiewicz, A. Dubietis, G. Tamosauskas, A. Couairon, F. Bragheri, D. Papazoglou, S. Tzortzakis, P. Di Trapani, **Few-cycle laser pulse collapse in Kerr media: the role of group**

velocity dispersion and X-wave formation, *Phys. Rev. A* **78**(3), 033826 (2008). [doi: 10.1103/PhysRevA.78.033826]

6. M. Clerici, D. Faccio, A. Lotti, E. Rubino, O. Jedrkiewicz, J. Biegert, P. Di Trapani, **Finite-Energy, Accelerating Bessel Pulses**, *Opt. Express* **16**(24), 19807–19811 (2008). [doi: 10.1364/OE.16.019807]

7. D. Faccio, A. Averchi, A. Lotti, M. Kolesik, J. V. Moloney, A. Couairon, P. Di Trapani, **Generation and control of extreme-blue shifted continuum peaks in optical Kerr media**, *Phys. Rev. A* , **78**(3), 033825 (2008). [doi: 10.1103/PhysRevA.78.033825]

Presented in this dissertation

1. D. Faccio, A. Lotti, A. Matijosius, F. Bragheri, V. Degiorgio, A. Couairon, P. Di Trapani, **Experimental energy-density flux characterization of ultrashort laser pulse filaments**, *Opt. Express* **17**(10), 8193–8200 (2009). [doi: 10.1364/OE.17.008193]

2. A. Lotti, A. Couairon, D. Faccio, P. Di Trapani, **Energy-flux characterization of conical and space-time coupled wave packets**, *Phys. Rev. A* **81**(2), 023810 (2010). [doi: 10.1103/PhysRevA.81.023810]

3. A. Lotti, A. Couairon, D. Faccio, P. Di Trapani, **Energy density characterization of complex ultrashort laser pulses**, *SPIE Proceedings* Vol. **7728** Nonlinear Optics and Applications IV, 77280L (2010). [doi: 10.1117/12.854551]

4. A. Lotti, D. Faccio, A. Couairon, M. B. Gaarde, P. Di Trapani, **Carrier-envelope shearing and isolated attosecond pulse generation**, *Phys. Rev. A* **83**(5), 053804 (2011). [doi: 10.1103/PhysRevA.83.053804]

5. A. Lotti, D. Faccio, A. Couairon, D. G. Papazoglou, P. Panagiotopoulos, D. Abdollahpour, S. Tzortzakis, **Stationary nonlinear Airy beams**, *Phys. Rev. A* **84**(2), 021807(R) (2011). [doi: 10.1103/PhysRevA.84.021807]

6. S. M. Teichmann, D. R. Austin, P. Bates, S. Cousin, A. Grün, M. Clerici, A. Lotti, D. Faccio, P. Di Trapani, A. Couairon, J. Biegert, **Trajectory interferences in a semi-infinite gas cell**, *Laser Phys. Lett.*, *in press*

7. P. Panagiotopoulos, D. Abdollahpour, A. Lotti, A. Couairon, D. Faccio, D.G. Papazoglou, S. Tzortzakis, **Nonlinear propagation dynamics of finite energy Airy beams**, *Phys. Rev. A*, *submitted*

Other works performed during the Ph.D. studies

1. D. Faccio, S. Cacciatori, V. Gorini, V.G. Sala, A. Averchi, A. Lotti, M. Kolesik, J.V. Moloney, **Analogue Gravity and ultrashort laser pulse filamentation**, *EuroPhys. Lett.* **89**(3), 34004 (2010).
   [doi: 10.1209/0295-5075/89/34004]

2. M. Clerici, D. Faccio, E. Rubino, A. Lotti, A. Couairon, P. Di Trapani, **Space-time focusing of Bessel-like pulses**, *Opt. Lett.* **35**(19), 3267–3269 (2010). [doi: 10.1364/OL.35.003267]

3. F. Ferri, A. D'Angelo, M. Lee, A. Lotti, M. C. Pigazzini, K. Singh, R. Cerbino, **Kinetics of colloidal fractal aggregation by differential dynamic microscopy**, *Eur. Phys. J. Special Topics* **199**, 139–148 (2011). [doi: 10.1140/epjst/e2011-01509-9]

4. J. M. Brown, A. Lotti, A. Teleki, M. Kolesik, **Exactly solvable model for nonlinear light-matter interaction in an arbitrary time-dependent field**, *Phys. Rev. A* **84**(6), 063424 (2011). [doi: 10.1103/PhysRevA.84.063424]

A.2   Contributions at international conferences

Before the Ph.D. studies

- <u>A. Averchi</u>, D. Faccio, A. Lotti, M. Kolesik, J. V. Moloney, A. Couairon, P. Di Trapani, **Tunable, octave-spanning supercontinuum driven by X-Waves formation in condensed Kerr media**, *XVI International Conference on Ultrafast Phenomena*, Stresa, Italy (2008)

- A. Averchi, D. Faccio, A. Lotti, P. Di Trapani, <u>A. Couairon</u>, D. Papazoglou, S. Tzortzakis, **Demonstration of Spontaneously Generated Conical Waves during Ultrashort Laser Pulse Filamentation in Air**, *CLEO/QUELS*, S. Jose, USA (2008)

- <u>A. Lotti</u>, D. Faccio, M. Kolesik, J. V. Moloney, S. Tzortzakis, A. Couairon, P. Di Trapani, **Spontaneous emergence of pulses with constant carrier-envelope phase in femtosecond filamentation**, *EOS Annual Meeting 2008 / Topical Meeting on Nonlinear Optics: Materials, Devices and Spatio-Temporal Effects*, Paris, France (2008)

- M. Clerici, O. Jedrkiewicz, D. Faccio, A. Averchi, A. Lotti, E. Rubino, G. Valiulis, L. Tartara, V. Degiorgio, A. Couairon, M. Kolesik, P. Di Trapani, **Controlled X Wave Formation in Bulk Quadratic and Cubic Nonlinear**

Media, *21st Annual Meeting of the IEEE LEOS*, Newport Beach, CA - USA (2008)

During the Ph.D. studies

- <u>D. Faccio</u>, A. Lotti, M. Kolesik, J.V. Moloney, S. Tzortzakis, A. Couairon, P. Di Trapani, **Envelope- and Carrier-Phase Studies in Filaments: Energy Density Flux and CEP Stabilization**, *2nd International Symposium on Filamentation*, Palaiseau, France (2008)

- <u>D. Faccio</u>, A. Lotti, P. Di Trapani, A. Couairon, **Energy-density characterization of ultrashort laser pulses**, *Complex Phenomena in Nonlinear Physics*, Erice, Italy (2009)

- <u>A. Lotti</u>, A. Couairon, D. Faccio, P. Di Trapani, **Energy density characterization of ultrashort laser pulses**, *SPIE Photonics Europe*, Brussels, Belgium (2010).

- <u>A. Couairon</u>, C.L. Arnold, A. Mysyrowicz, P.P. Kiran, S. Bagchi, S.R. Krishnan, G. Ravindra Kumar, M.B. Gaarde, D. Steingrube, E. Schultz, M. Kovacev, A. Lotti, D. Faccio, P. Di Trapani, P. Panagiotopoulos, N.K. Efremidis, D. Papazoglou, S. Tzortzakis, **Filamentation without intensity clamping**, *3rd International Symposium on Filamentation*, Aghia Pelaghia, Crete, Greece (2010).

- <u>S. Teichmann</u>, D. Austin, P. Bates, S. Cousin, A. Grün, J. Biegert, A. Couairon, M. Clerici, A. Lotti, D. Faccio, P. Di Trapani, **Angle-frequency analysis of high-order harmonic generation**, *HILAS 2011*, Istanbul, Turkey (2011).

- <u>A. Couairon</u>, A. Lotti, P. Panagiotopoulos, D. Abdollahpour, D. Faccio, D.G. Papazoglou, S. Tzortzakis, **Nonlinear propagation and filamentation of intense Airy beams in transparent media**, *SPIE Photonics Europe*, Brussels, Belgium (2012), *submitted*.

Bibliography

[1] A. Bahabad, M. M. Murnane, H. C. Kapteyn, **Manipulating nonlinear optical processes with accelerating light beams**, *Phys. Rev. A* **84**(3), 033819 (2011). [doi:10.1103/PhysRevA.84.033819].

[2] M. K. Bhuyan, F. Courvoisier, P. A. Lacourt, M. Jacquot, R. Salut, L. Furfaro, J. M. Dudley, **High aspect ratio nanochannel machining using single shot femtosecond Bessel beams**, *Appl. Phys. Lett.* **97**(8), 081102 (2010). [doi:10.1063/1.3479419].

[3] P. Polynkin, M. Kolesik, A. Roberts, D. Faccio, P. Di Trapani, J. Moloney, **Generation of extended plasma channels in air using femtosecond Bessel beams**, *Opt. Express* **16**(20), 15733–15740 (2008). [doi:10.1364/OE.16.015733].

[4] S. Akturk, B. Zhou, M. Franco, A. Couairon, A. Mysyrowicz, **Generation of long plasma channels in air by focusing ultrashort laser pulses with an axicon**, *Opt. Commun.* **282**(1), 129–134 (2009). [doi:10.1016/j.optcom.2008.09.048].

[5] D. Faccio, A. Averchi, A. Dubietis, P. Polesana, A. Piskarskas, P. Di Trapani, A. Couairon, **Stimulated Raman X waves in ultrashort optical pulse filamentation**, *Opt. Lett.* **32**(2), 184–186 (2007). [doi:10.1364/OL.32.000184].

[6] T. Brabec, F. Krausz, **Intense few-cycle laser fields: Frontiers of nonlinear optics**, *Rev. Mod. Phys.* **72**, 545 (2000).

[7] T. Popmintchev, M.-C. Chen, P. Arpin, M. M. Murnane, H. C. Kapteyn, **The attosecond nonlinear optics of bright coherent X-ray generation**, *Nature Photon.* **4**(12), 822–832 (2010). [doi:10.1038/nphoton.2010.256].

[8] M. Hentschel, R. Kienberger, Ch. Spielmann, G. A. Reider, N. Milosevic, T. Brabec, P. Corkum, U. Heinzmann, M. Drescher, F. Krausz, **Attosecond metrology**, *Nature* **414**(6863), 509–513 (2001). [doi:10.1038/35107000].

[9] G. A. Siviloglou, D. N. Christodoulides, **Accelerating finite energy Airy beams**, *Opt. Lett.* **32**(8), 979–981 (2007). [doi:10.1364/OL.32.000979].

[10] G. A. Siviloglou, J. Broky, A. Dogariu, D. N. Christodoulides, **Observation of Accelerating Airy Beams**, *Phys. Rev. Lett.* **99**(21), 213901 (2007). [doi:10.1103/PhysRevLett.99.213901].

[11] M. D. Feit, J. A. Fleck, Jr., **Beam nonparaxiality, filament formation, and beam breakup in the self-focusing of optical beams**, *J. Opt. Soc. Am. B* **5**(3), 633–640 (1988). [doi:10.1364/JOSAB.5.000633].

[12] A. V. Husakou, J. Herrmann, **Supercontinuum Generation of Higher-Order Solitons by Fission in Photonic Crystal Fibers**, *Phys. Rev. Lett.* **87**(20), 203901 (2001). [doi:10.1103/PhysRevLett.87.203901].

[13] M. A. Porras, **Propagation of single-cycle pulsed light beams in dispersive media**, *Phys. Rev. A* **60**(6), 5069–5073 (1999). [doi:10.1103/PhysRevA.60.5069].

[14] T. Brabec, F. Krausz, **Nonlinear Optical Pulse Propagation in the Single-Cycle Regime**, *Phys. Rev. Lett.* **78**(17), 3282–3285 (1997). [doi:10.1103/PhysRevLett.78.3282].

[15] A. Couairon, A. Mysyrowicz, **Femtosecond filamentation in transparent media**, *Phys. Rep.* **441**, 47–189 (2007). [doi:10.1016/j.physrep.2006.12.005].

[16] A. C. Newell, J. V. Moloney, **Nonlinear Optics** (Addison-Wesley, Redwood City, California, 1992).

[17] B. E. A. Saleh, M. C. Teich, **Fundamentals of Photonics** (Wiley-Interscience, New York, 1991).

[18] J. H. Marburger, **Self-focusing: Theory**, *Prog. Quantum Electron.* **4**, 35–110 (1975). [doi:10.1016/0079-6727(75)90003-8].

[19] M. D. Feit, J. A. Fleck, **Effect of refraction on spot-size dependence of laser-induced breakdown**, *Appl. Phys. Lett.* **24**(4), 169–172 (1974). [doi:10.1063/1.1655139].

[20] Yu. P. Raizer, **Heating of a gas by a powerful light pulse**, *Sov. Phys. JETP* **21**(5), 1009 (1965).

[21] S. Skupin, R. Nuter, L. Bergé, **Optical femtosecond filaments in condensed media**, *Phys. Rev. A* **74**, 043813 (2006). [doi:10.1103/PhysRevA.74.043813].

[22] F. DeMartini, C. H. Townes, T. K. Gustafson, P. L. Kelley, **Self-steepening of light pulses**, *Phys. Rev.* **164**(2), 312–323 (1967). [doi:10.1103/PhysRev.164.312].

[23] L. V. Keldysh, **Ionization in the field of a strong electromagnetic wave**, *Sov. Phys. JETP* **20**, 1307–1314 (1965).

[24] S. Augst, D. D. Meyerhofer, D. Strickland, S. L. Chint, **Laser ionization of noble gases by Coulomb-barrier suppression**, *J. Opt. Soc. Am. B* **8**(4), 858–867 (1991). [doi:10.1364/JOSAB.8.000858].

[25] A. M. Perelomov, V. S. Popov, M. V. Terent'ev, **Ionization of Atoms in an Alternating Electric Field**, *Sov. Phys. JETP* **23**, 924–934 (1966).

[26] A. M. Perelomov, V. S. Popov, M. V. Terent'ev, **Ionization of Atoms in an Alternating Electric Field: II**, *Sov. Phys. JETP* **24**, 207 (1967).

[27] A. M. Perelomov, V. S. Popov, **Ionization of Atoms in an Alternating Electrical Field. III**, *Sov. Phys. JETP* **25**, 336 (1967).

[28] M. V. Ammosov, N. B. Delone, V. P. Krainov, **Tunnel ionization of complex atoms and of atomic ions in an alternating electromagnetic field**, *Sov. Phys. JETP* **64**(6), 1191–1194 (1986).

[29] F. A. Ilkov, J. E. Decker, S. L. Chin, **Ionization of atoms in the tunnelling regime with experimental evidence using Hg atoms**, *J. Phys. B: At. Mol. Opt. Phys.* **25**(19), 4005 (1992). [doi:10.1088/0953-4075/25/19/011].

[30] K. Mishima, M. Hayashi, J. Yi, S. H. Lin, H. L. Selzle, E. W. Schlag, **Generalization of Keldysh's theory**, *Phys. Rev. A* **66**(3), 033401 (2002). [doi:10.1103/PhysRevA.66.033401].

[31] T. Pfeifer, C. Spielmann, G. Gerber, **Femtosecond x-ray science**, *Rep. Prog. Phys.* **69**(2), 443–505 (2006). [doi:10.1088/0034-4885/69/2/R04].

[32] A. McPherson, G. Gibson, H. Jara, U. Johann, T. S. Luk, I. A. McIntyre, K. Boyer, C. K. Rhodes, **Studies of multiphoton production of vacuum-ultraviolet radiation in the rare gases**, *J. Opt. Soc. Am. B* **4**(4), 595–601 (1987). [doi:10.1364/JOSAB.4.000595].

[33] M. Ferray, A. L'Huillier, X. F. Li, L. A. Lompre, G. Mainfray, C. Manus, **Multiple-harmonic conversion of 1064 nm radiation in rare gases**, *J. Phys. B: At. Mol. Opt. Phys.* **21**(3), L31 (1988). [doi:10.1088/0953-4075/21/3/001].

[34] P. B. Corkum, **Plasma perspective on strong field multiphoton ionization**, *Phys. Rev. Lett.* **71**(13), 1994–1997 (1993). [doi:10.1103/PhysRevLett.71.1994].

[35] K. C. Kulander, K. J. Schafer, J. L. Krause, **Dynamics of Short-Pulse Excitation, Ionization and Harmonic Conversion**. In *Proceedings of the Super-Intense Laser-Atom Physics III (SILAP III) Workshop* (Edited by B. Piraux, A. L'Huillier, K. Rzazewski), vol. 316 of *NATO ASI, Series B*, 95–110 (Plenum Press, New York, 1993).

[36] J. L. Krause, K. J. Schafer, K. C. Kulander, **High-order harmonic generation from atoms and ions in the high intensity regime**, *Phys. Rev. Lett.* **68**(24), 3535–3538 (1992). [doi:10.1103/PhysRevLett.68.3535].

[37] K. S. Budil, P. Salières, M. D. Perry, A. L'Huillier, **Influence of ellipticity on harmonic generation**, *Phys. Rev. A* **48**(5), R3437–R3440 (1993). [doi:10.1103/PhysRevA.48.R3437].

[38] P. Dietrich, N. H. Burnett, M. Ivanov, P. B. Corkum, **High-harmonic generation and correlated two-electron multiphoton ionization with elliptically polarized light**, *Phys. Rev. A* **50**(5), R3585–R3588 (1994). [doi:10.1103/PhysRevA.50.R3585].

[39] M. Lewenstein, Ph. Balcou, M. Yu. Ivanov, A. L'Huillier, P. B. Corkum, **Theory of high-harmonic generation by low-frequency laser fields**, *Phys. Rev. A* **49**(3), 2117–2132 (1994). [doi:10.1103/PhysRevA.49.2117].

[40] P. Antoine, A. L'Huillier, M. Lewenstein, P. Salières, B. Carré, **Theory of high-order harmonic generation by an elliptically polarized laser field**, *Phys. Rev. A* **53**(3), 1725–1745 (1996). [doi:10.1103/PhysRevA.53.1725].

[41] H. A. Bethe, E. E. Salpeter, **Quantum mechanics of one and two electron atoms** (Academic Press, New York, 1957).

[42] M. Lewenstein, P. Salières, A. L'Huillier, **Phase of the atomic polarization in high-order harmonic generation**, *Phys. Rev. A* **52**(6), 4747–4754 (1995). [doi:10.1103/PhysRevA.52.4747].

[43] M. B. Gaarde, F. Salin, E. Constant, Ph. Balcou, K. J. Schafer, K. C. Kulander, A. L'Huillier, **Spatiotemporal separation of high harmonic radiation into two quantum path components**, *Phys. Rev. A* **59**(2), 1367–1373 (1999). [doi:10.1103/PhysRevA.59.1367].

[44] Ph. Balcou, A. S. Dederichs, M. B. Gaarde, A. L'Huillier, **Quantum-path analysis and phase matching of high-order harmonic generation and high-order frequency mixing processes in strong laser fields**, *J. Phys. B: At. Mol. Opt. Phys.* **32**(12), 2973–2989 (1999). [doi:10.1088/0953-4075/32/12/315].

[45] P. Salières, A. L'Huillier, M. Lewenstein, **Coherence Control of High-Order Harmonics**, *Phys. Rev. Lett.* **74**(19), 3776–3779 (1995). [doi:10.1103/PhysRevLett.74.3776].

[46] P. Salières, B. Carré, L. Le Déroff, F. Grasbon, G. G. Paulus, H. Walther, R. Kopold, W. Becker, D. B. Milošević, A. Sanpera, M. Lewenstein, **Feynman's Path-Integral Approach for Intense-Laser-Atom Interactions**, *Science* **292**(5518), 902–905 (2001). [doi:10.1126/science.108836].

[47] M. Murakami, J. Mauritsson, A. L'Huillier, K. J. Schafer, M. B. Gaarde, **Calculation and manipulation of the chirp rates of high-order harmonics**, *Phys. Rev. A* **71**(1), 013410 (2005). [doi:10.1103/PhysRevA.71.013410].

[48] P. Salières, A. L'Huillier, Ph. Antoine, M. Lewenstein, **Study of the Spatial and Temporal Coherence of High-Order Harmonics**, *Adv. At. Mol. Opt. Phys.* **41**, 83–142 (1999). [doi:10.1016/S1049-250X(08)60219-0].

[49] C. Lyngå, M. B. Gaarde, C. Delfin, M. Bellini, T. W. Hänsch, A. L'Huillier, C.-G. Wahlström, **Temporal coherence of high-order harmonics**, *Phys. Rev. A* **60**(6), 4823–4830 (1999). [doi:10.1103/PhysRevA.60.4823].

[50] M. B. Gaarde, J. L. Tate, K. J. Schafer, **Macroscopic aspects of attosecond pulse generation**, *J. Phys. B: At. Mol. Opt. Phys.* **41**(13), 132001 (2008). [doi:10.1088/0953-4075/41/13/132001].

[51] A. Rundquist, C. G. Durfee III, Z. Chang, C. Herne, S. Backus, M. M. Murnane, H. C. Kapteyn, **Phase-Matched Generation of Coherent Soft X-rays**, *Science* **280**(5368), 1412–1415 (1998). [doi:10.1126/science.280.5368.1412].

[52] M. Schnürer, Z. Cheng, S. Sartania, M. Hentschel, G. Tempea, T. Brabec, F. Krausz, **Guiding and high-harmonic generation of sub-10-fs pulses in**

hollow-core fibers at 10^{15} **W/cm^2**, *Appl. Phys. B* **67**(2), 263–266 (1998). [doi:10.1007/s003400050504].

[53] C. G. Durfee III, A. R. Rundquist, S. Backus, C. Herne, M. M. Murnane, H. C. Kapteyn, **Phase Matching of High-Order Harmonics in Hollow Waveguides**, *Phys. Rev. Lett.* **83**(11), 2187–2190 (1999). [doi:10.1103/PhysRevLett.83.2187].

[54] Y. Tamaki, Y. Nagata, M. Obara, K. Midorikawa, **Phase-matched high-order-harmonic generation in a gas-filled hollow fiber**, *Phys. Rev. A* **59**(5), 4041–4044 (1999). [doi:10.1103/PhysRevA.59.4041].

[55] E. Marcatili, R. Schmeltzer, **Hollow Metallic and Dielectric Waveguides for Long Distance Optical Transmission and Lasers**, *Bell Syst. Tech. J.* **43**(4), 1783–1809 (1964).

[56] Y. Tamaki, J. Itatani, Y. Nagata, M. Obara, K. Midorikawa, **Highly Efficient, Phase-Matched High-Harmonic Generation by a Self-Guided Laser Beam**, *Phys. Rev. Lett.* **82**(7), 1422–1425 (1999). [doi:10.1103/PhysRevLett.82.1422].

[57] V. Tosa, E. Takahashi, Y. Nabekawa, K. Midorikawa, **Generation of high-order harmonics in a self-guided beam**, *Phys. Rev. A* **67**(6), 063817 (2003). [doi:10.1103/PhysRevA.67.063817].

[58] M. Nisoli, E. Priori, G. Sansone, S. Stagira, G. Cerullo, S. De Silvestri, C. Altucci, R. Bruzzese, C. de Lisio, P. Villoresi, L. Poletto, M. Pascolini, G. Tondello, **High-Brightness High-Order Harmonic Generation by Truncated Bessel Beams in the Sub-10-fs Regime**, *Phys. Rev. Lett.* **88**(3), 033902 (2002). [doi:10.1103/PhysRevLett.88.033902].

[59] T. Auguste, O. Gobert, B. Carré, **Numerical study on high-order harmonic generation by a Bessel-Gauss laser beam**, *Phys. Rev. A* **78**(3), 033411 (2008). [doi:10.1103/PhysRevA.78.033411].

[60] A. Averchi, D. Faccio, R. Berlasso, M. Kolesik, J. V. Moloney, A. Couairon, P. Di Trapani, **Phase matching with pulsed Bessel beams for high-order harmonic generation**, *Phys. Rev. A* **77**(2), 021802 (2008). [doi:10.1103/PhysRevA.77.021802].

[61] L. V. Dao, K. B. Dinh, P. Hannaford, **Generation of extreme ultraviolet radiation with a Bessel-Gaussian beam**, *Appl. Phys. Lett.* **95**(13) (2009). [doi:10.1063/1.3240404].

[62] E. Constant, D. Garzella, P. Breger, E. Mével, Ch. Dorrer, C. Le Blanc, F. Salin, P. Agostini, **Optimizing High Harmonic Generation in Absorbing Gases: Model and Experiment**, *Phys. Rev. Lett.* **82**(8), 1668–1671 (1999). [doi:10.1103/PhysRevLett.82.1668].

[63] M. Schnürer, Z. Cheng, M. Hentschel, G. Tempea, P. Kálmán, T. Brabec, F. Krausz, **Absorption-Limited Generation of Coherent Ultrashort Soft-X-Ray Pulses**, *Phys. Rev. Lett.* **83**(4), 722–725 (1999). [doi:10.1103/PhysRevLett.83.722].

[64] D. McGloin, K. Dholakia, **Bessel beams: Diffraction in a new light**, *Contemp. Phys.* **46**(1), 15–28 (2005). [doi:10.1080/0010751042000275259].

[65] J. Durnin, J. J. Miceli, J. H. Eberly, **Diffraction-free beams**, *Phys. Rev. Lett.* **58**(15), 1499–1501 (1987). [doi:10.1103/PhysRevLett.58.1499].

[66] F. Gori, G. Guattari, C. Padovani, **Bessel-Gauss beams**, *Opt. Commun.* **64**, 491–495 (1987). [doi:10.1016/0030-4018(87)90276-8].

[67] L. M. Soroko (Ed.), **Meso-optics: foundations and applications** (World Scientific Pub. Co., Singapore, 1996).

[68] R. MacDonald, S. Boothroyd, T. Okamoto, J. Chrostowski, B. Syrett, **Interboard optical data distribution by Bessel beam shadowing**, *Optics Communications* **122**(4–6), 169–177 (1996). [doi:10.1016/0030-4018(95)00432-7].

[69] Z. Bouchal, J. Wagner, M. Chlup, **Self-reconstruction of a distorted nondiffracting beam**, *Opt. Commun.* **151**(4–6), 207–211 (1998). [doi:10.1016/S0030-4018(98)00085-6].

[70] V. Garcés-Chávez, D. McGloin, H. Melville, W. Sibbett, K. Dholakia, **Simultaneous micromanipulation in multiple planes using a self-reconstructing light beam**, *Nature* **419**(6903), 145–147 (2002). [doi:10.1038/nature01007].

[71] F. O. Fahrbach, P. Simon, A. Rohrbach, **Microscopy with self-reconstructing beams**, *Nature Photon.* **4**(11), 780–785 (2010). [doi:10.1038/nphoton.2010.204].

[72] M. A. Porras, G. Valiulis, P. Di Trapani, **Unified description of Bessel X waves with cone dispersion and tilted pulses**, *Phys. Rev. E* **68**, 016613 (2003). [doi:10.1103/PhysRevE.68.016613].

[73] H. E. Hernández-Figueroa, M. Zamboni-Rached, E. Recami (Eds.), **Localized Waves** (Wiley-Interscience, New York, 2008).

[74] J.-Y. Lu, J. F. Greenleaf, **Ultrasonic nondiffracting transducer for medical imaging**, *IEEE Trans. Ultrason. Ferroelectr. Freq. Control* **37**(5), 438–447 (1990). [doi:10.1109/58.105250].

[75] J.-Y. Lu, J. F. Greenleaf, **Nondiffracting X waves-exact solutions to free-space scalar wave equation and their finite aperture realizations**, *IEEE Trans. Ultrason. Ferroelectr. Freq. Control* **39**(1), 19–31 (1992). [doi:10.1109/58.166806].

[76] E. Recami, **On localized "X-shaped" Superluminal solutions to Maxwell equations**, *Physica A* **252**, 586–610 (1998). [doi:10.1016/S0378-4371(97)00686-9].

[77] Z. Liu, D. Fan, **Propagation of pulsed zeroth-order Bessel beams**, *J. Mod. Opt.* **45**(1), 17–21 (1998). [doi:10.1080/09500349808231665].

[78] P. Saari, K. Reivelt, **Evidence of X-Shaped Propagation-Invariant Localized Light Waves**, *Phys. Rev. Lett.* **79**, 4135 (1997). [doi:10.1103/PhysRevLett.79.4135].

[79] F. Bonaretti, D. Faccio, M. Clerici, J. Biegert, P. Di Trapani, **Spatiotemporal Amplitude and Phase Retrieval of Bessel-X pulses using a Hartmann-Shack Sensor**, *Opt. Express* **17**(12), 9804–9809 (2009). [doi:10.1364/OE.17.009804].

[80] P. Bowlan, H. Valtna-Lukner, M. Lõhmus, P. Piksarv, P. Saari, R. Trebino, **Measuring the spatiotemporal field of ultrashort Bessel-X pulses**, *Opt. Lett.* **34**, 2276 (2009). [doi:10.1364/OL.34.002276].

[81] O. E. Martinez, **Pulse distortions in tilted pulse schemes for ultrashort pulses**, *Opt. Commun.* **59**(3), 229–232 (1986). [doi:10.1016/0030-4018(86)90290-7].

[82] S. Akturk, X. Gu, E. Zeek, R. Trebino, **Pulse-front tilt caused by spatial and temporal chirp**, *Opt. Express* **12**(19), 4399–4410 (2004). [doi:10.1364/OPEX.12.004399].

[83] S. Akturk, X. Gu, P. Gabolde, R. Trebino, **The general theory of first-order spatio-temporal distortions of Gaussian pulses and beams**, *Opt. Express* **13**(21), 8642–8661 (2005). [doi:10.1364/OPEX.13.008642].

[84] I. Alexeev, K. Y. Kim, H. M. Milchberg, **Measurement of the Superluminal Group Velocity of an Ultrashort Bessel Beam Pulse**, *Phys. Rev. Lett.* **88**(7), 073901 (2002). [doi:10.1103/PhysRevLett.88.073901].

[85] C. J. Zapata-Rodríguez, M. A. Porras, **X-wave bullets with negative group velocity in vacuum**, *Opt. Lett.* **31**(23), 3532–3534 (2006). [doi:10.1364/OL.31.003532].

[86] M. A. Porras, P. Di Trapani, **Localized and stationary light wave modes in dispersive media**, *Phys. Rev. E* **69**(6), 066606 (2004). [doi:10.1103/PhysRevE.69.066606].

[87] S. Longhi, **Localized subluminal envelope pulses in dispersive media**, *Opt. Lett.* **29**(2), 147–149 (2004). [doi:10.1364/OL.29.000147].

[88] S. Malaguti, S. Trillo, **Envelope localized waves of the conical type in linear normally dispersive media**, *Phys. Rev. A* **79**, 063803 (2009). [doi:10.1103/PhysRevA.79.063803].

[89] J. H. McLeod, **The Axicon: A New Type of Optical Element**, *J. Opt. Soc. Am.* **44**(8), 592–592 (1954). [doi:10.1364/JOSA.44.000592].

[90] J. H. McLeod, **Axicons and Their Uses**, *J. Opt. Soc. Am.* **50**(2), 166–166 (1960). [doi:10.1364/JOSA.50.000166].

[91] A. Vasara, J. Turunen, A. T. Friberg, **Realization of general nondiffracting beams with computer-generated holograms**, *J. Opt. Soc. Am. A* **6**(11), 1748–1754 (1989). [doi:10.1364/JOSAA.6.001748].

[92] J. A. Davis, E. Carcole, D. M. Cottrell, **Nondiffracting interference patterns generated with programmable spatial light modulators**, *Appl. Opt.* **35**(4), 599–602 (1996). [doi:10.1364/AO.35.000599].

[93] J. Leach, G. M. Gibson, M. J. Padgett, E. Esposito, G. McConnell, A. J. Wright, J. M. Girkin, **Generation of achromatic Bessel beams using a compensated spatial light modulator**, *Opt. Express* **14**(12), 5581–5587 (2006). [doi:10.1364/OE.14.005581].

[94] M. Clerici, O. Jedrkiewicz, E. Rubino, D. Faccio, L. Tartara, V. Degiorgio, P. Di Trapani, **Generation and amplification of pulsed Bessel beams by seeding an optical parametric amplifier**, *Opt. Lett.* **33**(20), 2296–2298 (2008). [doi:10.1364/OL.33.002296].

[95] M. Kolesik, E. M. Wright, J. V. Moloney, **Dynamic nonlinear X waves for femtosecond pulse propagation in water**, *Phys. Rev. Lett.* **92**(25), 253901 (2004). [doi:10.1103/PhysRevLett.92.253901].

[96] D. Faccio, M. Porras, A. Dubietis, F. Bragheri, A. Couairon, P. Di Trapani, **Conical emission, pulse splitting and X-wave parametric amplification in nonlinear dynamics of ultrashort light pulses**, *Phys. Rev. Lett.* **96**(19), 193901 (2006). [doi:10.1103/PhysRevLett.96.193901].

[97] A. Couairon, E. Gaižauskas, D. Faccio, A. Dubietis, P. Di Trapani, **Nonlinear X-wave formation by femtosecond filamentation in Kerr media**, *Phys. Rev. E* **73**(1), 016608 (2006). [doi:10.1103/PhysRevE.73.016608].

[98] D. Faccio, A. Lotti, M. Kolesik, J. V. Moloney, S. Tzortzakis, A. Couairon, P. Di Trapani, **Spontaneous emergence of pulses with constant carrier-envelope phase in femtosecond filamentation**, *Opt. Express* **16**(15), 11103–11114 (2008). [doi:10.1364/OE.16.011103].

[99] D. Faccio, A. Couairon, P. Di Trapani, **Conical Waves, Filaments and Nonlinear Filamentation Optics** (Aracne Editrice, Roma, 2007).

[100] A. Averchi, D. Faccio, E. Rubino, H. Valtna Lukner, P. Panagiotopoulos, P. A. Loukakos, S. Tzortzakis, A. Couairon, P. Di Trapani, **Linear X-wave generation by means of cross-phase modulation in Kerr media**, *Opt. Lett.* **33**(24), 3028–3030 (2008). [doi:10.1364/OL.33.003028].

[101] D. Faccio, A. Averchi, A. Couairon, M. Kolesik, J. V. Moloney, A. Dubietis, G. Tamosauskas, P. Polesana, A. Piskarskas, P. Di Trapani, **Spatio-temporal reshaping and X Wave dynamics in optical filaments**, *Opt. Express* **15**(20), 13077–13095 (2007). [doi:10.1364/OE.15.013077].

[102] A. Braun, G. Korn, X. Liu, D. Du, J. Squier, G. Mourou, **Self-channeling of high-peak-power femtosecond laser pulses in air**, *Opt. Lett.* **20**(1), 73–75 (1995). [doi:10.1364/OL.20.000073].

[103] E. Garmire, R. Y. Chiao, C. H. Townes, **Dynamics and Characteristics of the Self-Trapping of Intense Light Beams**, *Phys. Rev. Lett.* **16**(9), 347–349 (1966). [doi:10.1103/PhysRevLett.16.347].

[104] V. V. Korobkin, R. V. Serov, **Investigation of Self-focusing of Neodymium-laser Radiation**, *JETP Lett.* **6**(5), 135–137 (1967).

[105] J. Reintjes, R. L. Carman, F. Shimizu, **Study of Self-Focusing and Self-Phase-Modulation in the Picosecond-Time Regime**, *Phys. Rev. A* **8**(3), 1486–1503 (1973). [doi:10.1103/PhysRevA.8.1486].

[106] S. Tzortzakis, L. Sudrie, M. Franco, B. Prade, A. Mysyrowicz, A. Couairon, L. Bergé, **Self-Guided Propagation of Ultrashort IR Laser Pulses in Fused Silica**, *Phys. Rev. Lett.* **87**(21), 213902 (2001). [doi:10.1103/PhysRevLett.87.213902].

[107] M. Kolesik, J. V. Moloney, **Self-healing femtosecond light filaments**, *Opt. Lett.* **29**(6), 590–592 (2004). [doi:10.1364/OL.29.000590].

[108] A. Dubietis, E. Kučinskas, G. Tamošauskas, E. Gaižauskas, M. A. Porras, P. Di Trapani, **Self-reconstruction of light filaments**, *Opt. Lett.* **29**(24), 2893–2895 (2004). [doi:10.1364/OL.29.002893].

[109] W. Liu, J.-F. Gravel, F. Théberge, A. Becker, S. L. Chin, **Background reservoir: its crucial role for long-distance propagation of femtosecond laser pulses in air**, *Appl. Phys. B* **80**(7), 857–860 (2005). [doi:10.1007/s00340-005-1805-6].

[110] A. Dubietis, E. Gaižauskas, G. Tamošauskas, P. Di Trapani, **Light filaments without self-channeling**, *Phys. Rev. Lett.* **92**(25), 253903 (2004). [doi:10.1103/PhysRevLett.92.253903].

[111] F. Courvoisier, V. Boutou, J. Kasparian, E. Salmon, G. Méjean, J. Yu, J.-P. Wolf, **Ultraintense light filaments transmitted through clouds**, *Appl. Phys. Lett.* **83**(2), 213–215 (2003). [doi:10.1063/1.1592615].

[112] G. Méjean, J. Kasparian, J. Yu, E. Salmon, S. Frey, J.-P. Wolf, S. Skupin, A. Vinçotte, R. Nuter, S. Champeaux, L. Bergé, **Multifilamentation transmission through fog**, *Phys. Rev. E* **72**(2), 026611 (2005). [doi:10.1103/PhysRevE.72.026611].

[113] J. M. Dudley, J. R. Taylor, **Supercontinuum generation in optical fibers** (Cambridge University Press, Cambridge, England, 2010).

[114] J. Kasparian, J.-P. Wolf, **Physics and applications of atmospheric nonlinear optics and filamentation**, *Opt. Express* **16**(1), 466–493 (2008). [doi:10.1364/OE.16.000466].

[115] C. P. Hauri, W. Kornelis, F. W. Helbing, A. Heinrich, A. Couairon, A. Mysyrowicz, J. Biegert, U. Keller, **Generation of intense, carrier-envelope phase-locked few-cycle laser pulses through filamentation**, *Appl. Phys. B* **79**(6), 673–677 (2004). [doi:10.1007/s00340-004-1650-z].

[116] A. Zaïr, A. Guandalini, F. Schapper, M. Holler, J. Biegert, L. Gallmann, A. Couairon, M. Franco, A. Mysyrowicz, U. Keller, **Spatio-temporal**

characterization of few-cycle pulses obtained by filamentation, *Opt. Express* **15**(9), 5394–5404 (2007). [doi:10.1364/OE.15.005394].

[117] J. Kasparian, P. Béjot, J.-P. Wolf, J. M. Dudley, **Optical rogue wave statistics in laser filamentation**, *Opt. Express* **17**(14), 12070–12075 (2009). [doi:10.1364/OE.17.012070].

[118] D. Majus, V. Jukna, G. Valiulis, D. Faccio, A. Dubietis, **Spatiotemporal rogue events in femtosecond filamentation**, *Phys. Rev. A* **83**(2), 025802 (2011). [doi:10.1103/PhysRevA.83.025802].

[119] K. Dysthe, H. E. Krogstad, P. Müller, **Oceanic Rogue Waves**, *Annu. Rev. Fluid Mech.* **40**(1), 287–310 (2008). [doi:10.1146/annurev.fluid.40.111406.102203].

[120] D. R. Solli, C. Ropers, P. Koonath, B. Jalali, **Optical rogue waves**, *Nature* **450**(7172), 1054–1057 (2007). [doi:10.1038/nature06402].

[121] M. Erkintalo, G. Genty, J. M. Dudley, **Rogue-wave-like characteristics in femtosecond supercontinuum generation**, *Opt. Lett.* **34**(16), 2468–2470 (2009). [doi:10.1364/OL.34.002468].

[122] P. Di Trapani, G. Valiulis, A. Piskarskas, O. Jedrkiewicz, J. Trull, C. Conti, S. Trillo, **Spontaneously generated X-shaped light bullets**, *Phys. Rev. Lett.* **91**(9), 093904 (2003). [doi:10.1103/PhysRevLett.91.093904].

[123] S. L. Chin, S. A. Hosseini, W. Liu, Q. Luo, F. Théberge, N. Aközbek, A. Becker, V. P. Kandidov, O. G. Kosareva, H. Schroeder, **The propagation of powerful femtosecond laser pulses in optical media: physics, applications, and new challenges**, *Can. J. Phys.* **83**(9), 863–905 (2005). [doi:10.1139/p05-048].

[124] E. T. J. Nibbering, P. F. Curley, G. Grillon, B. S. Prade, M. A. Franco, F. Salin, A. Mysyrowicz, **Conical emission from self-guided femtosecond pulses in air**, *Opt. Lett.* **21**(1), 62–65 (1996). [doi:10.1364/OL.21.000062].

[125] A. Couairon, J. Biegert, C. P. Hauri, W. Kornelis, F. W. Helbing, U. Keller, A. Mysyrowicz, **Self-compression of ultra-short laser pulses down to one optical cycle by filamentation**, *J. Mod. Opt.* **53**(1-2), 75–85 (2006). [doi:10.1080/09500340500227760].

[126] M. B. Gaarde, A. Couairon, **Intensity Spikes in Laser Filamentation: Diagnostics and Application**, *Phys. Rev. Lett.* **103**(4), 043901 (2009). [doi:10.1103/PhysRevLett.103.043901].

[127] B. Prade, M. Franco, A. Mysyrowicz, A. Couairon, H. Buersing, B. Eberle, M. Krenz, D. Seiffer, O. Vasseur, **Spatial mode cleaning by femtosecond filamentation in air**, *Opt. Lett.* **31**(17), 2601–2603 (2006). [doi:10.1364/OL.31.002601].

[128] X. M. Zhao, J.-C. Diels, C. Y. Wang, J. M. Elizondo, **Femtosecond ultraviolet laser pulse induced lightning discharges in gases**, *IEEE J. Quantum Electron.* **31**(3), 599–612 (1995). [doi:10.1109/3.364418].

[129] S. Tzortzakis, B. Prade, M. Franco, A. Mysyrowicz, S. Hüller, P. Mora, **Femtosecond laser-guided electric discharge in air**, *Phys. Rev. E* **64**(5), 057401 (2001). [doi:10.1103/PhysRevE.64.057401].

[130] G. Méchain, A. Mysyrowicz, M. Depiesse, M. Pellet, **A virtual antenna produced in air by intense femtosecond laser pulses**. In *Technologies for Optical Countermeasures II; Femtosecond Phenomena II; and Passive Millimetre-Wave and Terahertz Imaging II* (Edited by D. H. Titterton, S. M. Kirkpatrick, R. Stoian, R. Appleby, J. M. Chamberlain, K. A. Krapels), vol. 5989, 59890S (SPIE, Bellingham, Washington, 2005). [doi:10.1117/12.631202].

[131] S. Tzortzakis, G. Méchain, G. Patalano, Y.-B. André, B. Prade, M. Franco, A. Mysyrowicz, J.-M. Munier, M. Gheudin, G. Beaudin, P. Encrenaz, **Coherent subterahertz radiation from femtosecond infrared filaments in air**, *Opt. Lett.* **27**(21), 1944–1946 (2002). [doi:10.1364/OL.27.001944].

[132] C. D'Amico, A. Houard, M. Franco, B. Prade, A. Mysyrowicz, **Coherent and incoherent radial THz radiation emission from femtosecond filaments in air**, *Opt. Express* **15**(23), 15274–15279 (2007). [doi:10.1364/OE.15.015274].

[133] C. D'Amico, A. Houard, S. Akturk, Y. Liu, J. Le Bloas, M. Franco, B. Prade, A. Couairon, V. T. Tikhonchuk, A. Mysyrowicz, **Forward THz radiation emission by femtosecond filamentation in gases: theory and experiment**, *New J. Phys.* **10**(1), 013015 (2008). [doi:10.1088/1367-2630/10/1/013015].

[134] R. Y. Chiao, E. Garmire, C. H. Townes, **Self-Trapping of Optical Beams**, *Phys. Rev. Lett.* **13**(15), 479–482 (1964). [doi:10.1103/PhysRevLett.13.479].

[135] Y. R. Shen, **The Principles of Nonlinear Optics** (Wiley-Interscience, New York, 1984).

[136] A. Brodeur, C. Y. Chien, F. A. Ilkov, S. L. Chin, O. G. Kosareva, V. P. Kandidov, **Moving focus in the propagation of ultrashort laser pulses in air**, *Opt. Lett.* **22**(5), 304–306 (1997). [doi:10.1364/OL.22.000304].

[137] A. Couairon, **Light bullets from femtosecond filamentation**, *Eur. Phys. J. D* **27**(2), 159–167 (2003). [doi:10.1140/epjd/e2003-00255-9].

[138] D. Faccio, P. Di Trapani, S. Minardi, A. Bramati, F. Bragheri, C. Liberale, V. Degiorgio, A. Dubietis, A. Matijosius, **Far-field spectral characterization of conical emission and filamentation in Kerr media**, *J. Opt. Soc. Am. B* **22**(4), 862–869 (2005). [doi:10.1364/JOSAB.22.000862].

[139] D. Faccio, A. Matijosius, A. Dubietis, R. Piskarskas, A. Varanavičius, E. Gaižauskas, A. Piskarskas, A. Couairon, P. Di Trapani, **Near- and far-field evolution of laser pulse filaments in Kerr media**, *Phys. Rev. E* **72**, 037601 (2005). [doi:10.1103/PhysRevE.72.037601].

[140] M. A. Porras, A. Parola, D. Faccio, A. Dubietis, P. Di Trapani, **Non-linear Unbalanced Bessel Beams: stationary conical waves supported by nonlinear losses**, *Phys. Rev. Lett.* **93**(15), 153902 (2004). [doi:10.1103/PhysRevLett.93.153902].

[141] C. Conti, **Generation and dynamics of X waves of the Schrödinger equation**, *Phys. Rev. E* **70**(4), 046613 (2004). [doi:10.1103/PhysRevE.70.046613].

[142] M. A. Porras, A. Parola, P. Di Trapani, **Nonlinear unbalanced O waves: nonsolitary, conical light bullets in nonlinear dissipative media**, *J. Opt. Soc. Am. B* **22**(7), 1406–1413 (2005). [doi:10.1364/JOSAB.22.001406].

[143] F. Bragheri, D. Faccio, F. Bonaretti, A. Lotti, M. Clerici, O. Jedrkiewicz, C. Liberale, S. Henin, L. Tartara, V. Degiorgio, P. Di Trapani, **Complete retrieval of the field of ultrashort optical pulses using the angle-frequency spectrum**, *Opt. Lett.* **33**(24), 2952 (2008). [doi:10.1364/OL.33.002952].

[144] D. Faccio, A. Lotti, A. Matijosius, F. Bragheri, V. Degiorgio, A. Couairon, P. Di Trapani, **Experimental energy-density flux characterization of ultrashort laser pulse filaments**, *Opt. Express* **17**(10), 8193–8200 (2009). [doi:10.1364/OE.17.008193].

[145] P. Bowlan, P. Gabolde, A. Shreenath, K. McGresham, R. Trebino, S. Akturk, **Crossed-beam spectral interferometry: a simple, high-spectral-resolution method for completely characterizing complex ultrashort pulses in real time**, *Opt. Express* **14**(24), 11892–11900 (2006). [doi:10.1364/OE.14.011892].

[146] P. Bowlan, U. Fuchs, R. Trebino, U. Zeitner, **Measuring the spatiotemporal electric field of tightly focused ultrashort pulses with submicron spatial resolution**, *Opt. Express* **16**(18), 13663–13675 (2008). [doi:10.1364/OE.16.013663].

[147] H. S. Green, E. Wolf, **A Scalar Representation of Electromagnetic Fields**, *Proc. Phys. Soc. A* **66**(12), 1129 (1953). [doi:10.1088/0370-1298/66/12/308].

[148] E. Wolf, **A Scalar Representation of Electromagnetic Fields: II**, *Proc. Phys. Soc.* **74**(3), 269 (1959). [doi:10.1088/0370-1328/74/3/305].

[149] P. Roman, **A Scalar Representation of Electromagnetic Fields: III**, *Proc. Phys. Soc.* **74**(3), 281 (1959). [doi:10.1088/0370-1328/74/3/306].

[150] L. Allen, M. J. Padgett, M. Babiker, **The orbital angular momentum of light**, *Prog. Opt.* **39**, 291–372 (1999). [doi:10.1016/S0079-6638(08)70391-3].

[151] H. Sztul, R. Alfano, **The Poynting vector and angular momentum of Airy beams**, *Opt. Express* **16**(13), 9411–9416 (2008). [doi:10.1364/OE.16.009411].

[152] A. Dubietis, A. Couairon, E. Kučinskas, G. Tamošauskas, E. Gaižauskas, D. Faccio, P. Di Trapani, **Measurement and calculation of nonlinear absorption associated with femtosecond filaments in water**, *Appl. Phys. B* **84**, 439–446 (2006). [doi:10.1007/s00340-006-2249-3].

[153] P. Polesana, M. Franco, A. Couairon, D. Faccio, P. Di Trapani, **Filamentation in Kerr media from pulsed Bessel beams**, *Phys. Rev. A* **77**, 043814 (2008). [doi:10.1103/PhysRevA.77.043814].

[154] A. G. Van Engen, S. A. Diddams, T. S. Clement, **Dispersion Measurements of Water with White-Light Interferometry**, *Appl. Opt.* **37**(24), 5679–5686 (1998). [doi:10.1364/AO.37.005679].

[155] S. Malaguti, G. Bellanca, S. Trillo, **Two-dimensional envelope localized waves in the anomalous dispersion regime**, *Opt. Lett.* **33**(10), 1117–1119 (2008). [doi:10.1364/OL.33.001117].

[156] R. Trebino, D. J. Kane, **Using phase retrieval to measure the intensity and phase of ultrashort pulses: frequency-resolved optical gating**, *J. Opt. Soc. Am. A* **10**(5), 1101–1111 (1993). [doi:10.1364/JOSAA.10.001101].

[157] B. C. Platt, R. V. Shack, **Lenticular Hartmann-screen**, *Opt. Sci. Cent. Newsl.* **5**, 15–16 (1971).

[158] E. Rubino, D. Faccio, L. Tartara, P. K. Bates, O. Chalus, M. Clerici, F. Bonaretti, J. Biegert, P. Di Trapani, **Spatiotemporal amplitude and phase retrieval of space-time coupled ultrashort pulses using the Shackled-FROG technique**, *Opt. Lett.* **34**(24), 3854–3856 (2009). [doi:10.1364/OL.34.003854].

[159] C. P. Hauri, J. Biegert, U. Keller, B. Schaefer, K. Mann, G. Marowski, **Validity of wave-front reconstruction and propagation of ultrabroadband pulses measured with a Hartmann-Shack sensor**, *Opt. Lett.* **30**(12), 1563–1565 (2005). [doi:10.1364/OL.30.001563].

[160] M. A. C. Potenza, S. Minardi, J. Trull, G. Blasi, D. Salerno, P. Di Trapani, A. Varanavičius, A. Piskarskas, **Three dimensional imaging of short pulses**, *Opt. Commun.* **229**, 381–390 (2004). [doi:10.1016/j.optcom.2003.10.029].

[161] J. R. Fienup, **Phase retrieval algorithms: a comparison**, *Appl. Opt.* **21**(15), 2758–2769 (1982). [doi:10.1364/AO.21.002758].

[162] C. Conti, S. Trillo, P. Di Trapani, G. Valiulis, A. Piskarskas, O. Jedrkiewicz, J. Trull, **Nonlinear electromagnetic X waves**, *Phys. Rev. Lett.* **90**(17), 170406 (2003). [doi:10.1103/PhysRevLett.90.170406].

[163] W. H. Press, S. A. Teukolsky, W. T. Vetterling, B. P. Flannery, **Numerical Recipes in C: the Art of Scientific Computing, Second Edition** (Cambridge University Press, Cambridge, England, 1992).

[164] A. Bideau-Mehu, Y. Guern, R. Abjean, A. Johannin-Gilles, **Measurement of refractive indices of neon, argon, krypton and xenon in the 253.7-140.4 nm wavelength range. Dispersion relations and estimated oscillator strengths of the resonance lines**, *J. Quant. Spectrosc. Radiat. Transfer* **25**(5), 395–402 (1981). [doi:10.1016/0022-4073(81)90057-1].

[165] D. P. Shelton, **Nonlinear-optical susceptibilities of gases measured at 1064 and 1319 nm**, *Phys. Rev. A* **42**(5), 2578–2592 (1990). [doi:10.1103/PhysRevA.42.2578].

[166] A. Couairon, H. S. Chakraborty, M. B. Gaarde, **From single-cycle self-compressed filaments to isolated attosecond pulses in noble gases**, *Phys. Rev. A* **77**(5), 053814 (2008). [doi:10.1103/PhysRevA.77.053814].

[167] A. L. Gaeta, **Catastrophic Collapse of Ultrashort Pulses**, *Phys. Rev. Lett.* **84**(16), 3582–3585 (2000). [doi:10.1103/PhysRevLett.84.3582].

[168] A. H. Zewail, **Femtochemistry: Atomic-Scale Dynamics of the Chemical Bond**, *J. Phys. Chem. A* **104**(24), 5660–5694 (2000). [doi:10.1021/jp001460h].

[169] F. Remacle, R. Kienberger, F. Krausz, R. Levine, **On the feasibility of an ultrafast purely electronic reorganization in lithium hydride**, *Chem. Phys.* **338**(2–3), 342–347 (2007). [doi:10.1016/j.chemphys.2007.05.012].

[170] F. Remacle, M. Nest, R. D. Levine, **Laser Steered Ultrafast Quantum Dynamics of Electrons in LiH**, *Phys. Rev. Lett.* **99**(18), 183902 (2007). [doi:10.1103/PhysRevLett.99.183902].

[171] R. M. Bowman, J. J. Gerdy, G. Roberts, A. H. Zewail, **Femtosecond real-time probing of reactions. 6. A joint experimental and theoretical study of bismuth dimer dissociation**, *J. Phys. Chem.* **95**(12), 4635–4647 (1991). [doi:10.1021/j100165a011].

[172] T. Nagy, P. Simon, **Generation of 200-μJ, sub-25-fs deep-UV pulses using a noble-gas-filled hollow fiber**, *Opt. Lett.* **34**(15), 2300–2302 (2009). [doi:10.1364/OL.34.002300].

[173] S. Backus, J. Peatross, Z. Zeek, A. Rundquist, G. Taft, M. M. Murnane, H. C. Kapteyn, **16-fs, 1-μJ ultraviolet pulses generated by third-harmonic conversion in air**, *Opt. Lett.* **21**(9), 665–667 (1996). [doi:10.1364/OL.21.000665].

[174] U. Graf, M. Fieß, M. Schultze, R. Kienberger, F. Krausz, E. Goulielmakis, **Intense few-cycle light pulses in the deep ultraviolet**, *Opt. Express* **16**(23), 18956–18963 (2008). [doi:10.1364/OE.16.018956].

[175] F. Reiter, U. Graf, M. Schultze, W. Schweinberger, H. Schröder, N. Karpowicz, A. M. Azzeer, R. Kienberger, F. Krausz, E. Goulielmakis, **Generation of sub-3 fs pulses in the deep ultraviolet**, *Opt. Lett.* **35**(13), 2248–2250 (2010). [doi:10.1364/OL.35.002248].

[176] C. G. Durfee III, S. Backus, H. C. Kapteyn, M. M. Murnane, **Intense 8-fs pulse generation in the deep ultraviolet**, *Opt. Lett.* **24**(10), 697–699 (1999). [doi:10.1364/OL.24.000697].

[177] T. Fuji, T. Suzuki, E. E. Serebryannikov, A. Zheltikov, **Experimental and theoretical investigation of a multicolor filament**, *Phys. Rev. A* **80**(6), 063822 (2009). [doi:10.1103/PhysRevA.80.063822].

[178] S. Trushin, W. Fuss, K. Kosma, W. Schmid, **Widely tunable ultraviolet sub-30-fs pulses from supercontinuum for transient spectroscopy**, *Appl. Phys. B* **85**(1), 1–5 (2006). [doi:10.1007/s00340-006-2416-6].

[179] S. A. Trushin, K. Kosma, W. Fuß, W. E. Schmid, **Sub-10-fs supercontinuum radiation generated by filamentation of few-cycle 800 nm pulses in argon**, *Opt. Lett.* **32**(16), 2432–2434 (2007). [doi:10.1364/OL.32.002432].

[180] F. Reiter, U. Graf, E. E. Serebryannikov, W. Schweinberger, M. Fiess, M. Schultze, A. M. Azzeer, R. Kienberger, F. Krausz, A. M. Zheltikov, E. Goulielmakis, **Route to Attosecond Nonlinear Spectroscopy**, *Phys. Rev. Lett.* **105**(24), 243902 (2010). [doi:10.1103/PhysRevLett.105.243902].

[181] E. E. Serebryannikov, E. Goulielmakis, A. M. Zheltikov, **Generation of supercontinuum compressible to single-cycle pulse widths in an ionizing gas**, *New J. Phys.* **10**(9), 093001 (2008). [doi:10.1088/1367-2630/10/9/093001].

[182] *CXRO - Center for X-Ray Optics*, Lawrence Berkeley National Laboratory, `http://www.cxro.lbl.gov/`.

[183] Z. L. Horváth, J. Vinkó, Z. Bor, D. von der Linde, **Acceleration of femtosecond pulses to superluminal velocities by Gouy phase shift**, *Appl. Phys. B* **63**(5), 481–484 (1996). [doi:10.1007/BF01828944].

[184] M. B. Gaarde, K. J. Schafer, **Generating single attosecond pulses via spatial filtering**, *Opt. Lett.* **31**(21), 3188–3190 (2006). [doi:10.1364/OL.31.003188].

[185] C. A. Haworth, L. E. Chipperfield, J. S. Robinson, P. L. Knight, J. P. Marangos, J. W. G. Tisch, **Half-cycle cutoffs in harmonic spectra and robust carrier-envelope phase retrieval**, *Nat. Phys.* **3**(1), 52–57 (2007). [doi:10.1038/nphys463].

[186] M. J. Abel, T. Pfeifer, P. M. Nagel, W. Boutu, M. J. Bell, C. P. Steiner, D. M. Neumark, S. R. Leone, **Isolated attosecond pulses from ionization gating of high-harmonic emission**, *Chem. Phys.* **366**, 9–14 (2009). [doi:10.1016/j.chemphys.2009.09.016].

[187] M. B. Gaarde, **Time-frequency representations of high order harmonics**, *Opt. Express* **8**(10), 529–536 (2001). [doi:10.1364/OE.8.000529].

[188] Ph. Balcou, A. L'Huillier, **Phase-matching effects in strong-field harmonic generation**, *Phys. Rev. A* **47**(2), 1447–1459 (1993). [doi:10.1103/PhysRevA.47.1447].

[189] C. Altucci, R. Bruzzese, C. de Lisio, M. Nisoli, E. Priori, S. Stagira, M. Pascolini, L. Poletto, P. Villoresi, V. Tosa, K. Midorikawa, **Phase-matching analysis of high-order harmonics generated by truncated Bessel beams in the sub-10-fs regime**, *Phys. Rev. A* **68**(3), 033806 (2003). [doi:10.1103/PhysRevA.68.033806].

[190] Ph. Balcou, P. Salières, A. L'Huillier, M. Lewenstein, **Generalized phase-matching conditions for high harmonics: The role of field-gradient forces**, *Phys. Rev. A* **55**(4), 3204–3210 (1997). [doi:10.1103/PhysRevA.55.3204].

[191] D. S. Steingrube, E. Schulz, T. Binhammer, M. B. Gaarde, A. Couairon, U. Morgner, M. Kovačev, **High-order harmonic generation directly from a filament**, *New J. Phys.* **13**(4), 043022 (2011). [doi:10.1088/1367-2630/13/4/043022].

[192] J. C. Painter, M. Adams, N. Brimhall, E. Christensen, G. Giraud, N. Powers, M. Turner, M. Ware, J. Peatross, **Direct observation of laser filamentation in high-order harmonic generation**, *Opt. Lett.* **31**(23), 3471–3473 (2006). [doi:10.1364/OL.31.003471].

[193] H. S. Chakraborty, M. B. Gaarde, A. Couairon, **Single attosecond pulses from high harmonics driven by self-compressed filaments**, *Opt. Lett.* **31**(24), 3662–3664 (2006). [doi:10.1364/OL.31.003662].

[194] J. Itatani, J. Levesque, D. Zeidler, H. Niikura, H. Pépin, J. C. Kieffer, P. B. Corkum, D. M. Villeneuve, **Tomographic imaging of molecular orbitals**, *Nature* **432**(7019), 867–871 (2004). [doi:10.1038/nature03183].

[195] E. Goulielmakis, Z.-H. Loh, A. Wirth, R. Santra, N. Rohringer, V. S. Yakovlev, S. Zherebtsov, T. Pfeifer, A. M. Azzeer, M. F. Kling, S. R. Leone, F. Krausz, **Real-time observation of valence electron motion**, *Nature* **466**(7307), 739–743 (2010). [doi:10.1038/nature09212].

[196] M. Drescher, M. Hentschel, R. Kienberger, M. Uiberacker, V. Yakovlev, A. Scrinzi, Th. Westerwalbesloh, U. Kleineberg, U. Heinzmann, F. Krausz, **Time-resolved atomic inner-shell spectroscopy**, *Nature* **419**(6909), 803–807 (2002). [doi:10.1038/nature01143].

[197] A. L. Cavalieri, N. Müller, Th. Uphues, V. S. Yakovlev, A. Baltuška, B. Horvath, B. Schmidt, L. Blümel, R. Holzwarth, S. Hendel, M. Drescher, U. Kleineberg, P. M. Echenique, R. Kienberger, F. Krausz, U. Heinzmann, **Attosecond spectroscopy in condensed matter**, *Nature* **449**(7165), 1029–1032 (2007). [doi:10.1038/nature06229].

[198] A. Zaïr, M. Holler, A. Guandalini, F. Schapper, J. Biegert, L. Gallmann, U. Keller, A. S. Wyatt, A. Monmayrant, I. A. Walmsley, E. Cormier, T. Auguste, J. P. Caumes, P. Salières, **Quantum Path Interferences in High-Order Harmonic Generation**, *Phys. Rev. Lett.* **100**(14), 143902 (2008). [doi:10.1103/PhysRevLett.100.143902].

[199] H. Xu, H. Xiong, Z. Zeng, Y. Fu, J. Yao, R. Li, Y. Cheng, Z. Xu, **Fine interference fringes formed in high-order harmonic spectra generated by infrared driving laser pulses**, *Phys. Rev. A* **78**(3), 033841 (2008). [doi:10.1103/PhysRevA.78.033841].

[200] E. Brunetti, R. Issac, D. A. Jaroszynski, **Quantum path contribution to high-order harmonic spectra**, *Phys. Rev. A* **77**(2), 023422 (2008). [doi:10.1103/PhysRevA.77.023422].

[201] M. Holler, A. Zaïr, F. Schapper, T. Auguste, E. Cormier, A. Wyatt, A. Monmayrant, I. A. Walmsley, L. Gallmann, P. Salières, U. Keller, **Ionization effects on spectral signatures of quantum-path interference in high-harmonic generation**, *Opt. Express* **17**(7), 5716–5722 (2009). [doi:10.1364/OE.17.005716].

[202] F. Schapper, M. Holler, T. Auguste, A. Zaïr, M. Weger, P. Salières, L. Gallmann, U. Keller, **Spatial fingerprint of quantum path interferences in high order harmonic generation**, *Opt. Express* **18**(3), 2987–2994 (2010). [doi:10.1364/OE.18.002987].

[203] P. D. Maker, R. W. Terhune, M. Nisenoff, C. M. Savage, **Effects of Dispersion and Focusing on the Production of Optical Harmonics**, *Phys. Rev. Lett.* **8**(1), 21–22 (1962). [doi:10.1103/PhysRevLett.8.21].

[204] S. Kazamias, D. Douillet, F. Weihe, C. Valentin, A. Rousse, S. Sebban, G. Grillon, F. Augé, D. Hulin, P. Balcou, **Global Optimization of High Harmonic Generation**, *Phys. Rev. Lett.* **90**(19), 193901 (2003). [doi:10.1103/PhysRevLett.90.193901].

[205] C. M. Heyl, J. Güdde, U. Höfer, A. L'Huillier, **Spectrally Resolved Maker Fringes in High-Order Harmonic Generation**, *Phys. Rev. Lett.* **107**(3), 033903 (2011). [doi:10.1103/PhysRevLett.107.033903].

[206] M. V. Berry, N. L. Balazs, **Nonspreading wave packets**, *Am. J. Phys.* **47**(3), 264–267 (1979). [doi:10.1119/1.11855].

[207] A. Chong, W. H. Renninger, D. N. Christodoulides, F. W. Wise, **Airy-Bessel wave packets as versatile linear light bullets**, *Nature Photon.* **4**(2), 103–106 (2009). [doi:10.1038/nphoton.2009.264].

[208] G. A. Siviloglou, J. Broky, A. Dogariu, D. N. Christodoulides, **Ballistic dynamics of Airy beams**, *Opt. Lett.* **33**(3), 207–209 (2008). [doi:10.1364/OL.33.000207].

[209] J. Baumgartl, M. Mazilu, K. Dholakia, **Optically mediated particle clearing using Airy wavepackets**, *Nature Photon.* **2**(11), 675–678 (2008). [doi:10.1038/nphoton.2008.201].

[210] P. Polynkin, M. Kolesik, J. V. Moloney, G. A. Siviloglou, D. N. Christodoulides, **Curved Plasma Channel Generation Using Ultraintense Airy Beams**, *Science* **324**(5924), 229–232 (2009). [doi:10.1126/science.1169544].

[211] M. Abramowitz, I. A. Stegun (Eds.), **Handbook of Mathematical Functions with Formulas, Graphs, and Mathematical Tables** (Dover Publications, New York, 1972).

[212] P. Polesana, A. Dubietis, M. A. Porras, E. Kučinskas, D. Faccio, A. Couairon, P. Di Trapani, **Near-field dynamics of ultrashort pulsed Bessel beams in media with Kerr nonlinearity**, *Phys. Rev. E* **73**(5), 056612 (2006). [doi:10.1103/PhysRevE.73.056612].

[213] J. A. Giannini, R. I. Joseph, **The role of the second Painlevé transcendent in nonlinear optics**, *Phys. Lett. A* **141**(8–9), 417–419 (1989). [doi:10.1016/0375-9601(89)90860-8].

[214] I. Kaminer, M. Segev, D. N. Christodoulides, **Self-Accelerating Self-Trapped Optical Beams**, *Phys. Rev. Lett.* **106**(21), 213903 (2011). [doi:10.1103/PhysRevLett.106.213903].

[215] K. D. Moll, A. L. Gaeta, G. Fibich, **Self-Similar Optical Wave Collapse: Observation of the Townes Profile**, *Phys. Rev. Lett.* **90**(20), 203902 (2003). [doi:10.1103/PhysRevLett.90.203902].

[216] P. Polynkin, M. Kolesik, J. Moloney, **Filamentation of Femtosecond Laser Airy Beams in Water**, *Phys. Rev. Lett.* **103**(12), 123902 (2009). [doi:10.1103/PhysRevLett.103.123902].

[217] N. N. Akhmediev, A. Ankiewicz, **Solitons, Nonlinear Pulses and Beams** (Chapman and Hall, London, England, 1997).

[218] D. G. Papazoglou, S. Suntsov, D. Abdollahpour, S. Tzortzakis, **Tunable intense Airy beams and tailored femtosecond laser filaments**, *Phys. Rev. A* **81**(6), 061807 (2010). [doi:10.1103/PhysRevA.81.061807].

[219] F. Courvoisier, P.-A. Lacourt, M. Jacquot, M. K. Bhuyan, L. Furfaro, J. M. Dudley, **Surface nanoprocessing with nondiffracting femtosecond Bessel beams**, *Opt. Lett.* **34**(20), 3163–3165 (2009). [doi:10.1364/OL.34.003163].

[220] M. K. Bhuyan, F. Courvoisier, P.-A. Lacourt, M. Jacquot, L. Furfaro, M. J. Withford, J. M. Dudley, **High aspect ratio taper-free microchannel fabrication using femtosecond Bessel beams**, *Opt. Express* **18**(2), 566–574 (2010). [doi:10.1364/OE.18.000566].

[221] E. Greenfield, M. Segev, W. Walasik, O. Raz, **Accelerating Light Beams along Arbitrary Convex Trajectories**, *Phys. Rev. Lett.* **106**(21), 213902 (2011). [doi:10.1103/PhysRevLett.106.213902].

[222] L. Froehly, F. Courvoisier, A. Mathis, M. Jacquot, L. Furfaro, R. Giust, P. A. Lacourt, J. M. Dudley, **Arbitrary accelerating micron-scale caustic beams in two and three dimensions**, *Opt. Express* **19**(17), 16455–16465 (2011). [doi:10.1364/OE.19.016455].